Quantifying Antarctic Icebergs and their Melting in the Ocean

Tiago Araújo Marques da Silva

Department of Geography
University of Sheffield

November 2006

Thesis submitted for the degree of Doctor of Philosophy

To my parents,
Margarida and Daniel
for all their love

Acknowledgements

I wish to thank my main supervisor, Grant Bigg, for the enthusiasm with which he guided this work and his unfaltering support, while at the same time giving me the freedom to carry out my own ideas. To Keith Nicholls, my supervisor at the British Antarctic Survey, for the encouragement given and for the very productive interactions to which he lent his scientific rigour and an extensive knowledge of the Southern Ocean.

I had the opportunity to interact with other researchers in the area to which I am indebted. Rupert Gladstone provided access to the code and output of his iceberg simulations. Douglas MacAyeal and Young-Jin Kim shared GPS data from iceberg stations on the Ross Sea. Helen Fricker and, again, Young-Jin Kim helped me decode the several releases of ICESat data. Jo Jacka shared and discussed the ANARE ship-based observations of icebergs. R.H. Harvey provided the code for the Sieves image processing algorithm. The crew of the R.S.S. Shackleton helped carry out the field project. To Adrian Jenkins for several discussions on the effect of meltwater around ice. Stan Jacobs, Hartmut Hellmer and four anonymous referees helped improve chapters 3 and 6. The National Ice Center and David Long provided access to their database of iceberg tracks.

To Aldina, my partner and friend, for the encouragement that got me through the gloomy moments and for knowing me so well. To Alexandre for stretching his friendship this 2000 km.

It were the people that I have met both at the University of East Anglia, during the first year, then at the University of Sheffield, and in the field work in the Southern Ocean, that made this an enjoyable period of discovery and that broadened my middle-Portuguese horizons. To Tricia, Lindsay, Beatriz, Em, César, Jo, John Green, Jos, Monica, Alan, Jon, Alex, Liz, Zöe, Ben and Richard, among others.

This work was funded by the Portuguese Science and Technology Foundation, PhD studentship SFRH/BD/8246/2002 and British Antarctic Survey through a CASE

fundinf. The field project in the Weddell Sea was supported by the Antarctic Funding Initiative, Collaborative Gearing Scheme 6/14. Satellite images were obtained from the European Space Agency through a Category 1 project.

Abstract

From the Antarctic Ice Sheet calves every year into the Southern Ocean, an average of 2000 km^3 of icebergs. The meltwater is spread over a large area in the Southern Ocean but the large temporal variability in iceberg calving and the clustering of iceberg distribution means that meltwater injection can be locally very high.

This study quantifies iceberg distribution, movement and melting using remote sensing observations and modelling. Icebergs were detected and tracked on Synthetic Aperture Radar images using a new computer-based iceberg detection method. The method allows an efficient and systematic processing of large volumes of SAR images, necessary to build a climatology of icebergs in the Southern Ocean. Tests were conducted using ground data from a field campaign and against manual image classification. The method was applied to several SAR image collections, namely the RADARSAT RAMP mosaic for the totality of coastal Antarctica, providing the first picture of iceberg distribution over such a large area.

Giant icebergs (icebergs above 100 km^2 in area) were shown to carry over half the total mass of the Antarctic iceberg population. Estimates of the spatial distribution of giant iceberg melting over the ocean were made using observed tracks and modelling the melting and spreading along its path. The modelling of basal melting was tested using ICESat laser altimetry to measure the reduction in the freeboard of three giant icebergs in the Ross.

The distribution of meltwater for giant icebergs was combined with an existing simulation of meltwater distribution from smaller icebergs to produce the first map of total iceberg meltwater for the Southern Ocean. The iceberg contribution to the freshwater flux is shown to be relevant to both the Weddell Sea and the Southern Ocean south of the Polar Front.

Contents

Chapter 1 Introduction

The Antarctic continent is almost completely covered by an ice cap with an average thickness of 2 kilometres [*Lythe et al.*, 2000] formed by snow fallen over hundreds of thousands off years. In one year the snow accumulation is estimated to be 2246±86 Gt yr^{-1} [*IPCC*, 2001] or on average 1 m thick of snow over the continent. This snow compacts into firn and then into ice that, driven by gravity, inches its way to the coast. On reaching the coast, and supported by its buoyancy, the ice sheets extend over the water forming ice shelves and floating glacier tongues. One fourth of the ice volume that crosses over the ice sheets' grounding line melts in contact with the ocean [*IPCC*, 2001]; in some places the meltrate can be as high as 12 m yr^{-1} [*Jacobs et al.*, 1996]. Rifts created by the glaciological stress fields or the flexing of the extensions of floating ice, through tides, storms or collision with passing icebergs, causes the calving of new icebergs. The icebergs spread over most of the Southern Ocean as they melt onto the surface layers.

The general drift pattern of icebergs in the Southern Ocean has been known since the 1960s through the compilation of ship-based observations [*Bakayev*, 1966]. The pattern, shown in Figure 1, is better understood in terms of the general circulation of the Southern Ocean. The Antarctic Coastal Current travels westward all around the coast of Antarctica, only interrupted by the Antarctic Peninsula. The most important drivers are the south-easterly winds that originate in the cold high Antarctic plateau. This narrow current, around 30 km wide, carries the majority of calved icebergs along the coast [*Gladstone and Bigg*, 2002] and the very cold and fresh seawater cause a relatively slow melting.

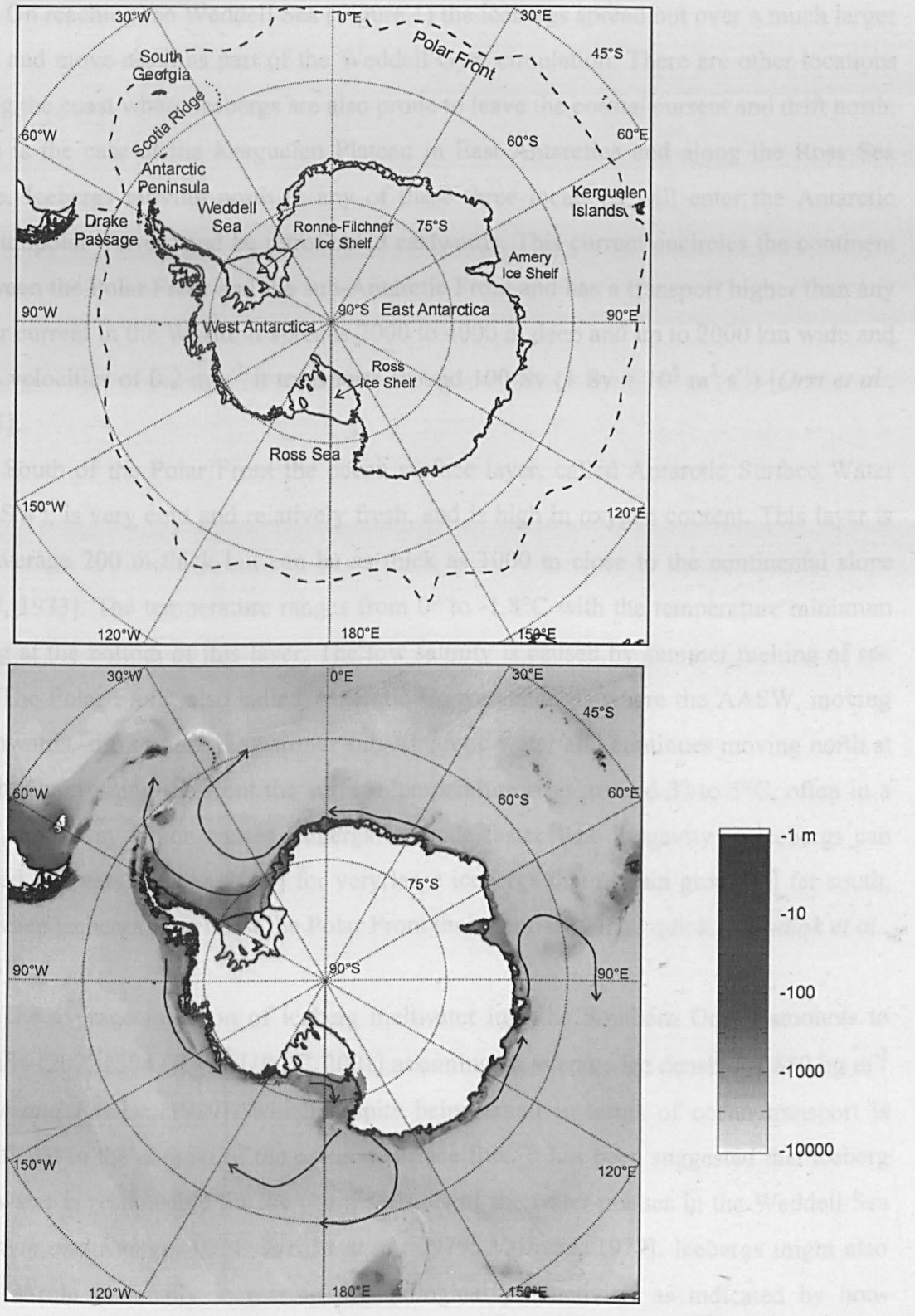

Figure 1 – (Top) Map of Antarctica and Southern Ocean with features mentioned in the text and (bottom) bathymetry of the area shown by shading and general pattern of iceberg drift after [*Tchernia and Jeannin*, 1984] indicated by arrows.

On reaching the Weddell Sea (Figure 1) the icebergs spread out over a much larger area and move north as part of the Weddell Gyre circulation. There are other locations along the coast where icebergs are also prone to leave the coastal current and drift north. This is the case at the Kerguelen Plateau in East Antarctica and along the Ross Sea Gyre. Icebergs moving north in any of these three locations will enter the Antarctic Circumpolar Current and be retroflected eastwards. This current encircles the continent between the Polar Front and the sub-Antarctic Front and has a transport higher than any other current in the World. It spreads 2000 to 4000 m deep and up to 2000 km wide and with velocities of 0.2 m s^{-1} it transports around 100 Sv (1 Sv = 10^6 m^3 s^{-1}) [*Orsi et al.*, 1995].

South of the Polar Front the ocean surface layer, called Antarctic Surface Water (AASW), is very cold and relatively fresh, and is high in oxygen content. This layer is on average 200 m thick but can be as thick as 1000 m close to the continental slope [*Gill*, 1973]. The temperature ranges from 0° to -1.8°C with the temperature minimum being at the bottom of this layer. The low salinity is caused by summer melting of sea ice. The Polar Front, also called Antarctic Convergence, is where the AASW, moving northwards, sinks under the warmer sub-Antarctic water and continues moving north at depth. On crossing the front the surface temperature rises around 3° to 5°C, often in a very sharp way which causes icebergs to erode faster. The longevity of icebergs can exceed 10 years [*Young*, 2002] for very large icebergs that remain grounded far south, but when icebergs travel past the Polar Front their demise will be quick [*Schodlok et al.*, 2006].

The average injection of iceberg meltwater into the Southern Ocean amounts to 77 mSv (2072±304 Gt yr^{-1} [*IPCC*, 2001] assuming an average ice density of 850 kg m^{-3} [*Keys and Fowler*, 1989]) which despite being small in terms of ocean transport is significant in the context of the ocean's surface flux. It has been suggested that iceberg meltwater is responsible for the characteristics of the water masses in the Weddell Sea [*Foldvik and Kvinge*, 1974; *Jacobs et al.*, 1979; *Neshyba*, 1977]. Icebergs might also have a role in locally increasing the biological productivity, as indicated by non-systematic observations of wildlife foraging around icebergs [*Ainley and Jacobs*, 1981; *Jacobs et al.*, 1979].

The meltwater release by ice shelves seems to be responsible for cooling and freshening of the surface layer, thickening of the sea ice and stabilization of the nearby water column [*Hellmer*, 2004]. The volume of iceberg meltwater is three times larger,

although the form and location of the release differs from ice shelves. The testing of the previously mentioned hypothesis and the inclusion of iceberg meltwater in ocean circulation models is held back by the lack of a climatology of iceberg distribution, drift and melting.

Gladstone and collaborators [*Gladstone*, 2001; *Gladstone et al.*, 2001] adapted an Arctic iceberg trajectory and erosion model [*Bigg et al.*, 1997] for the Southern Ocean, and forcing it with a climatology for the ocean, atmosphere and sea ice, simulated the climatological pattern of iceberg movements and melting. The model only represented icebergs up to 2 km in length as larger icebergs are more difficult to model successfully, probably due to the changes caused by the iceberg itself to the ocean currents which is the main forcing. These results reproduced well the observed northern most limits of iceberg distribution. Nevertheless there is still no observational climatology of iceberg and meltwater distribution as it requires the detection of large numbers of icebergs spread over the whole Southern Ocean.

Antarctic giant icebergs (icebergs larger than ~18 km in length) are tracked by the National Ice Center in the United States and this accounts for about half the volume of icebergs calved into the ocean [*Jacobs et al.*, 1992]. The detection of smaller icebergs is more labour intensive and requires higher resolution satellite images. This thesis is concerned with measuring the distribution of icebergs in the Southern Ocean and in estimating the release of meltwater into the Southern Ocean. For this purpose Synthetic Aperture Radar (SAR) satellite images were used in conjunction with iceberg tracks. Modelling of iceberg basal melting was used to estimate meltwater spatial and temporal variability. The structure of the thesis is now summarised up.

Chapter 2 starts by giving an introduction to the SAR sensor and properties of SAR images, and then presents a comparison of several image processing methods applied to the detection of icebergs on SAR images.

A computer-based algorithm to detect and track icebergs in high resolution SAR images is presented in Chapter 3. It allows a semi-automated observation of icebergs in a systematic and time-efficient way. The contents of this chapter were published as a journal paper during the course of this thesis [*Silva and Bigg*, 2005].

Medium resolution (150 m) and wide coverage SAR images are particularly well suited for icebergs detection over large areas of the ocean. In Chapter 4 the iceberg detection and tracking algorithm is applied to these images and validated using both high resolution images and field observations. The method is applied to two SAR image

mosaics and the distribution of icebergs around the Antarctic coast is mapped. This is analysed and compared with previous ship-based observations.

In Chapter 5 an estimate is made of the average meltwater distribution in the Southern Ocean. Giant iceberg tracks, modelling of basal melting and previous results of dynamical and thermodynamical simulations of icebergs up to 2 km in size [*Gladstone*, 2001; *Gladstone et al.*, 2001] were combined to produce this estimate. The magnitude of the iceberg meltwater is compared with the other terms of the freshwater flux for both the Weddell Sea and the Southern Ocean and shown to be significant. The contents of this chapter were also published as a journal paper [*Silva et al.*, 2006].

Estimates of meltwater injection, as performed in the previous chapter, rely on accurate simulations of iceberg basal melting. In Chapter 6 laser altimetry from the ICESat satellite is applied to measure changes to the freeboard of three giant icebergs in the Ross Sea. These measurements of basal melting and other published data [*Scambos et al.*, 2005] are compared with modelling results.

The discussion of the various parts of this thesis are generally contained within individual chapters, however, Chapter 7 contains a general discussion of issues that cross several chapters. The quantification of iceberg meltwater is a starting point to evaluate the impact of icebergs in the ocean but how the meltwater mixes with the ambient water is also poorly known. From this process depends the properties of the mixture, the magnitude of the area around icebergs that is affected by melting and the effect on the surface heat flux. Chapter 7 also includes a review of the present knowledge of how meltwater mixes with ambient water and highlights the gaps in the literature relevant to the study of the effect of the icebergs to the ocean. In 7.2 we present the main conclusions from this thesis work.

Chapter 2 On Synthetic Aperture Radar Images and Scene Analysis

2.1 SAR imagery

The Synthetic Aperture Radar (SAR) can produce high resolution images of the earth's surface independently of Sun illumination and cloud conditions. Radar stands for **ra**dio **d**etection **a**nd **r**anging and describes sensors operating in the radio part of the electromagnetic spectrum that emit radiation and use its echo properties to detect and locate targets. Because SAR is an active sensor it does not rely on the Sun's energy, and thus, unlike optical imagery, can be used during the polar winters.

The delay between emission and echo reception informs us of the distance to the target. As the speed of light, c, is a known constant, the distance is $d = t\,c\,/\,2$, where t is time delay and the factor two takes into account the double way trip of the radiation. The intensity of the returned radiation depends on the target's geometry and electromagnetic characteristics. This pixel intensity is normally described by the backscattering coefficient, σ^0, which is the proportion of radiation power scattered back to the sensor per target unit surface, normalised for parameters of the radar system, such as transmitted power, antenna gain and distance to target. For better visualisation, SAR images will be plotted in the logarithm scale $\left[\sigma^0\right]_{dB} = 10.\log_{10}\left(\sigma^0\right)$ using the non-dimensional unit decibel (dB).

2.1.1 Microwave spectrum

Microwaves are at the high frequency end of the radio spectrum, with wavelength in the 1mm to 1 m range. For comparison, visible light has much shorter wavelength, extending from 0.4 to 0.7 μm. The interaction of radiation with the targets depends on the wavelength, for instance longer wavelengths tend to penetrate deeper into objects; while visible radiation only penetrates a few angstroms, microwaves can penetrate dozens of metres into very dry objects, such as sandy soil. Also, most of the microwave

spectrum suffers very little absorption from the atmosphere giving microwave sensors all-weather capabilities. Radiation scatters when it interacts with objects with size close to its wavelength, thus microwave sensors yield information on the geometric and structural characteristics of targets such as vegetation or ground roughness.

Figure 2 shows an optical and a SAR image of icebergs and sea ice. Both the iceberg and sea ice have a similar brightness on the Landsat (optical) image. On the SAR image more energy is returned from the iceberg than the sea ice because some of the radiation penetrates deeply into the ice where it is scattered and reflected [*Haykin et al.*, 1994]. The SAR image shows a better contrast between sea ice and icebergs, which is an advantage to detect icebergs.

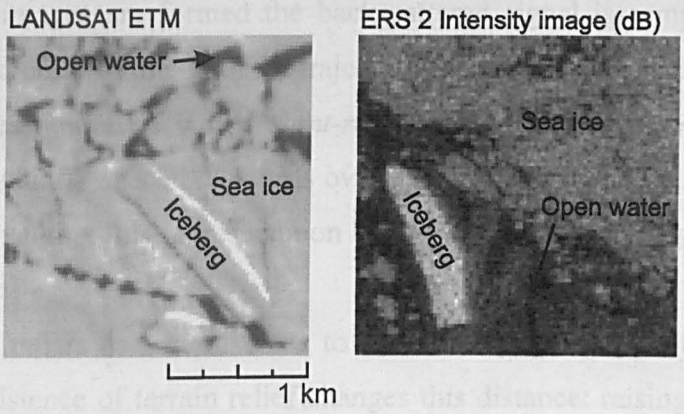

Figure 2 – Two similarly sized icebergs as seen by an optical sensor (Landsat) and SAR (ERS2) sensor. The scale is the same on both images.

2.1.2 SAR geometry

The sensors are typically mounted on an aeroplane or satellite, and the sensor is pointed sideways, being therefore named side-looking radar. The geometry of such a sensor is depicted in Figure 3. The directions perpendicular and parallel to the platform movement are designated range and azimuth, respectively.

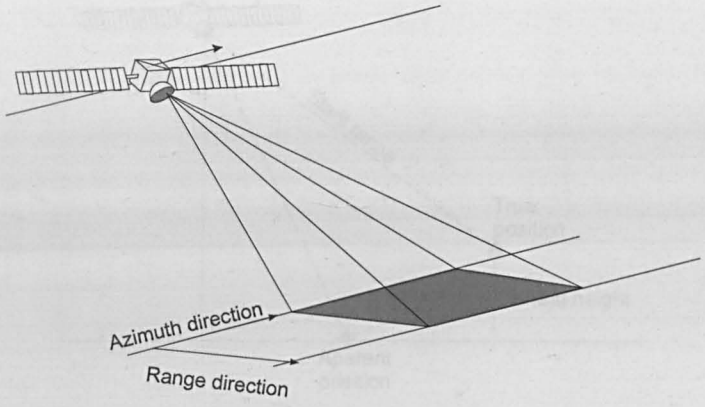

Figure 3 - Geometry of a side looking radar system.

When SAR images are formed the backscattered signal is sampled in the range direction (perpendicular to the platform trajectory) at regular distances from the sensor. This image representation is called *slant-range*. The image might then have to be resampled into regularly spaced distances over the earth's surface, called *ground-range* (see Figure 4). Changing this representation leaves the image unchanged in the azimuth direction.

Side-looking radars use the distance to sensor to determine the target position in range. But the existence of terrain relief changes this distance: raising the target above the ground bring it closer to the sensor, making it look like it was still on the ground, but closer to the satellite track (see Figure 5).

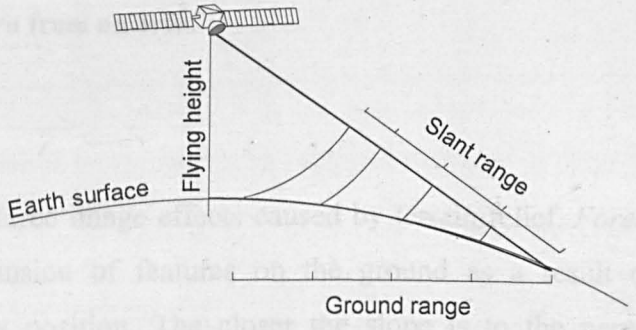

Figure 4 - Slant-range versus ground-range image representation. Equidistant points on the ground (ground-range) result in differently distanced points on slant-range (see text).

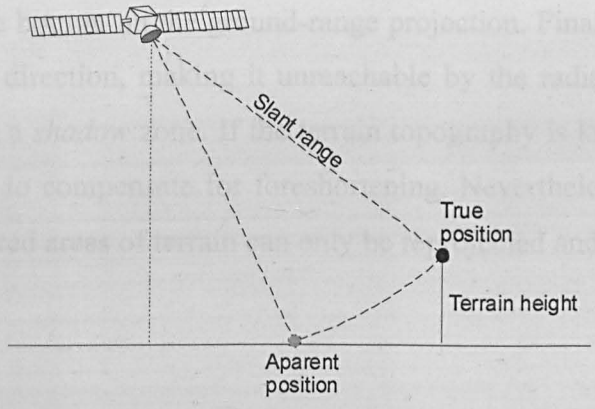

Figure 5 - Effect of terrain height on mapping.

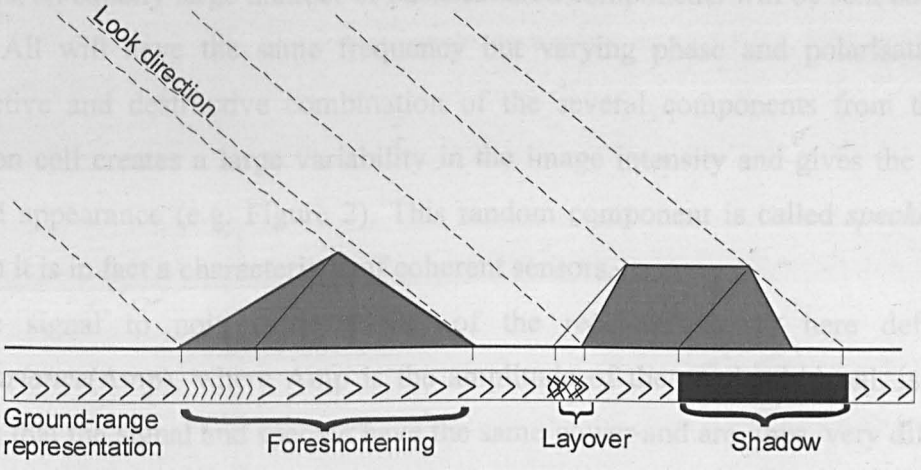

Figure 6 – Three effects of terrain relief on SLR images: *foreshortening*, *layover* and *shadow*. Foreshortening results in features looking compressed or expanded in ground-range; layover results in features being inverted and overlapped and shadow in the absence of radar return from an area.

Figure 6 shows three image effects caused by terrain relief. *Foreshortening* is the compression or expansion of features on the ground as a result of terrain height changing its apparent position. The closer the slope is to the perpendicular of the sensor's look direction, the more noticeable the effect. Conversely, a slope close to the look direction results in expanded terrain features. When the slope is so steep that the radiation reaches the top of the incline before reaching the bottom, the result is *layover*,

as the top lays over the bottom on the ground-range projection. Finally, when the slope departs from the look direction, making it unreachable by the radiation, no energy is backscattered, creating a *shadow* zone. If the terrain topography is known it is possible to resample the image to compensate for foreshortening. Nevertheless, information on the laid-over or shadowed areas of terrain can only be reprojected and not recovered.

2.1.3 Speckle

SAR sensors emit *coherent* radiation, that is, with a single frequency and polarisation. When the incident wave interacts with the target composed of many scatterers, an equally large number of backscattered components will be sent back to the sensor. All will have the same frequency but varying phase and polarisation. The constructive and destructive combination of the several components from the same resolution cell creates a large variability in the image intensity and gives the image a speckled appearance (e.g. Figure 2). This random component is called *speckle noise*, although it is in fact a characteristic of coherent sensors.

The signal to noise ratio (SNR) of the received signal, here defined as $\text{Amp}^2/\textit{variance}(\text{Amp})$, where Amp is the amplitude of the received signal, is only 1, meaning that the signal and speckle have the same power and are, thus, very difficult to separate. If more samples of the same location are available it is possible to get a better estimate of the σ^0. The maximum likelihood estimator is the average of the several realisations of σ^0

$$\hat{\sigma}^0 = \frac{1}{N}\sum_{n=1}^{N}\sigma^0(n). \tag{2.1}$$

This technique is called *multilook* and N is the number of looks. As repetitive samples of the same location for different times are seldom available, an alternative is to assume that neighbouring pixels have approximately the same properties. By averaging spatially, spatial resolution is traded off against reduced signal variability, or in a sense increased SNR. This increases linearly with the square root of the number of looks. In Figure 7 an image was averaged spatially, and it can be seen that as the number of looks increases the effect of speckle decreases.

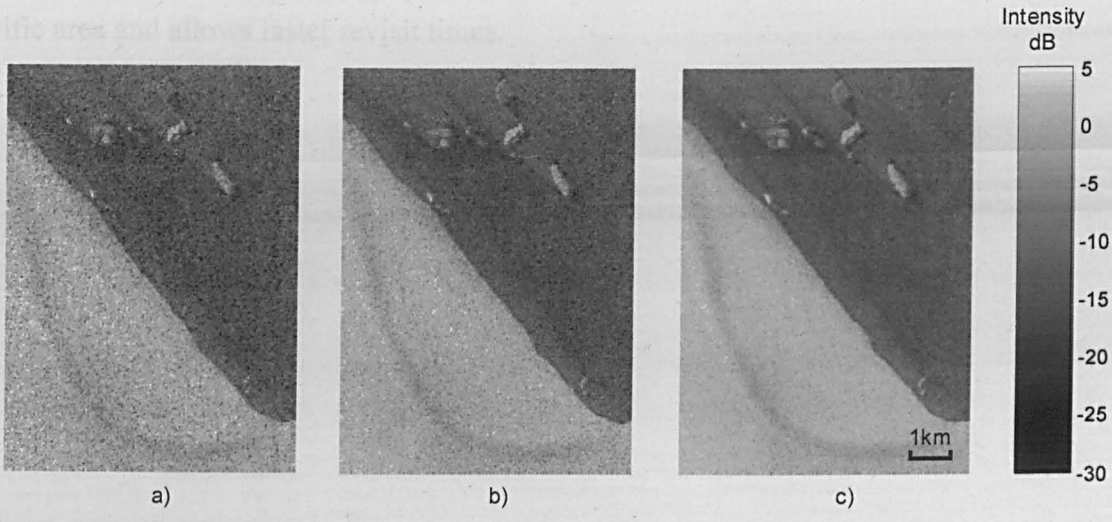

Figure 7 - The effect of spatial multilook for different values of the number of looks: a) N=3, b) N=5 and c) N=14. The image was extracted from an ERS-2 PRI image of the Antarctic coast and shows icebergs close to an ice shelf edge.

2.1.4 Available sensors

SAR sensors are used both on airborne and spaceborne platforms (satellites and space shuttle). Airborne sensors can provide detailed and customised coverage of a small area at a cost. Spaceborne sensors, on the other hand, can continuously acquire data with near-global coverage providing a valuable dataset for Earth monitoring, specifically for oceanography and glaciology.

Table 1 presents a summary of past, present and future SAR spaceborne sensors used for earth observation.

Several points are worth noticing. The European Space Agency has continuously acquired high resolution (26 m) images since 1991, using the satellites ERS-1, ERS-2 and ENVISAT. The Canadian agency also aims at maintaining continuity with Radarsat-1, launched in 1995, by launching Radarsat-2. Most modern systems have the flexibility of working at different resolutions and therefore swath width according to

what is needed. Also, custom acquisitions can be requested when the sensor is aimed a specific area and allows faster revisit times.

Table 1 – Main spaceborne Sinthetic Aperture Radar missions used for general Earth observation.

Sensor	Country or institution	Start	Duration	Band (freq., GHz)	Wavelength (cm)	Resolution (m)	Swath width (km)	Revisit time (days)
Seasat	USA	1978-06-27	100 days	L (1.28)	23.5	25	100	3/17
SIR-A	USA	1981-10-12	2.4 days	L (1.28)	23.5	40	50	
SIR-B	USA	1984-09-13	8.3 days	L (1.28)	23.5	16 – 58	20-40	
Almaz-1	Russia	1991-03-31	2 years	S (3.00)	10	15-30	20-45	
ERS-1	ESA	1991-07-16	9 years	C (5.25)	5.7	26	100	3/35/176
JERS-1	Japan	1992-02-01	4 years	L (1.28)	23.5	18	75	44
SIR-C/	USA and	09/05/1994	8 days	L	23.5	30	15-90	
X-SAR	Germany	and	each	C	5.8	30	15-90	
(shuttle)		30/09/1994		X (9.6)	3.1	30	15-40	
Radarsat-1	Canada	1995/11	>11 years	C (5.3)	5.7	8-100	50-440	24
ERS-2	ESA	1995	>11 years	C (5.25)	5.7	26	100	3/35/176
SRTM (shuttle)	USA	2000-02-11	11.2 days	C and X		30	50	n.a.
ENVISAT ASAR	ESA	2002-03-01	>6 years	C (5.3)	5.7	28/150/1000	100-400	1-30
Planned missions								
Radarsat-2	Canada	2007	7 years	C (5.3)	5.7	3-100	50-440	24
ALOS PALSAR	Japan	2006-01-24		L	23.6	7-100	40-350	
TerraSAR-X	Germany	2006	5 years	L		1-16	5-100	13

Both ERS/ENVISAT images and Radarsat are useful for monitoring roles due to the existence of a large library of acquired images. The characteristics of both standard and wide swath intensity images are summarised in Table 2. All the image types in Table 2 have a pixel spacing two times smaller than their resolution. This implies that the image has a strong spatial autocorrelation [see *Oliver and Quegan*, 1998]. In order to reduce the data volume to a 1/4, the intensity image can be block averaged with a 2×2 window and subsampled 1:2, doubling its pixel size but without loosing much spatial information. This procedure is equivalent to multilooking so increases the Equivalent Number of Looks (ENL), increasing the SNR. We calculated the increase in ENL for an ERS PRI image before and after pre-processing described above. The ENL was estimated by applying to homogenous areas of 100×100 pixels the following approximation [*Oliver and Quegan*, 1998]:

$$ENL = \frac{mean(\sigma^0)^2}{\mathrm{var}(\sigma^0)} \tag{2.2}$$

The pre-processing increased the ENL's value from 2.7 to 5.

Table 2 - Characteristics of the standard and wide swath intensity images from ERS/ENVISAT and Radarsat. ENL is the equivalent number of looks.

Image Type	Resolution (m)	Pixel spacing (m)	Coverage (km)	Image size (pixels)	ENL
ERS PRI/ ENVISAT IMP	30	12.5	100×100	8000×8000	>3
ENVISAT Wide Swath	150	75	400×400	5300×5300	11.5
Radarsat Standard	25×28	12.5	100×100	8000×8000	4
Radarsat SCANSAR (Wide)	100	50	500×440	10000×10000	4-8

2.2 Segmentation of SAR images

In Chapter 3 a computer-based technique to segment and track icebergs on SAR images is presented. Before a method could be selected and further improved, several segmentation algorithms had to be implemented and compared. Here this comparison is presented.

The speckle perturbation present in SAR images (see section 2.1.3) is equivalent to the presence of multiplicative noise. This means that the higher the backscattering coefficient of target area, the more variability will one see in the acquired image, so brighter areas will look noisier. Classical image processing methods are designed to cope with the more usual additive noise and yield erroneous results when applied to noisy SAR images. Therefore, the methods selected should be adequate to work with multiplicative noise, or, in signal processing terms, should have a constant false alarm rate (CFAR).

The methods compared here include edge-based methods that rely on an edge map and a region-based method that does not. An edge map is an image describing the likelihood of the presence of an edge. In the next section we will present several methods used to build edge maps. These must then be analysed and regions fully encircled by edges are identified objects or segments. In section 2.2.1.2 we present several segmentation methods based on edge maps and also a region-based method.

2.2.1 Brief description of the methods

2.2.1.1 Edge detection

2.2.1.1.1 Sobel gradient operator

The Sobel gradient operator [*Davis*, 1975; *Jain*, 1988] was designed to be used on images with additive noise, unlike radar images that have multiplicative noise. This widely used gradient operator was included here to demonstrate the effects of the incorrect use of this type of filter. This is a spatially invariant, linear filter with finite impulsive

response (FIR) which means that its output for each pixel is the linear combination of a limited number of neighbouring pixels. For example the spatial average filter that consists of averaging every pixel with its four horizontal and vertical neighbours can be written for a general pixel with coordinates m and n, $p_{m,n}$, as:

$$Avg_{m,n} = \frac{p_{m,n} + p_{m-1,n} + p_{m+1,n} + p_{m,n-1} + p_{m,n+1}}{5}. \tag{2.3}$$

This linear combination can also be represented by a matrix of the coefficients, also called the filter kernel, to be applied to each of the neighbours:

$$k = \begin{bmatrix} 0 & 1 & 0 \\ 1 & 1 & 1 \\ 0 & 1 & 0 \end{bmatrix} /5. \tag{2.4}$$

The centre element (in this case line 2 column 2) represents $p_{m,n}$ and the remaining elements its 8 pixel neighbours on the image. Because the four diagonal neighbours don't take part in calculation (2.3) their coefficients are 0, while the other neighbours have a coefficient of 1/5. Each pixel $q_{m,n}$ of the output image can be then calculated by

$$q_{m,n} = \sum_{l=1}^{3}\sum_{c=1}^{3} k_{l,c} \cdot p_{m-2+l,n-2+c} \,. \tag{2.5}$$

We can define the Sobel filter in the same way, except that it has two coefficient matrices, or kernels, to detect horizontal and vertical edges respectively:

$$k_{horiz} = \begin{bmatrix} -1 & -2 & -1 \\ 0 & 0 & 0 \\ 1 & 2 & 1 \end{bmatrix}, \; k_{vert} = \begin{bmatrix} -1 & 0 & 1 \\ -2 & 0 & 2 \\ -1 & 0 & 1 \end{bmatrix} \tag{2.6}$$

The outputs of each filtering operation, s_{horiz} and s_{vert}, are combined into an omni-directional edge map $s = \sqrt{s_{horiz}^2 + s_{vert}^2}$.

2.2.1.1.2 σ/μ filter

The σ/μ or *coefficient of variation* filter [*Sephton et al.*, 1994] is a multidirectional edge detector with CFAR for SAR images. It was first applied to SAR images by Sephton *et al.* [1994] and its calculation is the ratio of the standard deviation (σ) over the mean (μ) calculated in a kernel of a given size.

2.2.1.1.3 Ratio of averages filter

The Ratio Of Averages filter (ROA) is a directional CFAR filter [*Touzi et al.*, 1988]. It is calculated by splitting the filtering window into two areas which do not encompass the centre pixel (Figure 8). Then the averages of both subwindows are calculated and divided to test the presence of an edge in the space between. Taking the maximum value of both possible ratios, $\max\{A_1 / A_2, A_2 / A_1\}$, assures that the index has a value in [1,+∞). In this case, four subwindows of similar sizes and different orientations were used (Figure 8). Finally, the maximum value for the four orientations was taken [*Fjørtoft*, 1999b].

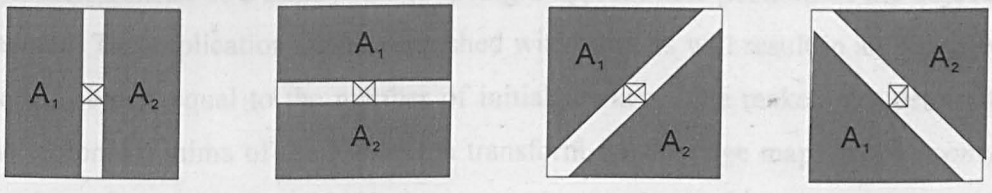

Figure 8 – The Ratio of average (ROA) filter is calculated for four different edge directions. For each direction it consists of the ratio of the average for each subregion, A1 and A2.

2.2.1.1.4 Multiresolution ROA

The larger the window size then the higher is the noise suppression. Unfortunately the size of the smallest object detected also increases. Furthermore, an assumption of the filter is that there is only one edge inside the window, which becomes less likely with larger

windows. The Multiresolution ROA [*Fjørtoft et al.*, 1997] applies the ROA filter using several window sizes, normalises it, and for each pixel takes the higher index, independently of the window size for which it was obtained. This results in more noise reduction in homogeneous areas of the image while remaining sensitive to small objects in high detail areas.

2.2.1.2 Segmentation methods

2.2.1.2.1 Watershed segmentation using *hconcave* markers

Watershed segmentation is a method derived from mathematical morphology [e.g. *Soille*, 2002] that thins the edges to unit width (skeletonises) and eliminates open contours, thus returning image segments. It was first introduced by Beucher and Lantuejoul [1978] but only later was a computationally efficient implementation proposed [*Vincent and Soille*, 1991]. The technique often leads to oversegmented images so Meyer and Beucher [1990] introduced the concept of *marker* to control the number of objects found. Markers consist of a binary image giving a approximate position of the objects to be segmented. The application of the watershed with markers will result in an image with a number of objects equal to the number of initial markers. The makers are determined using the regional minima of the H-minima transform for the edge map, called *hconcave* (once again refer to [*Soille*, 2002] for a good overview of modern mathematical morphology applied to image processing).

2.2.1.2.2 Watershed segmentation using basin dynamics

Oversegmentation is caused by every fluctuation on the edge map being translated into an object. A simple approach is to set to zero all values of the edge map below a certain threshold. The smarter method used here, called basin dynamics [*Grimaud*, 1992],

uses mathematical morphology operators to eliminate local minima deeper than a defined threshold.

2.2.1.2.3 Sieves

Sieves [*Bangham et al.*, 1996] is another image processing technique with its roots in mathematical morphology. One of the many uses for this technique is to perform image segmentation on a region-based formulation, so as to detect objects by aggregating segments with similar brightness values. Furthermore it is very straightforward to filter regions based on their size, eliminating objects too small (noise) or too large (background). The implementation used here is a library kindly provided by R.H. Harvey and A.J. Bangham from the University of East Anglia.

2.2.1.2.4 Watershed segmentation using *Sieves* as markers

Sieves proved to be quite good at detecting objects but less so at correctly extracting their contours. This variation on the watershed method uses sieves to provide the approximate position of the objects, and supplying this as markers to the watershed algorithm.

2.2.1.2.5 Williams *et al.* method

This technique, proposed to segment icebergs on SAR images [*Williams et al.*, 1999], is an adaptation of the sea ice segmentation technique proposed by Septhon and colleagues [1994]. The pre-processing step consists of block averaging the image with an 8×8 window followed by resampling at this same resolution. This procedure strongly reduces the amount of data to be dealt with (1/64 of the original), reduces the noise level and simplifies the distribution of pixel values to Gaussian, which simplifies analysis. On

the other hand spatial detail is lost. An σ/μ edge map is then used by an algorithm called "valley-seeking bonding" that localises the edges and reduces it to a skeleton [*Jain*, 1988]. Finally an iterative procedure cleans all the open edges, leaving only closed segments corresponding to regions.

2.2.2 Test methodology

One synthetic (Figure 9) and two real images (Figure 10) were used for the tests. The synthetic image was created to test the capacity to detect small objects at different contrast levels with the background. Noise was generated so as to simulate an ERS PRI/ENVISAT IMP intensity image, block-averaged and resampled on a 2×2 window. The number of looks simulated is 5. The real images were extracted from ERS-2 PRI images and block averaged and resampled on a 2×2 window. The resulting ENL is approximately 5 (see previous section).

The output of all the methods is a *label* image where the pixels belonging to each object will have a unique identifier. This image is converted to a binary image showing the presence or absence of objects. Finally, this classification is compared with the binary classification produced by the operator. The error measure should take into consideration both the pixels incorrectly classified as icebergs (false alarms) as well as missed pixels belonging to icebergs. The *exclusive or* logic operator, or XOR, returns 1 when the inputs are different and 0 otherwise. This was used to build the XOR error function,

$$e_{XOR} = \frac{\sum_M \sum_N (al \otimes op)}{\sum_M \sum_N op}, \qquad (2.7)$$

where $\Sigma_M \Sigma_N$ are the sums along all the M lines and N columns of the image, $\otimes$ denotes the exclusive or operator, and *al* and *op* are the classification performed by the algorithm and the operator, respectively. The e_{XOR} error can be interpreted as the number of incorrectly classified pixels as a proportion of the total number of iceberg pixels. Note that the output can be larger than 1.

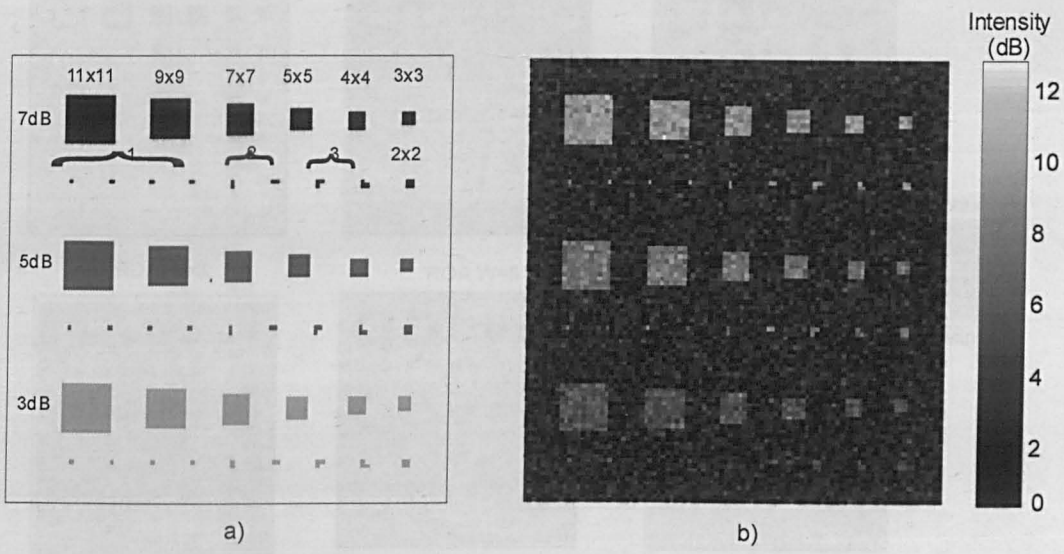

Figure 9- Synthetic test image: a) legend and b) the random realization used. The image simulates icebergs with different sizes and contrast levels with the background as seen on a ERS PRI image, block averaged and subsampled with window size 2×2. The noise was generated to reproduce an image with ENL=5. This was done by generating a gamma distribution with parameters μ = ENL and $\sigma = \sigma^0/ENL$.

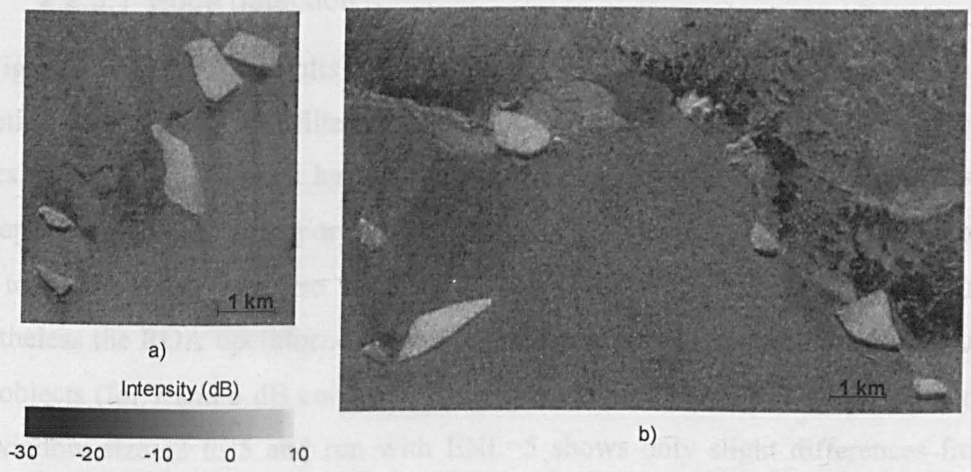

Figure 10 - Real SAR test images 1(a) and 2 (b) showing icebergs over a background of sea ice.

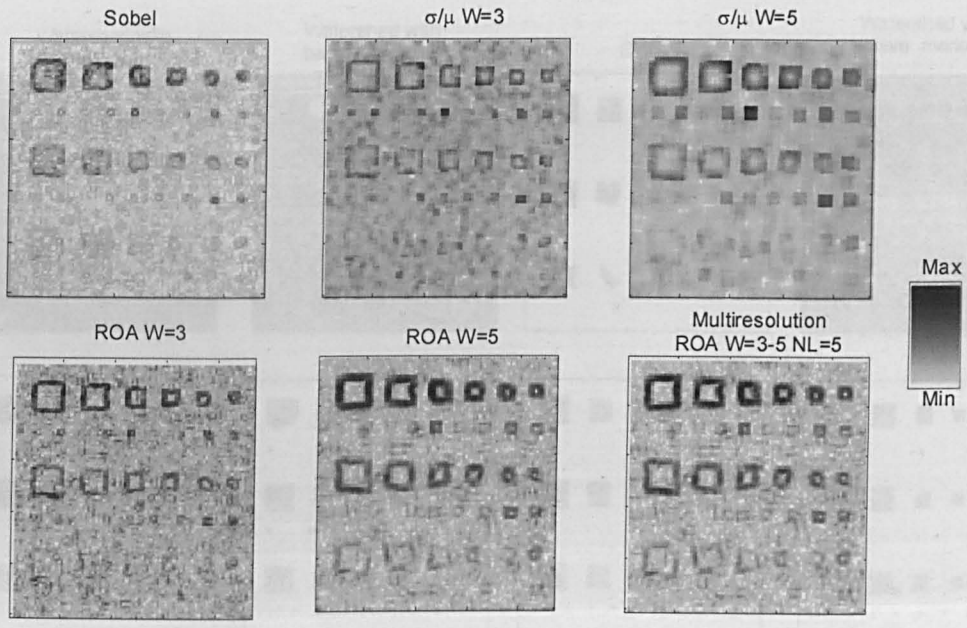

Figure 11 – Edge maps produced by several edge-detection methods when applied to the synthetic test image.

2.2.3 Test results

2.2.3.1 Edge detection

Figure 11 shows the results of the application of the edge detection methods to the synthetic image. The Sobel filter has higher edge values in the middle of the brighter squares. Because it is doesn't have a CFAR it is more likely to have false alarms in the brighter areas of the image. For both σ/μ and ROA filters the increase in window size leads to lower noise but also reduce the capacity in detecting the smaller objects. Nevertheless the ROA operator, even with W=5, discriminates better the edge around the small objects (for 7 and 5 dB contrast), while the σ/μ does not. The Multiresolution ROA with window sizes 3 to 5 and run with ENL=5 shows only slight differences from the ROA W=5 filter. As it is assumed that the former is better by design ([*Fjørtoft et al.*, 1997]) it was selected to be used as a base for the segmentation methods in these tests.

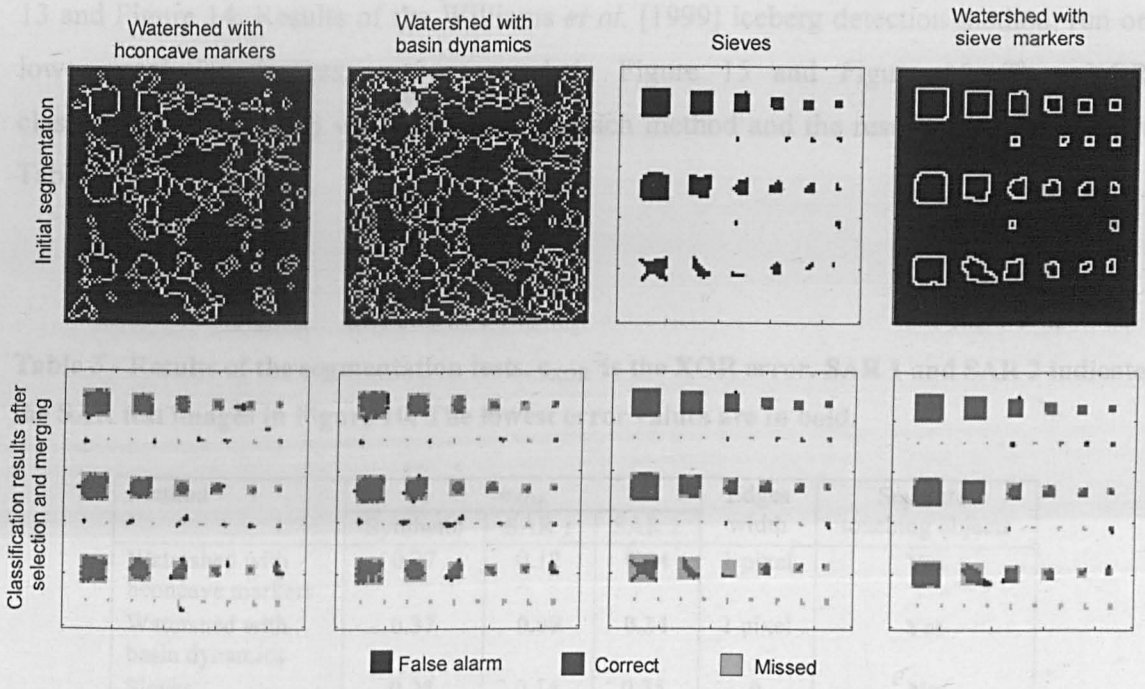

Figure 12 - Results of the segmentation of the synthetic test image. Objects resulting from the segmentation (images on top) are classified as icebergs and compared with the operator classification (images on bottom), as either correct, missed or false pixels.

The watershed transform separates regions according to the presence of edges, but not all the resulting objects will be icebergs. Dark objects such as open water or iceberg shadows, or medium brightness ones such as sea ice will also be segmented. A classification step is performed after the segmentation to identify objects as icebergs if their average σ^0>-6dB. The threshold is scene-dependent and is chosen by the operator.

2.2.3.2 Segmentation

The segmentation methods were first tested using the synthetic image in Figure 9b and the results are presented in Figure 12. The top row shows the segments produced and the bottom row the comparison with the ideal segmentation. The methods were also tested on the two sections or real SAR images in Figure 10. The results are presented in Figure

13 and Figure 14. Results of the Williams *et al.* [1999] iceberg detection method, run on lower resolution images, are presented in Figure 15 and Figure 16. The eXOR classification from (2.7) was calculated for each method and the results are presented in Table 3.

Table 3 - Results of the segmentation tests. e_{XOR} is the XOR error. SAR 1 and SAR 2 indicate the SAR test images in Figure 10. The lowest error values are in bold.

Method	e_{XOR}			Edges width	Separates touching objects
	Synthetic	SAR 1	SAR 2		
Watershed with hconcave markers	0.37	0.12	**0.34**	1 pixel	**Yes**
Watershed with basin dynamics	0.37	**0.09**	**0.34**	1 pixel	**Yes**
Sieves	0.28	0.14	0.35	**0**	No
Watershed with sieve markers	**0.18**	0.095	0.43	1 pixel	**Yes**
Williams et al. 1999	0.86	0.34	0.45	**0**	**Yes**

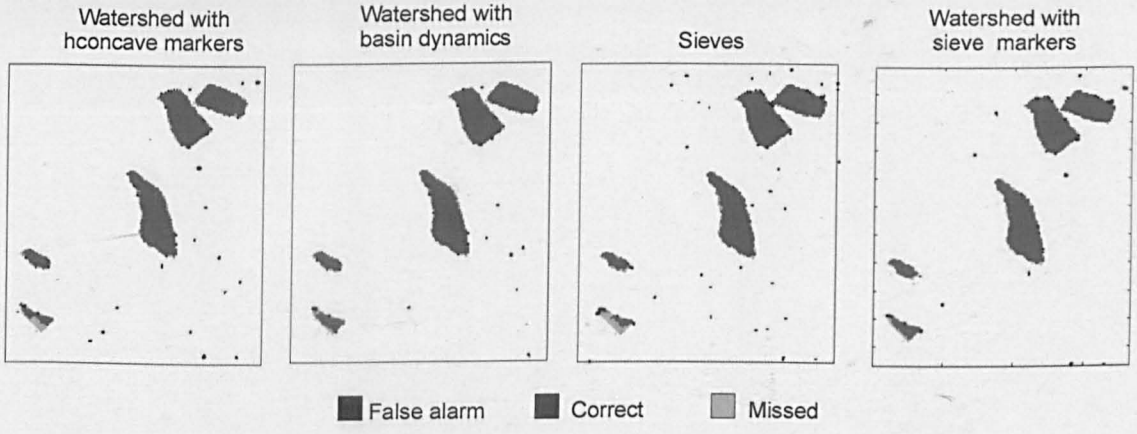

Figure 13 – Segmentation of real image 1 compared with operator classification.

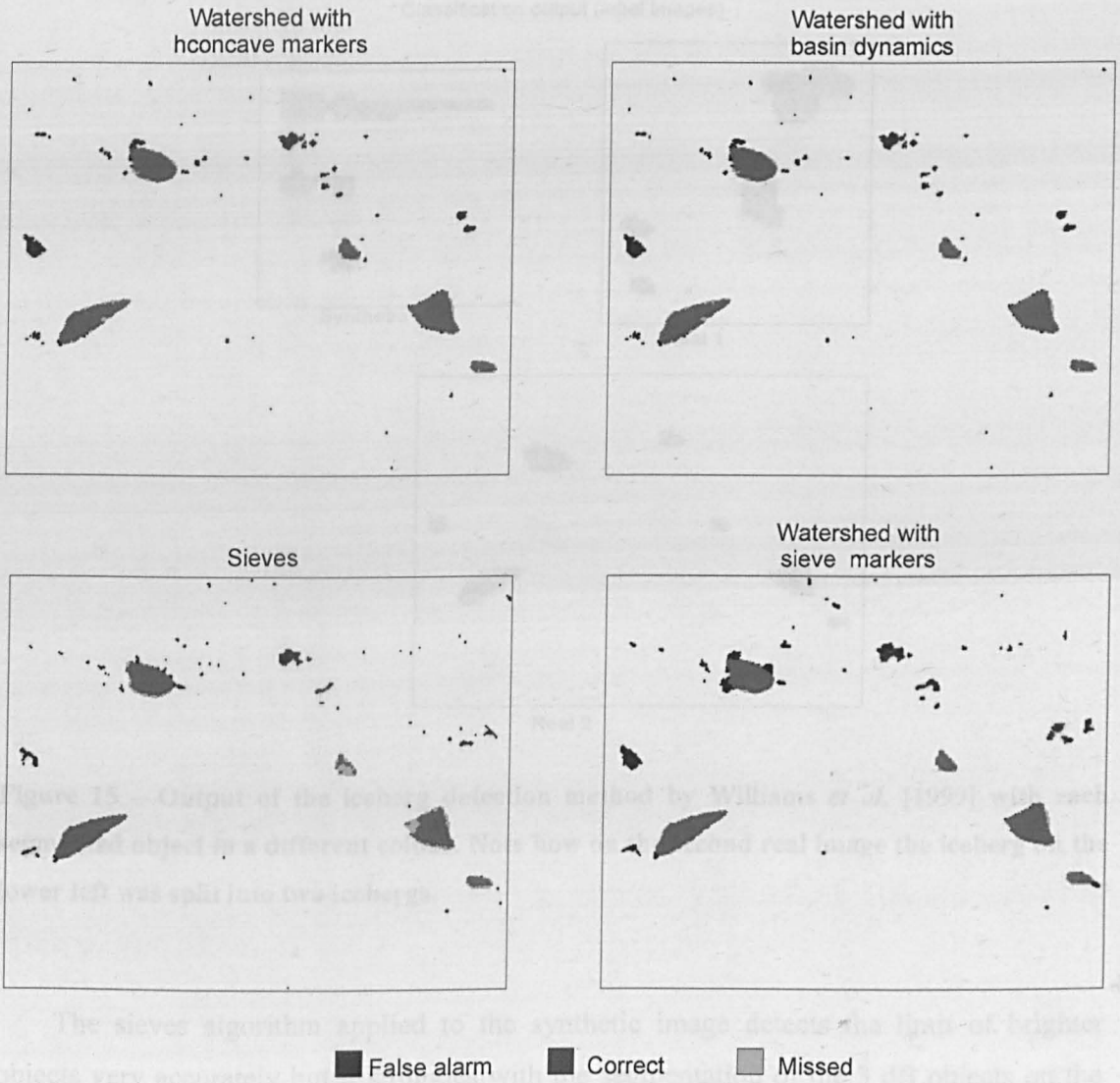

Figure 14 – Segmentation of real image 2 compared with operator classification.

When applied to the synthetic image, the watershed with hconcave markers and watershed with basin dynamics produce a very large number of segments over the background (top row in Figure 12). But after classification of the segments only one false alarm is generated. Small objects with only 3dB contrast are missed (*e.g.* bottom squares in Figure 12), but most other objects are correctly identified.

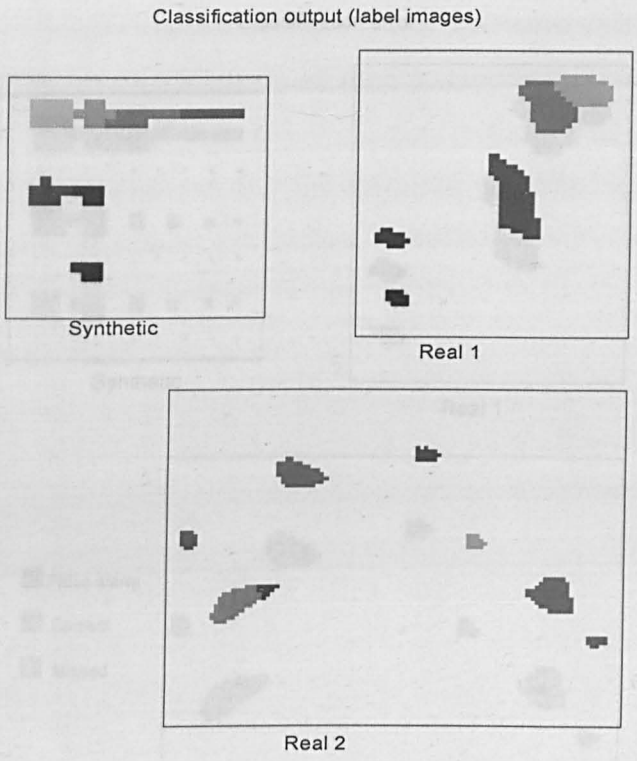

Figure 15 – Output of the iceberg detection method by Williams *et al.* [1999] with each segmented object in a different colour. Note how on the second real image the iceberg on the lower left was split into two icebergs.

The sieves algorithm applied to the synthetic image detects the limit of brighter objects very accurately but it struggles with the segmentation of the 3 dB objects on the lower row. Also, on the dimmer icebergs on the real images the advantage disappears, as can be seen with the partially missed iceberg on the left bottom corner in Figure 13 and the two also partially missed objects on the right hand of the image in Figure 14. Being a region-based method, the sieves algorithm groups pixels with similar brightness values. All pixel clusters brighter than a threshold are then selected. If the threshold is lowered then noisy areas of the background would also be erroneously selected. A shortcoming is the fact that touching objects are not separated, as can be seen with the two large icebergs on the top right handed corner of Figure 13. This limitation would seriously hamper the segmentation of individual icebergs in areas with high iceberg concentration, and thus bias ice volume estimates.

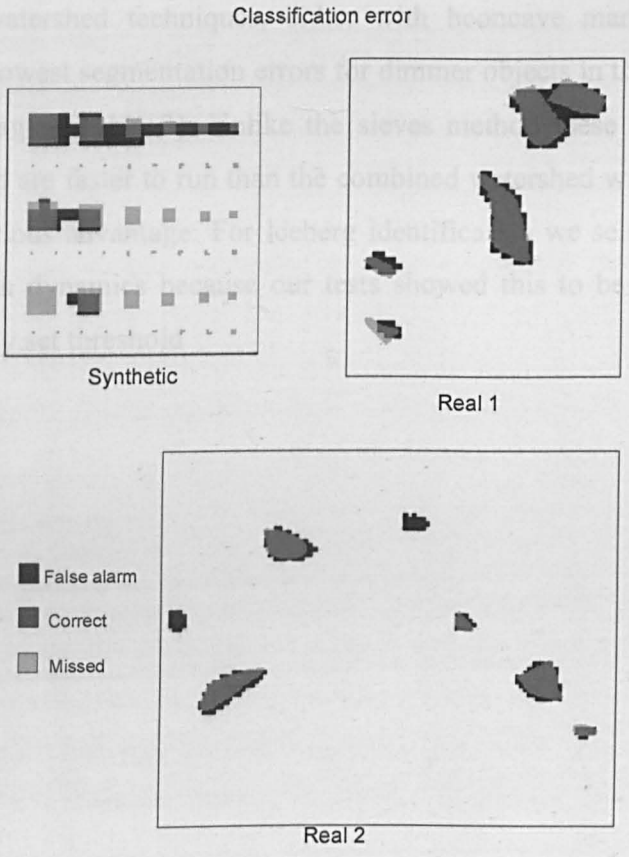

Figure 16 – Evaluation of the classification performed by the iceberg detection method by Williams *et al.* [1999].

The watershed with sieve markers method missed approximately as many small objects as the sieves method, while separating touching objects. But the markers are difficult to set; if these overlap the object edge then the object spills outside its bounds has happened to the large top left iceberg in Figure 14.

The Williams *et al.* method works at much lower resolution, leading to most of the objects of 7×7 pixels or smaller going undetected or being grouped with other objects (for example see the results for the synthetic image in Figure 16). The algorithm has managed to separate the two touching icebergs at the top of Figure 10a (see Figure 16 top right) although it split the bottom left-most object in Figure 10b into two objects (see bottom of Figure 16).

Overall, the watershed techniques, either with hconcave markers or with basin dynamics gave the lowest segmentation errors for dimmer objects in the synthetic exercise and on the real images (Table 3). Unlike the sieves method these allow separation of touching objects and are faster to run than the combined watershed with markers, that did not present any obvious advantage. For iceberg identification we selected the watershed technique with basin dynamics because our tests showed this to be more robust to the value of the manually set threshold

Chapter 3 Computer-based identification and tracking of Antarctic icebergs in SAR images

The contents of this chapter were published as a paper in *Remote Sensing of the Environment* [*Silva and Bigg*, 2005]. The co-author, G. Bigg, participated in this work through numerous productive discussions and by revising the manuscript.

3.1 Introduction

Giant icebergs (icebergs longer than 10 nautical miles or approximately 18.5 km) are systematically tracked by the National Ice Center and the Brigham Young University Center for Remote Sensing, using several satellite sensors. However the main source of information on smaller icebergs around Antarctica has been ship-borne observations [*Hamley and Budd*, 1986; *Orheim*, 1985a]. While potentially valuable, this information is believed to exhibit some biases by overestimating coastal numbers and underestimating the areas where icebergs are absent [*Gladstone and Bigg*, 2002]; it also does not usually provide iceberg tracks. More recently, Synthetic Aperture Radar (SAR) has been used to look also at smaller icebergs [*Gill*, 2001; *Gladstone and Bigg*, 2002; *Power et al.*, 2001; *Willis et al.*, 1996; *Young et al.*, 1998]. Since 1991 several SAR sensors have covered the Antarctic coast without interruption, building a large data source. Most icebergs, after calving, are carried along the coast in a counter-clockwise fashion by the narrow Antarctic Coastal Current [*Tchernia and Jeannin*, 1984]. Gladstone *et al.* [2001] proposed the acquisition and analysis of time series of images from areas close to the coast, where most icebergs would flow, to monitor a large fraction of the iceberg traffic. The ERS and Envisat satellites have provided images of Antarctica continuously since 1991. Nevertheless, this large dataset is of limited use unless a time efficient and systematic way exists to analyse the images.

In this study we propose the first computer-based method that allows both the identification and tracking of icebergs as small as 200 m in length in high resolution

satellite-acquired SAR images. In section 3.2 we overview the problem of segmenting SAR images. This is followed by a review, in Section 3.3, of the application of computer-based methods to the identification of icebergs in remotely sensed images. The full algorithm is described in Section 3.4 with the performance evaluation of the application to three satellite images (see Appendix for the image details) being presented in Section 3.5. This section also includes the results of the application of the method by Williams *et al.* [1999] applied to the same images. Discussion and conclusions occupy the last section.

3.2 Segmentation of SAR images

Intrinsic to SAR images is the signal variability known as speckle (see section 2.1.3). This characteristic of the signal makes the analysis of SAR images very difficult. However, the problem can be mitigated by making use of the knowledge of the statistical characteristics of the signal.

The application of traditional segmentation algorithms designed for additive noise to SAR images often yields erroneous results. With differential operators, for example, since the variability of the signal increases with the mean amplitude the probability of falsely detecting an edge on the image will also increase. Numerous segmentation methods have been proposed specifically for use in coherent images. These may be classified into local and global methods. Local methods can be applied to one section of the image at a time while global methods look for a solution taking into account the whole image. Global methods should ultimately attain better results but are slower and this field is still immature. As we are seeking a computationally efficient algorithm we will only consider local methods. Also, as we intend to use intensity images we will not consider methods designed for complex or multi-polarisation images. Applicable methods can be classified as edge-based or region-based, depending on whether the method tries to locate boundaries between pixels (edges) or to aggregate pixels with similar characteristics into regions. Edge-based approaches generally consist of two steps. First an index of spatial dissimilarity, such as the gradient, is calculated in order to construct an edge map. Pixels

with high values have higher probability of being an edge. The second stage then decides whether the pixels belong to an edge.

The segmentation method presented here relies on an edge-based approach. The multi-resolution filter of [*Fjørtoft et al.*, 1997] is used to calculate an edge map, which is then segmented by the watershed algorithm [*Beucher and Lantuejoul*, 1978; *Soille*, 2002; *Vincent and Soille*, 1991]. The basin dynamic method [*Grimaud*, 1992] was chosen to limit over-segmentation, where the threshold is chosen with the help of a contour dynamics map [*Najman and Schmitt*, 1996; *Schmitt*, 1998]. As in Fjørtoft [1999b], a merging step is applied at the end to correct over-segmentation and make the algorithm less sensitive to the choice of basin dynamics threshold. Here we use a simple heuristic merging rule. The segmentation method used here is well adapted to the statistical properties of coherent images, so should perform well in high resolution images with low SNR. This is important when using full resolution images, where it will be possible to track icebergs below 1 km in length through their shapes. Furthermore, this method is capable of separating touching objects.

3.3 Application to the identification of icebergs

Williams and MacDonald [1995] introduced an algorithm to identify and outline icebergs on Landsat TM images based on associating their sunlit faces with their shadow. When SAR images became widely available they became the imagery of choice for medium to small iceberg identification because of their lack of dependence on sunlight or cloud cover, and because of the strong signal backscattered from icebergs in sub-zero temperatures. A pixel based detection with Constant False Alarm Rate (CFAR) was applied to SAR images to identify ships (Vachon et al., 1997) and later icebergs in the Arctic [*Gill*, 2001; *Power et al.*, 2001]. This technique is well adapted to identify bright targets against a dimmer sea background, as long as these targets are smaller than the sliding window used. On the other hand, the larger Antarctic icebergs vary widely in size and are frequently embedded in a poorly contrasting sea ice background, especially in winter.

The simplest solution to deal with SAR speckle is to average intensity images spatially by block processing, followed by undersampling. SAR methods proposed so far work with images with pixel width increased from 12.5 m to 100 m. Willis *et al.* [1996] used simple thresholding of the resolution-reduced image, combined with mathematical morphology operators, to identify icebergs both through their bright reflectance and their shadows. One problem with their technique is that it merges touching objects and thus biases the estimation of iceberg mass. Williams *et al.* [1999] overcame this problem by adapting previous sea ice detecting algorithm [*Sephton et al.*, 1994]. An edge map was built using an omni-directional CFAR index. A valley-seeking method was then used to perform the segmentation step. Young *et al.* [1998] applied this technique to the study of Antarctic iceberg distribution and abundance in winter.

The problem addressed by the present algorithm is a different one. Not only do we seek to identify icebergs in one image, but also to extract their shape in order to allow tracking between different images. With a pixel distance of 100 m, icebergs must be at least a kilometre in size to allow shape extraction. Unfortunately, higher resolution images have stronger speckle noise. This makes segmenting the same image at higher resolution much harder, but it is necessary to perform iceberg tracking effectively.

3.4 Algorithm description

3.4.1 Iceberg identification

The iceberg identification algorithm is represented as a flowchart in Figure 17 and described in detail below. SAR images are pre-processed to reduce the data size. If the coast is visible in the image, a binary mask is produced to exclude coastal areas from the analysis. The segmentation step uses an edge detection method. The classification is performed by a simple rule classifier and false alarms are corrected by the operator. An example of algorithm classification accuracy when compared with manual classification is shown for a section of a SAR image in Figure 18

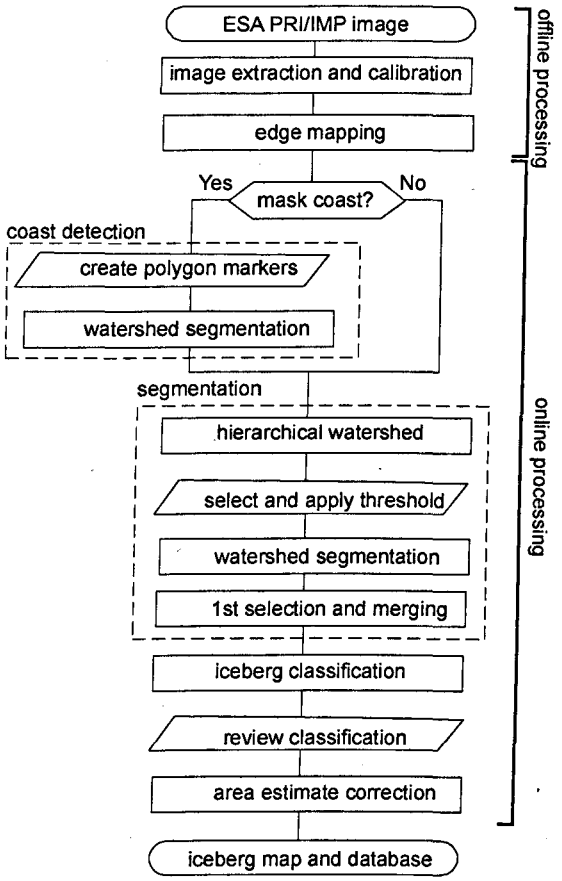

Figure 17 - Flowchart of the iceberg identification algorithm. Parallelograms indicate modules which require user intervention.

3.4.1.1 Pre-processing

The input SAR image is a calibrated backscattering coefficient (intensity) image projected in ground range. ERS and ENVISAT ASAR precision images, called PRI and IMP respectively, have a pixel width of 12.5 m but a resolution of approximately 26 m because of the image's significant spatial autocorrelation with first order neighbours [*Oliver and Quegan*, 1998 p. 105]. Unless the segmentation algorithm takes into account this image characteristic, there will be little loss of information by block averaging with a 2×2 pixel window and under-sampling by a factor of 2, which results in a pixel width of 25 m. Also, this reduces the memory requirements during processing.

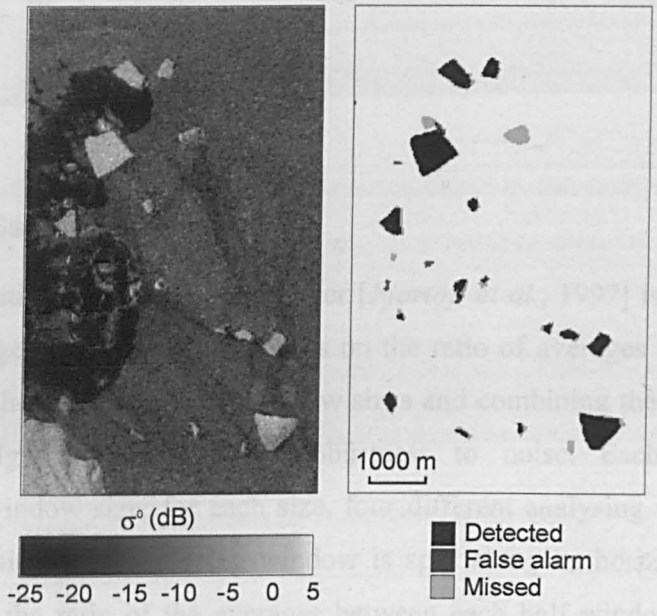

Figure 18 - Detail of SAR intensity image (from image A) on the left and results of automatic classification for comparison on the right. The SAR intensity image on the left shows a group of icebergs over sea ice background. The dark area on the left hand side is open water and the ice shelf appears on the bottom left. The results of the automatic classification (prior to user checking) show a dim iceberg on the middle top part of the image being missed and several false alarms caused by small fragments of sea ice.

3.4.1.2 Coastal masking

Coastal images might have large areas of ice sheets that could be erroneously identified as icebergs. A step is performed to detect and mask out the coastal limits. The image resolution is reduced by an additional factor of 4, block averaging by 4×4, followed by under-sampling, as the coast limits do not need to be very precise. The operator is asked to draw a polygon contained within each separate coastal section. The polygons are used as markers in watershed segmentation (Meyer and Beucher, 1990). This algorithm expands the initial polygon's limits until it finds the coastline, so only a rough positioning

of the polygon is needed. Finally, the binary mask is interpolated to its original size using a nearest neighbour algorithm and employed to mask out the coastal areas in the segmented image.

3.4.1.3 Segmentation

A multi-resolution ratio of averages filter [*Fjørtoft et al.*, 1997] is used to determine the edge map image. This method improves on the ratio of averages filter [*Touzi et al.*, 1988] by running the filter at several window sizes and combining the results in order to obtain precise edge positioning with robustness to noise. Each resolution level corresponds to a window size; for each size, four different analysing windows are used, one for each direction. The analysing window is split along its horizontal, vertical and diagonal axis, and the ratio of the averages between each half window is calculated as follows

$$r_d = \min\left\{\frac{\hat{\mu}_1}{\hat{\mu}_2}, \frac{\hat{\mu}_2}{\hat{\mu}_1}\right\}, \quad d = \{-, |, /, \backslash\}, \tag{3.1}$$

where $\hat{\mu}_1$ and $\hat{\mu}_2$ are the arithmetic mean values calculated on the half windows each side of the central pixel and d denotes each of the four directions. The index r_d has values in the interval $[0, 1]$ with low values indicating the presence of an edge. Four different values of r_d are calculated for each window size l. These are combined as follows

$$r_l = \min\{r_-, r_|, r_/, r_\backslash\} \tag{3.2}$$

in order to detect an edge in *any* of the four directions. The ratios are normalised across window sizes by dividing by the threshold T_l corresponding to a given probability of false alarm:

$$r_n = \frac{r_l}{T_l}. \tag{3.3}$$

The threshold T_l has to be calculated numerically from the expression of the probability of false alarm which we will now derive.

The probability density function of the ratio of averages, r, conditional to the contrast ratio R_1/R_2 between two homogeneous half-windows, for the case when R1/R2=1 is [*Touzi et al.*, 1988]:

$$p(r \mid ((R_1 / R_2) = 1)) = \frac{\Gamma(2NL)}{\Gamma(NL)^2}\left[2(r+1)^{-2NL}\right] r^{NL-1}, \tag{3.4}$$

where $\Gamma(.)$ is the gamma function, L the number of looks of the image and N the number of pixels in each half window. As an example, for a window size 5×5 each half window on each side of the central pixel has N=10. It follows that the probability of false alarm for a given threshold T between two homogeneous regions is

$$P_f(T) = \Pr ob(r < T, R1/R2 = 1) = \int_0^T p(r \mid 1) dr. \tag{3.5}$$

However this is only valid for the ratio calculated in one direction. For minimum over the four directions (3.2) the following empirical relation can be used [*Touzi et al.*, 1988]

$$P_{f4}(T) = 1 - (1 - P_{f4}(T))^3 \tag{3.6}$$

For each window size l, the threshold T_l has to be calculated numerically for a fixed P_{f4} value and used to normalise r_l between different window sizes (see (3.3)). This can be done by building a table of P_{f4} (T_l) for each window size. We used the number of looks L=5 from our estimates of the equivalent number of looks of the pre-processed ERS PRI intensity images as $mean^2/variance$ over homogenous areas [*Oliver and Quegan*, 1998, p. 95]. Lastly, the minimum value of r_n across all resolution levels is used to build the edge map. We used window sizes of 3×3 and 5×5 and a probability of false alarm of 1%. The resulting edge map is transformed by 50 *log (*map*)* to allow for an 8 bit representation consistent across different images.

The edges on the intensity images are likely to correspond to local minima of the edge map. These will be determined by running a watershed algorithm on the edge map. However, as this algorithm frequently leads to over-segmentation, we applied watersheds with basin dynamics [*Grimaud*, 1992] which defines a segment only when the basin in the edge map has a depth greater than a threshold value. The choice of this value is made easier by first creating a hierarchical watershed representation for a selected region [*Najman and Schmitt*, 1996]. This representation shows the segmented image for several thresholds.

The segmentation of a typical image results in a vast number of segments, both dim and bright, corresponding to homogeneous regions in the sea, sea ice or icebergs. A selection eliminates objects with average backscattering coefficient values below a threshold to accelerate further region-based computation. The threshold value of -10 dB was determined empirically and is a minimum limit for iceberg average backscattering coefficient (σ^0). Homogeneous objects that have been split by over-segmentation, can be merged by applying an optimal statistical decision, which takes into account the size and average intensity of every two touching segments [*Fjørtoft*, 1999a, p. 124]. Nevertheless, icebergs are three dimensional objects and the surface slope may alter the backscattering coefficient, breaking the homogeneity assumption and making this approach less successful. In addition, the statistical criteria just mentioned can be computationally expensive to calculate. Therefore, a simple merging criterion was defined so as to merge any two objects that share more than a certain proportion of their respective borders and do not differ by more than a certain value in average intensity. A limit of 15% for the shared contour and 2 dB for the modulus of the intensity difference proved effective for most cases.

3.4.1.4 Classification

The segmentation step returns many segments that correspond to homogeneous areas, both with high and low intensity values, but not all are icebergs. Sea ice and iceberg shadows are the most frequent false alarms. The classification step uses the segment database to select the ones corresponding to icebergs. A simple rule classifier was defined by inspecting the characteristics of the manually-defined objects from image A. These characteristics are described in Table 4: square root of the area; major and minor axes; position; average σ^0 and time of image acquisition. A segment is classified as an iceberg if all the values for these variables are within the ranges observed for manually selected objects in image A. Parameter "area" eliminates objects too small to be confidently identified, and parameters "major/minor axis" and "perimeter/sqrt(area)" help eliminate long and often convoluted bright sea ice ridges.

Table 4 – Parameters and limits used in the iceberg classifier. Each segment was classified as corresponding to an iceberg if all of the above parameters fell within the limits. The limits were the ones observed for the icebergs manually segmented in image A.

Parameter	Description	Limits used in iceberg classifier
average σ^0 (dB)	Estimated backscattering coefficient in dB: $10 \cdot \log_{10}\left(\frac{\sum_{all\_the\ pixels} Intensity(x,y)}{Number\_of\_pixels}\right)$	[-9.24, +∞)
area (m^2)	Number of pixels multiplied by pixel size (25×25).	[1.5×10^4, +∞)
major/minor axis	Ratio between length and width the object.	[0, 3.99]
perimeter/area$^{1/2}$	Higher values correspond to a more intricate shape.	[3, 4.4]

3.4.2 Iceberg tracking

In order to perform tracking, objects previously identified as icebergs must be matched between images acquired at different times, and possibly different locations. This was done by ranking iceberg pairs in terms of size similarities followed by a finer ranking in terms of shape resemblance. For each image, an iceberg database is produced containing the same object parameters already used for iceberg identification (see Table 4). The square root of the area and major and minor axes are components of the feature vector, and the Euclidean distance between feature vectors is calculated and ranked for all pairs of objects contained in different images. The objects with a value of this measure (Euclidean distance) below 500 m were tested for shape matching.

Each object with a possible match had its shape extracted by performing a one dimensional shape representation [e.g. *Jain*, 1988]. This is obtained by following the object's contour and recording, for each pixel, the distance and direction from the object's centroid. The resulting distance/direction vector is then interpolated linearly and re-sampled every 5 degrees to yield a shape vector. This describes the distance from the edge to the centroid for 72 (360/5) regularly distributed directions. All pairs of geometrically similar objects are then compared by shifting one of the contour vectors until a maximum

correlation is obtained. This eliminates the effect of rotation on the object matching. Finally, the Euclidean distance between the two shape vectors is calculated. This contour representation is invariant to rotation and robust to noise.

The pair-wise shape distances are sorted in descending order and used to match objects. All pairs already matched are excluded from further searching. In this way optimal matches can be found, independent of the order followed. A report is produced including the bitmaps of images of higher scoring object pairs to be checked, and if necessary corrected, by a human operator. Figure 19 shows the coverage of three images with the position of all the detected icebergs.

3.4.3 Implementation notes

The algorithm was implemented in Matlab (The Mathworks, Inc.) making use of the Image Processing Toolbox. All filtering used the fast Fourier Transform technique (FFT) for greater performance. Object analysis (averaging and contour description) was done on the smallest images that can contain the object instead of on the whole image. Image calibration - using the European Space Agency's BEST software - and edge mapping takes about 20 minutes to perform on an Intel Xeon workstation, but as these tasks can be run in the background, without any user intervention, time requirements are not thought to be relevant. Running the online part of the identification algorithm takes approximately 15 minutes on the same machine and uses 1 to 1.5GB of memory in 64 bit representation (with a 64 bit datatype). The tracking algorithm takes below one minute per image pair. The user intervenes to draw the watershed markers inside coastal objects, to choose a basin dynamic threshold for the segmentation and to exclude the false alarms resulting from classification and from tracking.

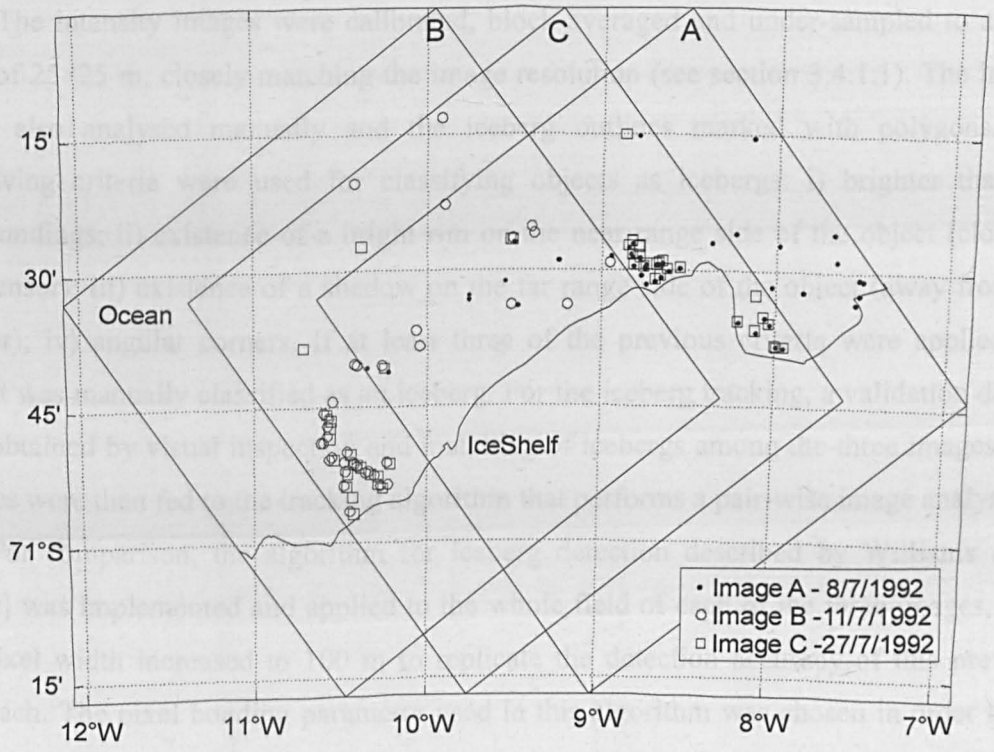

Figure 19 – Coverage of the three SAR images with coastline and position of detected icebergs. Discrepancies in iceberg detected in each image are mostly due to icebergs drifting between acquisitions.

3.5 Performance evaluation

The technique was tested on three wintertime ERS-1 PRI images around Kapp Norvegia, in the south-eastern Weddell Sea (image details in the Appendix). The modelling results from Gladstone *et al.* [2001] indicate this to be an area where a large number of icebergs, having calved from the ice shelves between the Fimbul and the Amery ice shelves, are driven close to the coast. The three images have a partial overlap which allows objects to be matched between images (see Figure 19). The discrepancies in detected icebergs between the three images are mostly due to iceberg drift on the coastal current.

The intensity images were calibrated, block averaged and under-sampled to a pixel size of 25×25 m, closely matching the image resolution (see section 3.4.1.1). The images were also analysed manually and the iceberg outlines marked with polygons. The following criteria were used for classifying objects as icebergs: i) brighter than the surroundings; ii) existence of a bright rim on the near range side of the object (closer to the sensor); iii) existence of a shadow on the far range side of the object (away from the sensor); iv) angular corners. If at least three of the previous criteria were applied, the object was manually classified as an iceberg. For the iceberg tracking, a validation dataset was obtained by visual inspection and matching of icebergs among the three images. The images were then fed to the tracking algorithm that performs a pair-wise image analysis.

For comparison, the algorithm for iceberg detection described by Williams *et al.* [1999] was implemented and applied to the whole field of each of the three images, with the pixel width increased to 100 m to replicate the detection accuracy of this previous approach. The pixel bonding parameter used in this algorithm was chosen in order to get the best results (0.2 for all the images). Segments were classified as icebergs for values of σ^0 larger than -8 dB. Because the results are validated by a user, we are mostly concerned with misses and not with false alarms, but using a lower threshold would lead to thousands of segments being classified instead of the 200 to 500 false alarms observed.

3.5.1 Segmentation accuracy

The segmentation step was performed on the three images with the threshold being selected by inspection of the hierarchical watershed representation. The automatically determined segments were compared with the ones obtained manually and classified in the following categories: "Correctly segmented" if the contour is similar to the one obtained manually; "Small" if the resulting segment has less than half the area of the manually determined; "Over-segmented" if several segments were created for one iceberg; "Under-segmented" if the object was agglomerated with the surroundings or other objects; and "Miss" if no corresponding segment was detected. The results in Table 5 show that the majority of objects were correctly segmented. A number of false alarms as large as to

double the total number of icebergs were produced; these will have to be excluded manually by the operator. The summed area of the correctly segmented objects was greater than 90% of the total iceberg area for all images, showing that the errors occurred mostly on small objects - nevertheless, as we will see shortly, the area of objects "Correctly segmented" was underestimated. The most frequent problem corresponded to the category Small, when only the brighter part of the iceberg was segmented. Under-segmentation was rare.

Figure 20 shows the detectability, or the proportion of objects detected, and the number of objects per image was plotted as functions of the square root of the iceberg area. As expected, the detectability increases with iceberg size, although the number of objects larger than 0.5 km^2 was small. The system detects almost all objects with area above 0.35 km^2 and half the objects around 0.1 km^2. In the same graph the detectability resulting from the application of the algorithm by Williams *et al.* [1999] is also included for comparison. The performance of this algorithm can be seem to be similar to the one presented here, performing slightly better at the 0.16 km^2 class and decaying more rapidly for objects smaller than 0.09 km^2 due to the algorithm working with images with pixel size of 100 m. Samples sizes for objects above 0.6 km are small so the detectability curves should be read with care. For instance, the failure of the method by Williams *et al.* in detecting the only object in image B in the 0.6 km class produced a 0 detectability score.

Table 5 – Number of correctly segmented objects before manual verification. The well defined icebergs account for around 90% of the area of the manually defined icebergs. The following segmentation thresholds were used for images A, B and C: 25, 30 and 29.

Image	A	B	C
Correctly segmented	42	25	37
Small	1	5	4
Ovesegmented	0	1	3
Undersegmented	0	0	1
Miss	18	23	12
False alarm	66	108	81
TOTAL OBJECTS	61	54	57

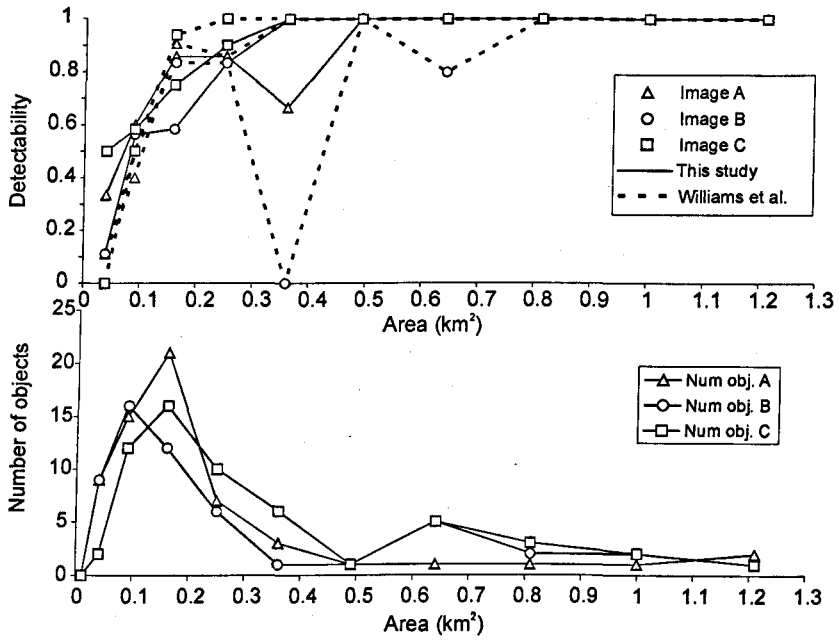

Figure 20 – (Top) Variation of iceberg detectability with iceberg size for both the algorithm here presented and the one presented in Williams et al. [1999]; (Bottom) Distribution of number of objects in each image per area class.

Different human operators will likely choose different values for the threshold by looking at the hierarchical watershed representation. In our experience this range was up to 10 units (the threshold is non-dimensional). Therefore, a sensitivity analysis was conducted to evaluate the effect of varying the segmentation threshold with a range of 20 units for image A. The results in Figure 21 show that there is little variation of the number of correctly segmented icebergs, especially if care is taken to choose a low threshold value. The downside then is the larger number of false alarms that must be excluded manually at the verification stage.

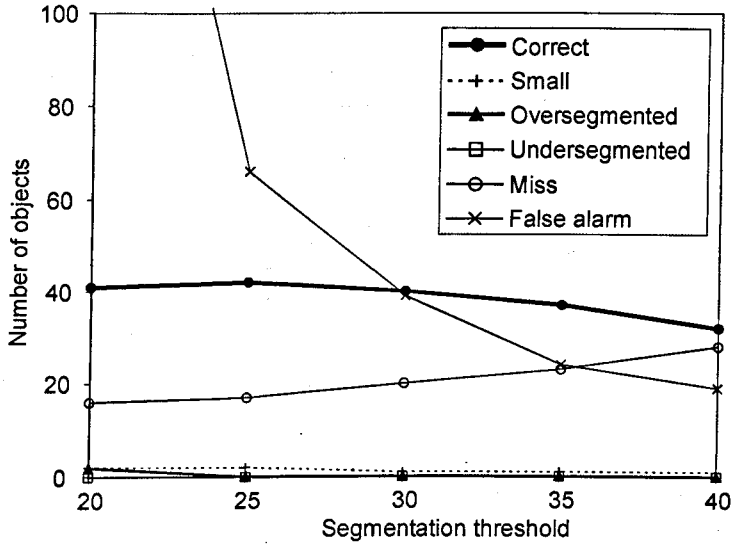

Figure 21 - Icebergs detection algorithm's sensitivity to segmentation threshold (basin dynamic) performed on image A.

3.5.2 Area estimate

The accuracy of the area estimate for each segment was assessed by comparing it with the area obtained from the manual segmentation. The results are plotted in Figure 22 with a linear regression fitted to the data. It can be seen that the area is underestimated by as little as 10% for 1 km^2 icebergs, with the error increasing for smaller objects. The intensity image and segmentation results for a typical iceberg shown in Figure 23 illustrate why this happens. The surrounding pixels tend to exhibit lower intensity values and are ignored by the segmentation algorithm. The lower values are due to steeper slopes and contamination from the background. This is more noticeable on the far range side of the object, right in this case, where, as the slope approaches the incident wave direction, the backscattering intensity is reduced.

The final aggregate iceberg area estimates for the three images are presented in Table 6. Around 70% of all the iceberg pixels are classified correctly. The area estimates for each iceberg are further improved by applying the linear correction extracted from image

A. False alarms are virtually eliminated by manual verification. For our example images, this results in the total area being underestimated by 10 to13%.

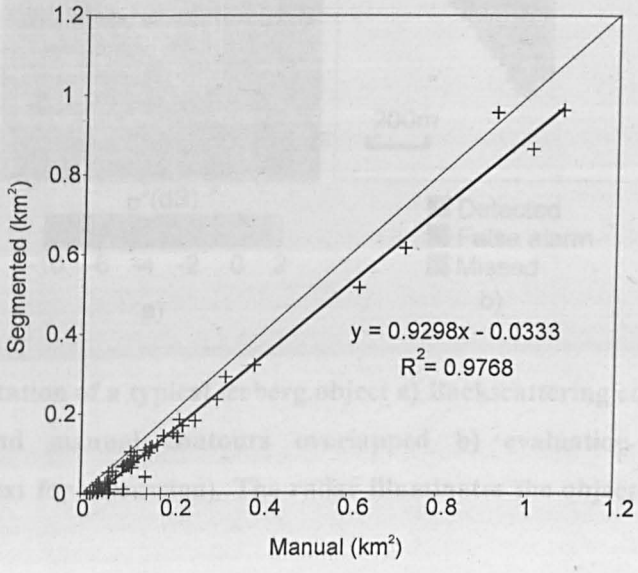

Figure 22 – Relationship between areas of manually and automatically segmented icebergs on image A. The thin line represents an unbiased estimate and the thick line a linear regression. The linear regression shows that the algorithm underestimated the areas by about 10%, although this effect is more important for smaller icebergs.

Table 6 - Comparison of automatic with manual iceberg identification. False alarm category is reduced to zero after verification.

Image	A	B	C
	Classification error discriminated (before verification) (km^2)		
Correct	7.40	7.87	10.47
Miss	3.35	3.56	4.32
False alarm	2.45	5.44	3.18
	Total iceberg area (km^2)		
Manual	10.75	11.43	14.92
Automatic after verification and with area correction	9.64	10.23	13.06

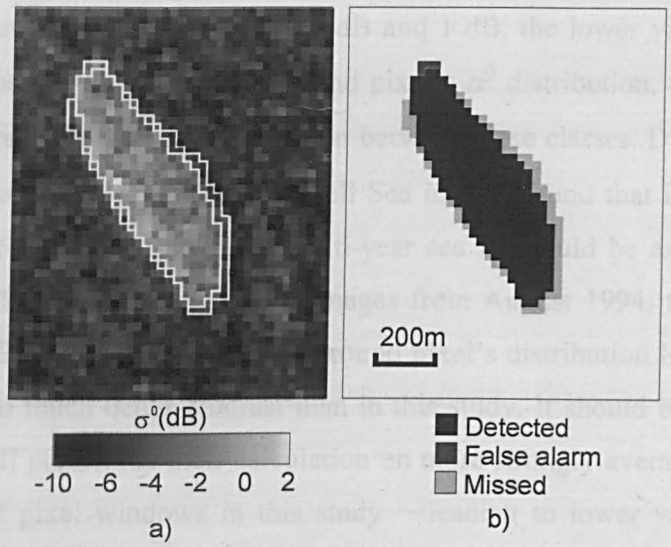

Figure 23 – Segmentation of a typical iceberg object a) Backscattering coefficient (• 0) image with automatic and manual contours overlapped b) evaluation of the automatic segmentation (see text for discussion). The radar illuminates the object from the left of the page.

Table 7 - Comparison on automatic matching with manual.

	Images Compared		
Icebergs matched	A-B	A-C	B-C
Manual (total)	7	19	20
Automatic (total)	13	18	15
Correct	7	13	12
Incorrect	5	3	3
Missed	0	6	8
Possible	1	2	0

3.6 Discussion

The ability to identify an iceberg on a SAR image relies heavily on the iceberg being brighter than the surroundings. On the three SAR images used as examples, there is a significant overlap between the values of σ^0 for background pixels and σ^0 averaged for the

icebergs. The latter had values between −9 dB and 1 dB, the lower value corresponding only to the 75% percentile of the background pixel's σ^0 distribution. Other studies, also for winter conditions, gave a better separation between these classes. Drinkwater's [1997] study using ERS observations of the Weddell Sea in July found that iceberg average σ^0 varied between −6 and 1 dB, although multi-year sea ice could be as bright as −2 dB. Young *et al.* [1998] found, in three SAR images from August 1994, that icebergs were brighter than -6 dB while 99% of the background pixel's distribution had values below -10.5 dB, leading to much better contrast than in this study. It should be pointed out that Young *et al.* [1998] performed their calculation on more strongly averaged images – 8×8 instead of the 2×2 pixel windows in this study – leading to lower variance. But even reducing the resolution of our images in the same way, the 99% percentile is only lowered from −5dB to between −6 and −7dB, depending on the image.

A common cause for reduced iceberg σ^0 values is the melting of the surface, as this increases the moisture content and leads to shallower penetration of the microwave radiation [*Rott et al.*, 1993]. However, the air temperatures of the study site at the time of the image acquisition were not high enough for this: the warmest temperature in NOAA NCEP/NCAR data for the acquisition days was -7° C. A reason for some icebergs in our images having low σ^0 values can be the fact that a large proportion were stranded and may have suffered erosion through breaking and rollover, and multiple melting-refreezing episodes in previous summers. As for the background, being formed mainly by sea ice, a higher concentration than normal of rough or 2^{nd} year sea ice could explain the high σ^0 values observed.

Bright areas of sea ice ridges and land-fast ice are also segmented by the algorithm. Because of this, the average σ^0 distribution for non-icebergs has even more overlap with icebergs than the background σ^0 distribution. The area versus σ^0 graph in Figure 24 shows that this separation is not clear even for icebergs as large as 0.1 km^2, or about 350 m in length. This was the reason that led us to include more geometric parameters in the classifier, but still it requires a human validation of the false alarms. The bright background and faint icebergs present in these images lead us to expect that the detectability curves plotted in Figure 20 should be seen as a worse than average scenario for this algorithm's performance. This is supported by the results of the algorithm by

Williams *et al.* [1999] presented on the same figure that also performed worse than expected: under more favourable circumstances the latter was described as being capable of detecting virtually all icebergs with area larger than 0.06 km^2 while with our images both algorithms detect around 50% of the icebergs of this same size. Also, our algorithm yielded several times less false alarms than the Williams *et al.* algorithm, shortening the time required by the operator to check the results.

Most of the matched objects were stranded icebergs, as can be seen in the clusters of icebergs observed in two or more images (Figure 19). Therefore they didn't rotate between observations. Although the matching algorithm is robust to rotation, the SAR foreshortening phenomenon - compression of features towards the radar – will cause some variation in the iceberg shape as it rotates, potentially making matching somewhat more difficult. The small numbers of moving icebergs in this set of images doesn't allow us to fully evaluate the effect of rotation in the matching accuracy.

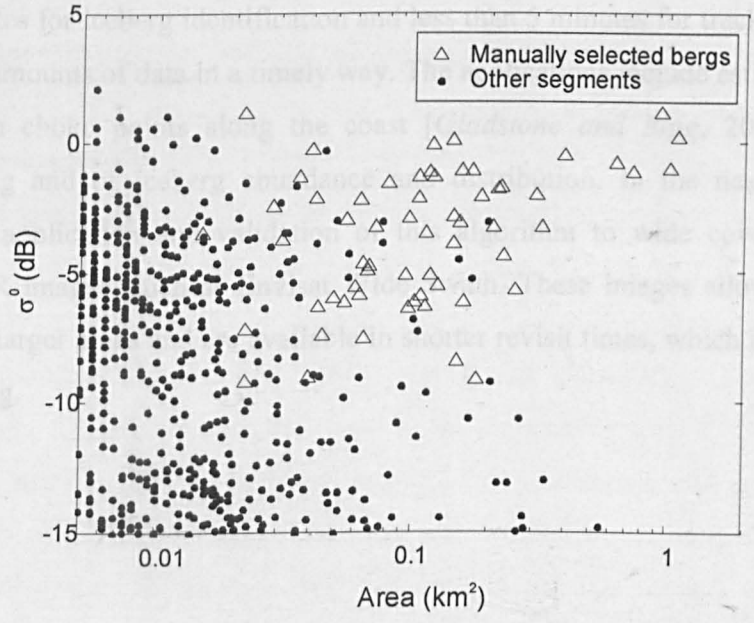

Figure 24 – Area and σ^0 for manually segmented icebergs and non-iceberg segments contained in image A. Icebergs are not separable from other segments by the values of σ^0 and area alone.

Icebergs drifting in the Antarctic coastal current can move at an average speed of 0.1 to 0.2 ms^{-1} [*Gladstone and Bigg*, 2002; *Tchernia and Jeannin*, 1984]. This means that an iceberg can cross the 100 km of an ERS SAR image width in as little as 6 days. Normal revisit times for ERS and ENVISAT are 35 days for the same geometries and 16 days between an ascending and a descending pass. Images A, B and C have only 3 and 16 days between acquisitions and are all ascending passes, but have different footprints. Radarsat and ENVISAT satellites have SAR sensors that can be pointed at the same location with as little as 3 days separation. However, the looking angle and possibly the pass direction will differ between acquisitions potentially making object matching more difficult. Alternatively, using wider coverage, lower resolution images such as RADARSAT Scansar wide or ENVISAT Wide Swath multiplies the image width by 4 reducing the resolution by a similar factor. Icebergs are more likely to be re-sighted for the same revisit time but smaller ones will be missed.

The computer-based method presented here can be used to analyse iceberg distribution and movements in high resolution SAR images. The online processing time of 15 to 30 minutes for iceberg identification and less than 5 minutes for tracking allows it to process large amounts of data in a timely way. The applications include estimating iceberg fluxes through choke points along the coast [*Gladstone and Bigg*, 2002], studies of iceberg calving and of iceberg abundance and distribution. In the next chapter it is presented the application and validation of this algorithm to wide coverage, medium resolution SAR images, such as Envisat Wide Swath. These images allow the effective monitoring of larger areas and are available in shorter revisit times, which is important for iceberg tracking.

Chapter 4 Antarctic Iceberg distribution and movements from SAR images

4.1 Introduction

There is nowadays the potential for including icebergs in coupled regional or global ocean models. Nevertheless, the knowledge of basic quantities such as the total mass of icebergs in the Southern Ocean or their longevity is poor and has seen little improvement over the last 20 years.

The population of icebergs in the Southern Ocean has been estimated to be around 300 000 [*Orheim*, 1985a] ranging in length from 25 m (definition of iceberg by [*Wadhams*, 2000]) to 200 km, and distributed over an area of over 20×10^6 km^2. Icebergs can move at speeds of over 20 km per day and rollover or break-up in a matter of minutes. These factors add up to make surveying the population a particularly demanding task.

Here we study the distribution and movements of icebergs on SAR images using the computer-based method already presented. The method is applied to larger footprint, reduced resolution, ENVISAT Wide Swath images, and tested against both higher resolution PRI images and field observations. The method was applied to two SAR mosaics covering the coastal Southern Ocean to obtain a synoptic view of the iceberg distribution close to the coast for a short period in time. This is compared with ship-based observations around East Antarctica. The observed size distribution is studied using a conceptual model for iceberg decay to learn about the calving size distribution and the relative importance of break-up and wall erosion. The movement, and consequently the flux of icebergs, over a short period of time was studied by tracking icebergs across several SAR images of the Eastern Weddell Sea. In the last section we make some recommendations for further improving the knowledge of icebergs in the Southern Ocean using satellite remote sensing.

4.2 Iceberg detection accuracy

In Chapter 3 we have presented a computer-based method for detecting icebergs on SAR images. This was tested on regular resolution SAR images – PRI/IMP – which have a footprint of 100×100 km (see Table 8). Wide swath (WS) images have been available since 2002 with the ENVISAT satellite, and allow for greater coverage in exchange for reduced spatial resolution. The image coverage is a great advantage for detecting icebergs as larger areas can be surveyed, but it must be tested if the minimum iceberg size detected remains satisfactory for the Antarctic population of icebergs. In the following section the algorithm is tested on WS images by comparing with icebergs manually detected on PRI images.

Both in Chapter 3 and the in following section the algorithm's detection accuracy was tested by comparison with manual classification of images. There will be situations when small icebergs with wet surfaces from melting or a rollover will have a backscatter so low that they will be missed in the manual classification. In addition, multiyear sea ice floes might yield a backscatter as high as icebergs. This can be a problem with smaller and more eroded icebergs which lack the straight edges and tall ice cliffs of larger tabular ones, and thus, might be impossible to separate from sea ice floes. We conducted fieldwork in the Southern Ocean to compare iceberg identification on SAR images with ship-based observations.

The thickness of calving icebergs varies with the outlet glacier or ice shelf. Gladstone [2001] measured the thickness at the calving front for the main calving sites along the Antarctic coast from the digital elevation model by Bamber and Bindschadler [1997] and found this to be typically 250 m although it could be as large as 550 m in the Filchner Ice shelf or as little as 150 m in the George VI Ice Shelf. He synthesised the dimensions of iceberg into 9 size classes with a maximum thickness of 250 m. We calculated iceberg volume from iceberg area using the following function fitted to the above mentioned iceberg categories (see Figure 25):

$$Z = 250 - 215 \cdot e^{-4.63\times10^{-5}\cdot A} \qquad (4.1)$$

where Z is the iceberg thickness, and A is the iceberg area as measured from the SAR images. For smaller icebergs smaller than 0.1 km^2 this is a better approximation than

assuming a constant ice thickness. Nevertheless, comparison with observational data for the Weddell Sea in Figure 25 shows that there is a large variability in iceberg thickness. The iceberg thickness will change geographically due to both the thickness of the calving front and the age of the icebergs, and its errors will propagate to the estimates of ice volume from SAR observations.

The density of ice shelves and tabular iceberg changes vertically, from around 100 kg m^{-3} for recently fallen snow to the density of ice, 917 kg m^{-3}, below 50 to 100 m [*Rist et al.*, 2002]. The average density will change with several factors, including the iceberg thickness and erosion. We used the average density of 850 kg m^{-3}, as measured for tabular icebergs in the Ross Sea [*Keys et al.*, 1990; *Keys and Fowler*, 1989], to convert estimated ice volume into mass.

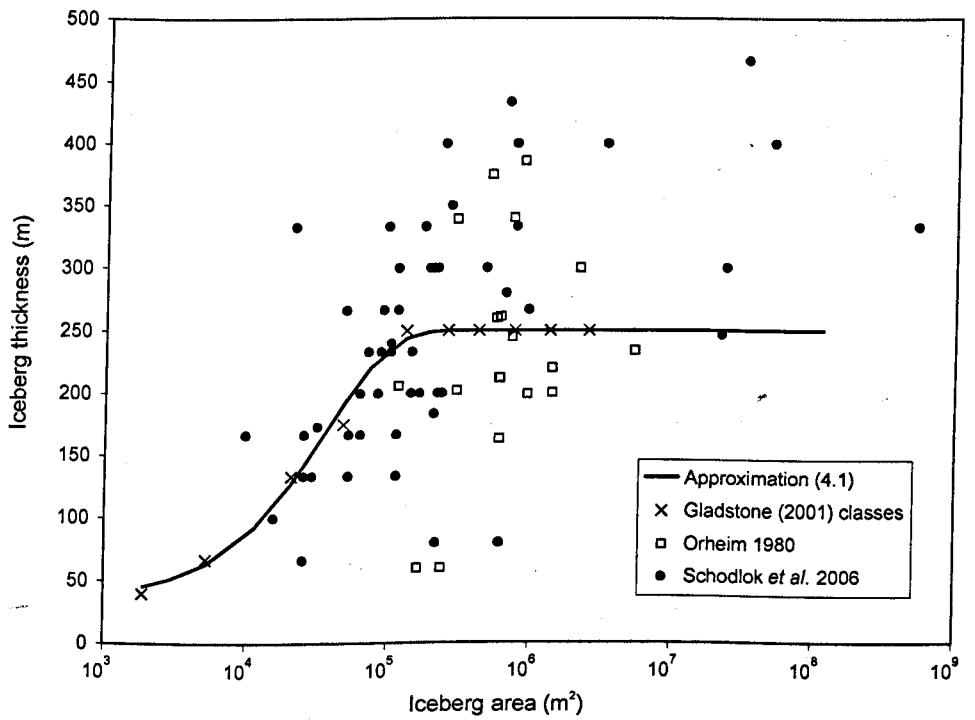

Figure 25 – Comparison of the estimate of iceberg thickness from iceberg area from the functional approximation (4.1) with observational data for the Weddell Sea [Orheim 1980; Schodlok *et al.* 2006]. Function (4.1) was fitted to the iceberg classes from Gladstone [2001].

Table 8 - Differences between narrow and wide swath images on European Space Agency satellites.

	Ground coverage	Number of looks	Resolution	Pixel size	Polarisation
ERS-1/2 PRI ENVISAT IMP	100 × 100 km	>3	~30 m	12.5 m	VV
ENVISAT Wide Swath	400 × 400 km	11.5	150 m	75 m	HH or VV

4.2.1 Size detectability of wide swath images

The study area is a section of Ruppert Coast, on the Pacific sector of West Antarctica, where the Land Glacier calves a large number of small icebergs (Figure 26). This poses a good problem for testing the detection limits of the lower resolution wide swath images. One wide swath image and a strip of three narrow swath images were obtained for the area, having been acquired 29 hours apart (image details are in the Appendix). The study area was restricted to the overlap of both types of images and a rough coastal mask was created to exclude the ice sheet and the highly crevassed glacier tongue. The cold winter conditions meant that the icebergs within 30 km from the coast are held together by land-fast sea ice. Further away from the coast, on the top right corner of Figure 26, the icebergs moved up to 5 km between the two acquisitions.

The narrow swath images were used to manually identify 3179 icebergs ranging in size from 25 m to 10 km in length. There are a large number of icebergs with sizes starting at 2×10^4 m^2 (Figure 27), which is equivalent to the resolution of WS images of 150 m. The iceberg detecting algorithm was applied to the overlapping part of the wide swath image which resulted in 2956 icebergs being detected, of which 2504 match the manual detections (see Table 9). Defining detectability as the fraction of objects correctly detected, we calculated and plotted this quantity as a function of the object's area (Figure 28). Icebergs of 0.05 km^2 have a detectability of only 50%. This increases steadily with size and icebergs with 0.25 km^2 or around 500 m in length have a detectability of over 90%. The detectability decreases slightly for the largest size class due to icebergs moving in between the acquisitions and failure to detect a few densely crevassed icebergs.

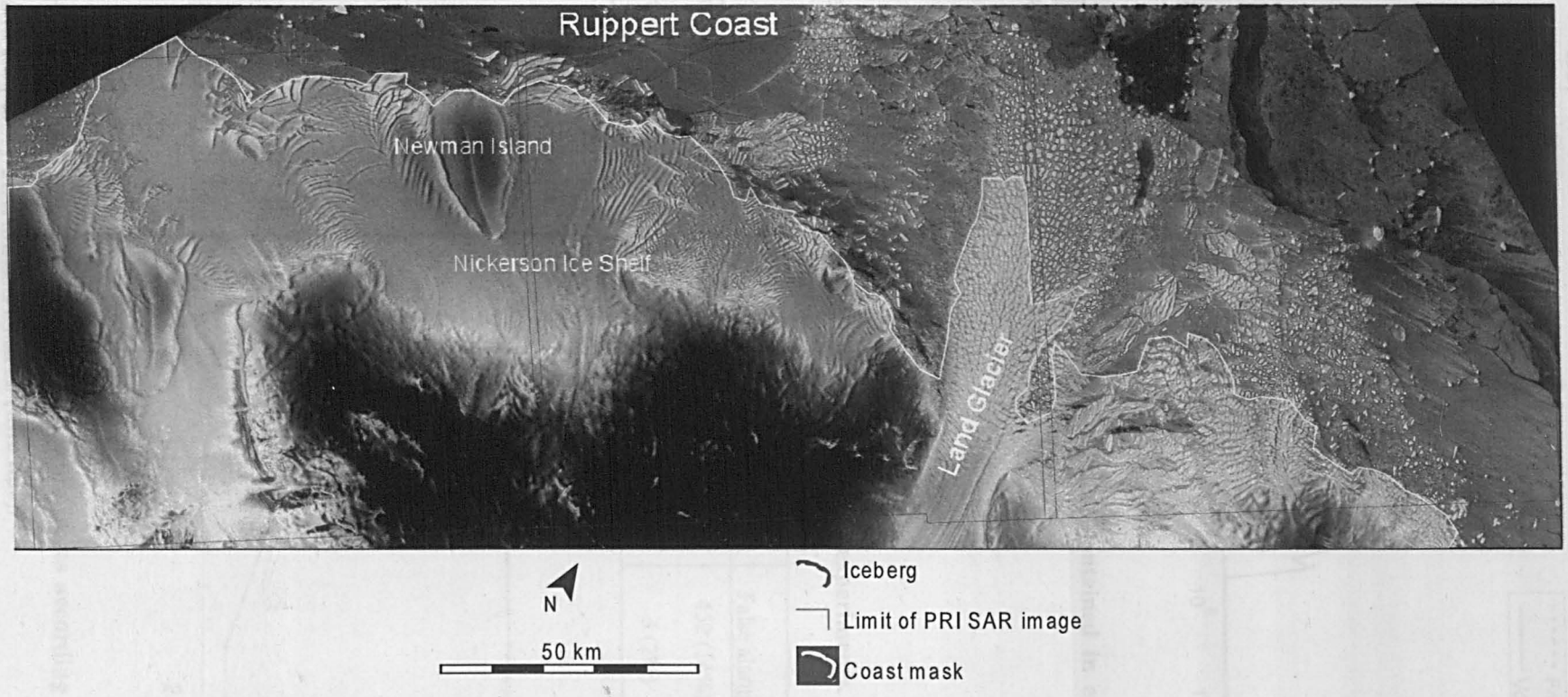

Figure 26 – Section of the wide swath SAR image used for WS to PRI comparison, showing limits of the three PRI images and the manually detected iceberg, Ruppert Coast, West Antarctica. The centre of the image is approximately at 75.5°S 144°W.

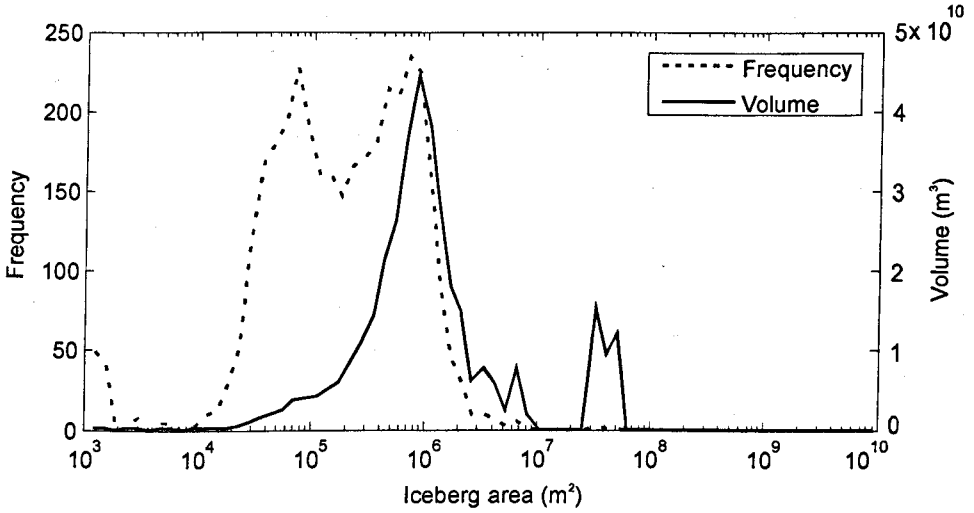

Figure 27 - Iceberg frequency and total volume contained in each size class for the Ruppert Coast study area.

Table 9 - Summary of results form the two validation experiments.

	Correctly detected icebergs	Missed icebergs	False alarms	Correctly detected volume (m^3)
Ruppert Coast winter	2504 (79%)	675 (21%)	452 (14%)	275×10^9 (88%)
Eastern Weddell summer	112 (90%)	12 (10%)	3 (2%)	16.6×10^9 (97%)

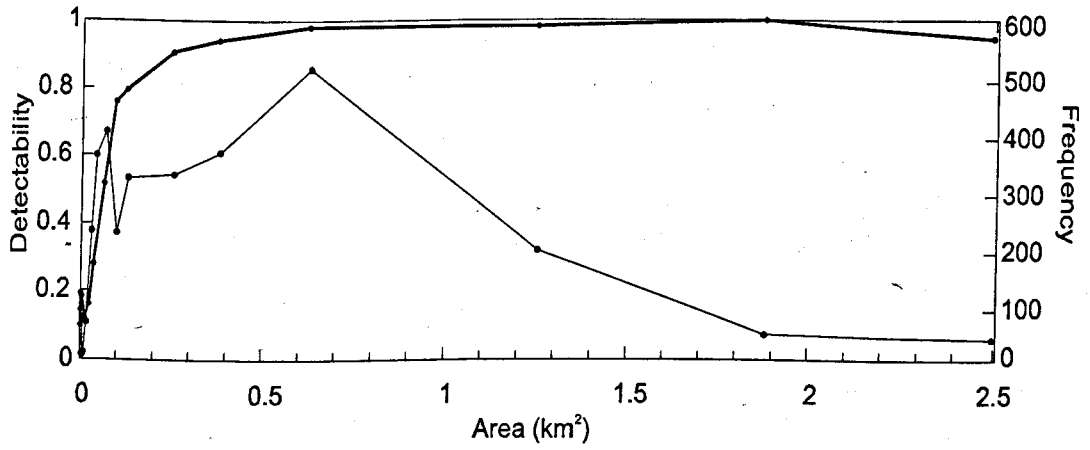

Figure 28 - Iceberg detectability on Wide Swath imges according to iceberg area (thick line) and frequency distribution by area (thin line).

The total percentage of objects missed is 21% but as smaller objects tend to be missed, the error in the total iceberg volume for this population of icebergs is smaller at 12%. There were also 452 false alarms, or 14 % of the number of manually detected icebergs. Nevertheless, false alarms have less impact in the results as these can be more easily edited out by the user than missed icebergs can be detected and segmented.

4.2.2 Field Validation

The method consists of mapping icebergs from a ship along a transect and use the observations to validate detections of icebergs on a SAR image acquired at approximately the same time. The ship-based K band radar and an on-board Global Positioning System were used to detect and locate icebergs larger than 25 m in length. When visibility conditions allowed, the icebergs were photographed with a fixed telephoto lens and measured on the photo. Knowing the distance from the ship from the radar range measurement it was possible to estimate the iceberg's apparent length. The size and photograph, or if this was not available the iceberg description (tabular, pinacled, weathered, sloping, etc...) helped to confirm the matching between ship-based and satellite observations.

The iceberg transects were conducted along the Weddell Sea Coast on the maritime route to Halley Base (Figure 29). Apart from the above mentioned logistical reasons, the Eastern Weddell was chosen due to having a large coastal flux of icebergs from East Antarctica that drift towards the Weddell Sea. The surveys were conducted on the 19th and 20th of December 2004 while the ship RRS Ernest Shackleton was approaching Halley. Although the Austral Summer is when the access is easier, this is not the best time to detect icebergs on SAR images; at melting temperatures the surface of the ice increases its moisture content, reducing its backscattering coefficient [*Rott et al.*, 1993] and making icebergs more difficult to separate from the background..

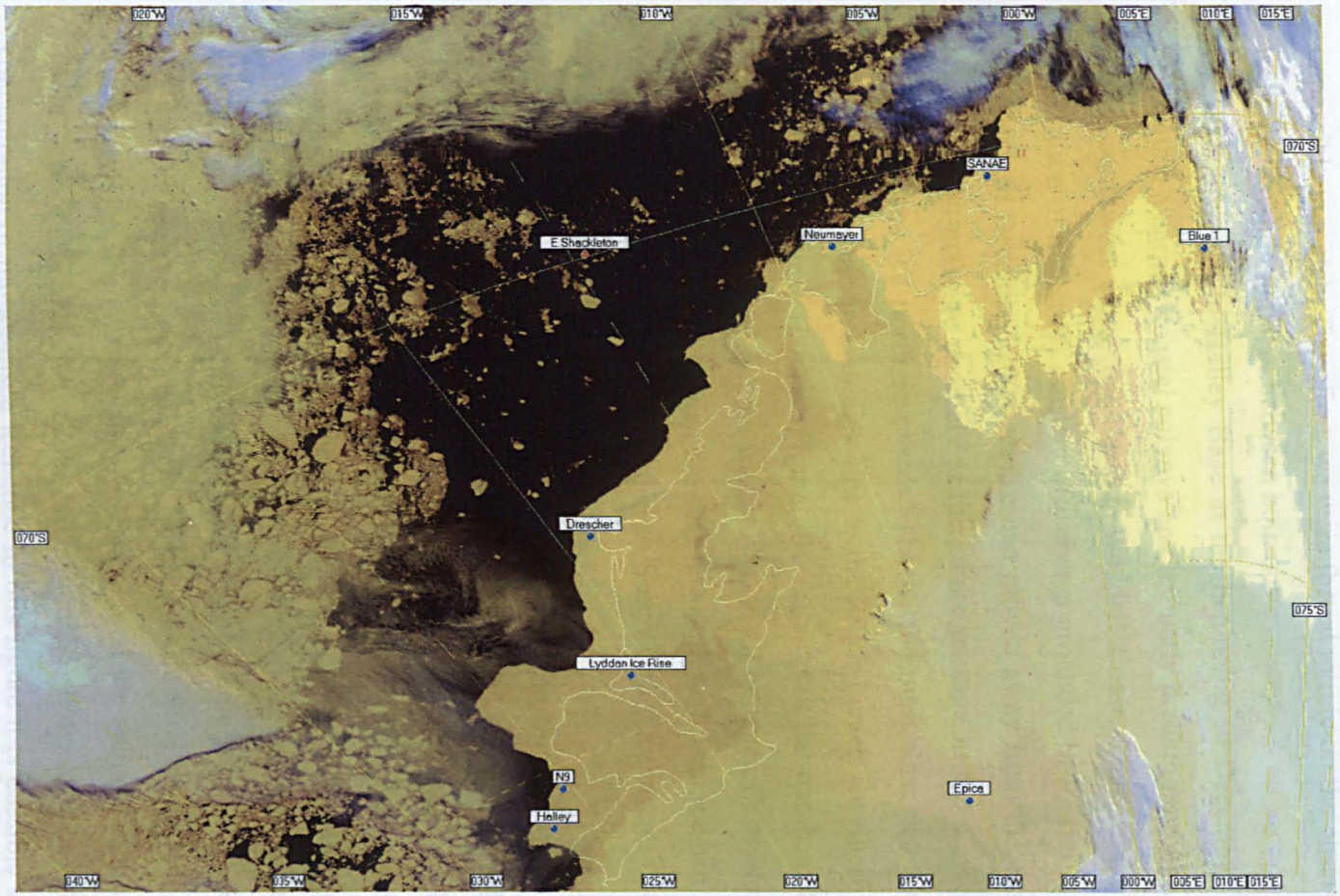

Figure 29 – Terra/Aqua optical satellite image of the Eastern Weddell Sea, acquired on the ship's HRPT terminal on the 19th of December 2004. The RRS Ernest Shackleton (top centre) is approaching Halley Base (bottom of the image) taking advantage of the large coastal polynya, atypical this early in the Summer.

The SAR images were acquired on the 23rd of December 2004, three days after the survey (see appendix for image details). As icebergs drifting on the Antarctic coastal current can move at speeds of 0.2 m s^{-1}, this time difference means that an iceberg can be tens of kilometres from its first recorded position and may therefore be impossible to match. Therefore, we were forced to rely on the observation of grounded icebergs that did not move between both observations

The approach to Halley Base at the beginning in December normally involves negotiating a narrow coastal polynya and regularly breaking through sea ice as the ship moves southwest along the Eastern Weddell Coast. This would have allowed the observation of numerous clusters of icebergs grounded or locked in land-fast ice, near the coast. In December 2004 sea ice had moved away from the coast (see Figure 29) due to a high pressure anomaly at the Drake passage in the previous weeks that had pushed the sea ice north-eastwards. The RRS Ernest Shackleton was able to travel through open-water in a straight line to the Riiser-Larsen Ice Shelf and only followed the coast for around 100 km (Figure 30). As a result the number of icebergs detected from the ship in the study area was only 129, all between Cape Norvegia and Halley. On the 29th of December, when the ship left Halley, the sea ice had further melted and moved away, and as the ship headed to South Georgia through open water very few icebergs were sighted.

The classification algorithm was run with the threshold for the backscattering coefficient, σ^0, of the iceberg class set at -13.5 dB. The number of icebergs detected was 112 plus 3 false alarms caused by sea ice floes that were excluded manually. A manual classification of the SAR images was also made using the ship-based observations to confirm the icebergs' presence and to assert the separation between icebergs and sea ice. Only objects present on the SAR images and verified by the ship-based observations were classified as icebergs. There were 124 icebergs (see Figure 30) and 50 sea ice floes detected. This results in 90% of correct identifications for icebergs which is equivalent of 97% of the total ice volume, as smaller icebergs (see Table 9) were more likely to be missed. Figure 31 shows an area with a relatively high concentration of immobilised icebergs. In this figure it is possible to see land-fast ice attached to the ice shelf cliff. Icebergs can be difficult to segment if embedded in land-fast ice and recently broken land-fast ice floes can be confused with icebergs. Therefore we also analysed the pixel statistics of the land-fast ice areas.

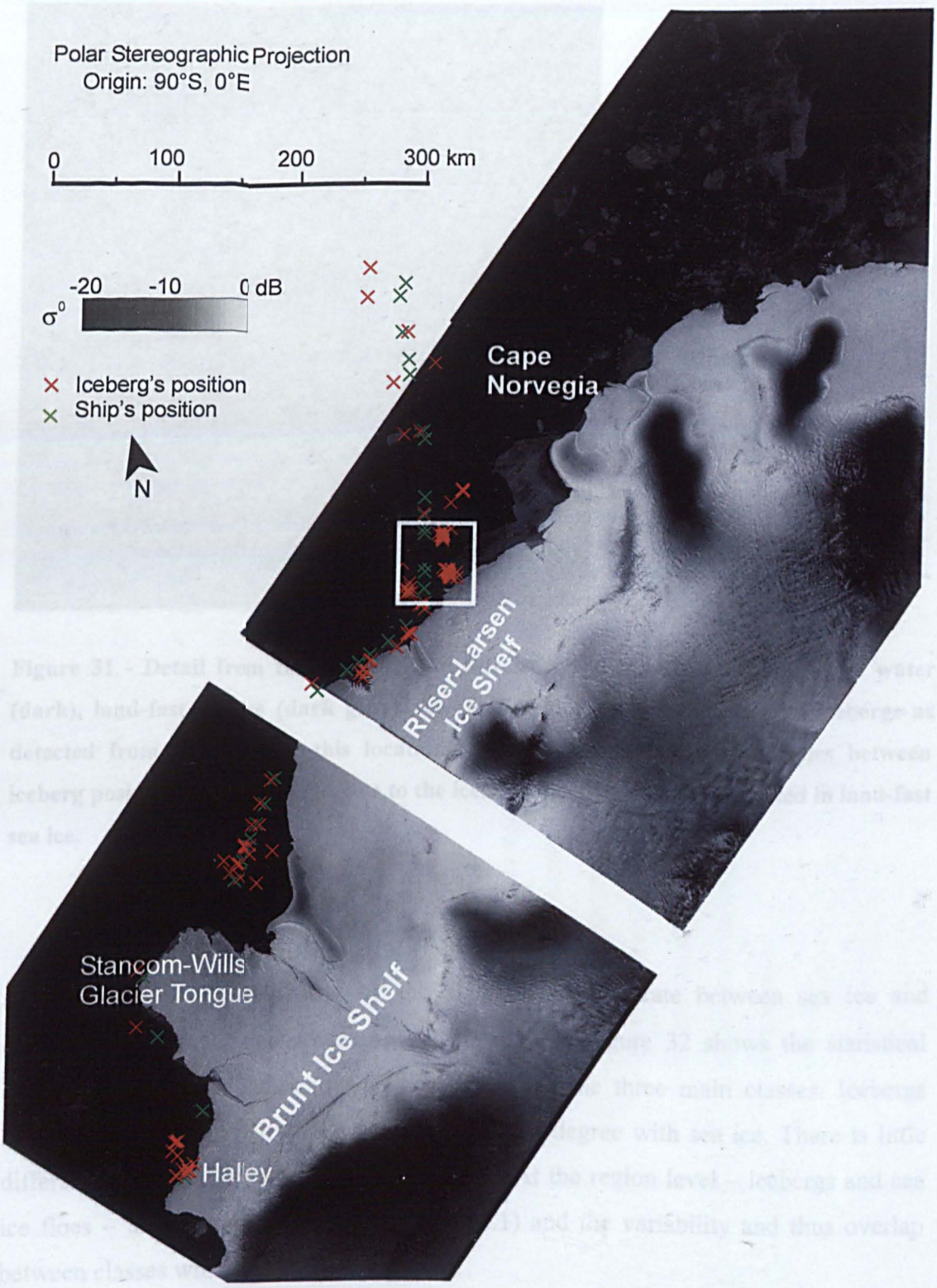

Figure 30 - SAR images of the Eastern Coast of the Weddell Sea with the location of the surveyed icebergs and ship's position. The area within the white rectangle is shown in detail on Figure 30.

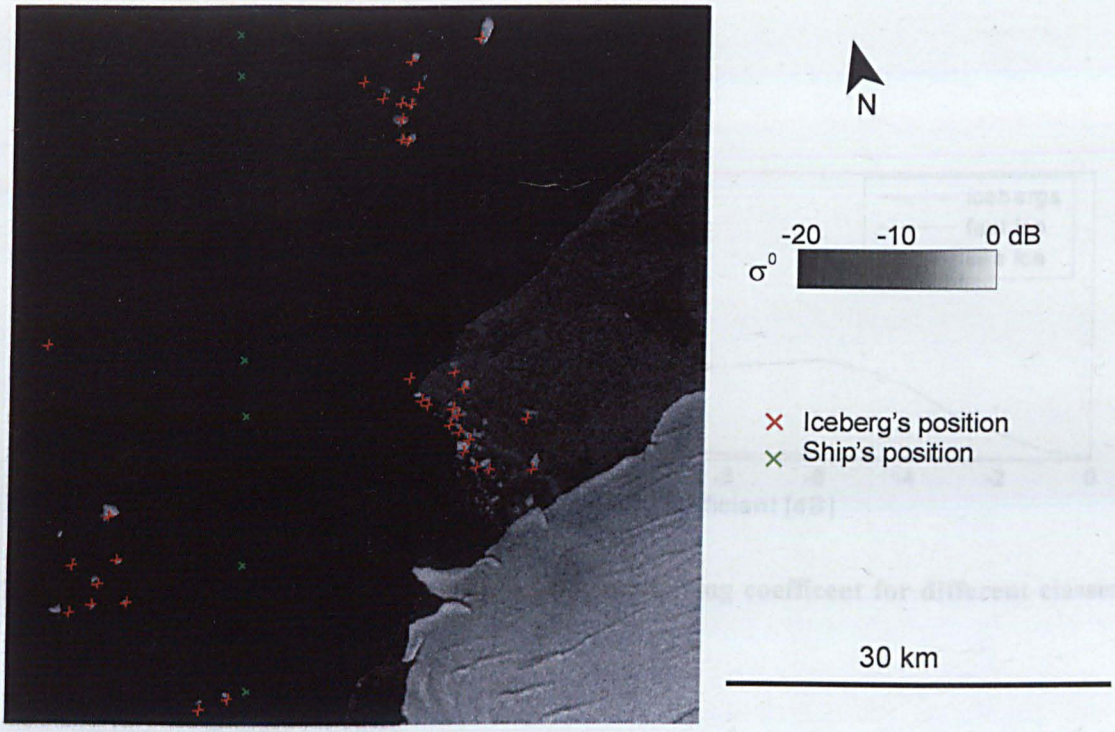

Figure 31 - Detail from the coast off the Riisen-Larsen Ice Shelf showing open water (dark), land-fast sea ice (dark gray), ice shelf (white) and the position of icebergs as detected from the ship. In this location there were very few discrepancies between iceberg positions and the image, due to the icebergs being grounded or locked in land-fast sea ice.

The main parameter used by the algorithm to separate between sea ice and icebergs is the radar backscattering coefficient, σ^0. Figure 32 shows the statistical distribution of pixel backscattering coefficient for the three main classes. Icebergs show the larger variability, overlapping to a large degree with sea ice. There is little difference between loose and land-fast sea ice. At the region level – icebergs and sea ice floes – the average is calculated as in (2.1) and the variability and thus overlap between classes will be smaller (Figure 33).

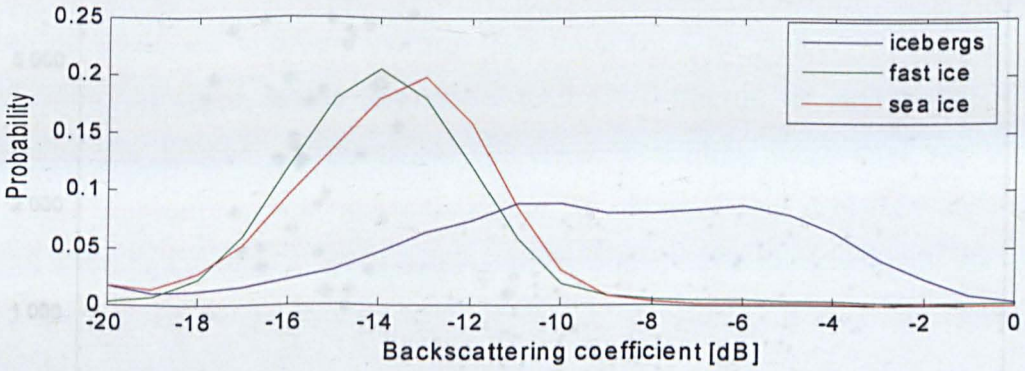

Figure 32 - Statistical distribution of pixel backscattering coefficent for different classes of floating ice.

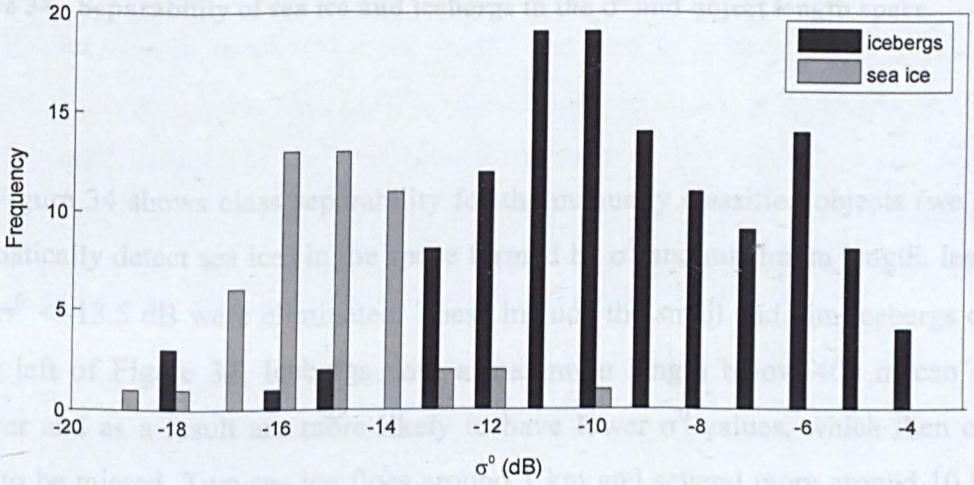

Figure 33 - Statistical distribution of region backscattering coefficient for sea ice and icebergs.

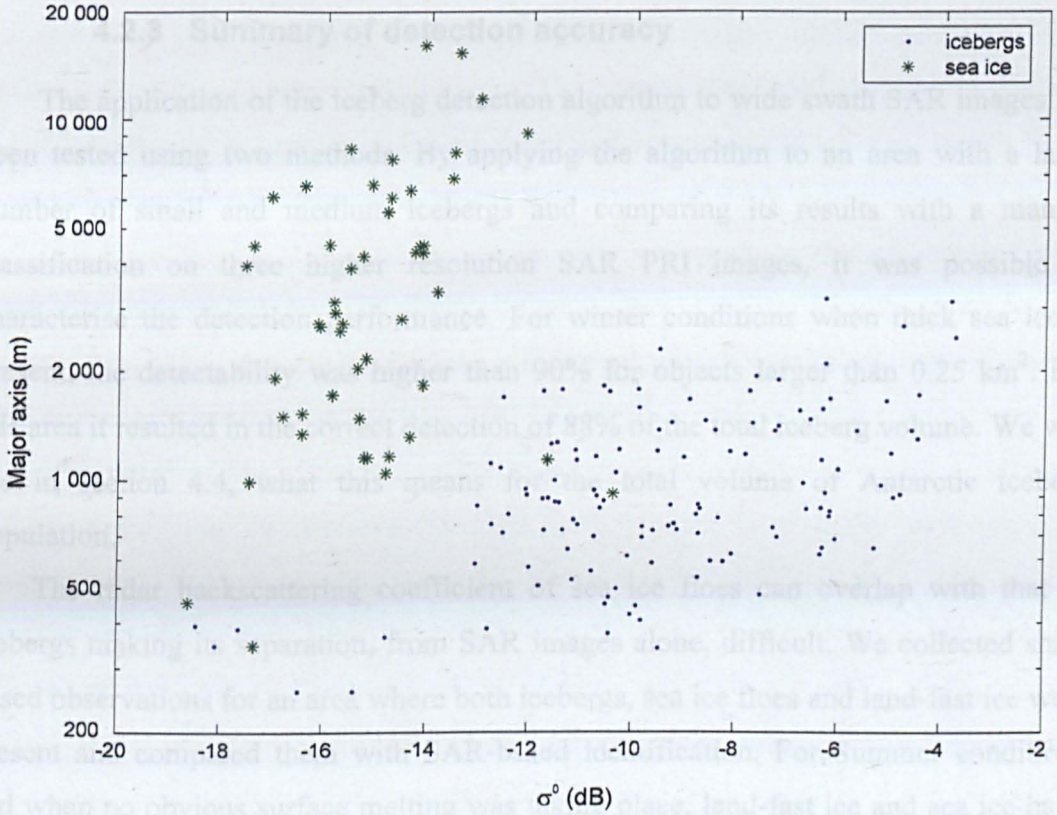

Figure 34 - Separability of sea ice and icebergs in the σ^0 and object length space.

Figure 34 shows class separability for the manually classified objects (we didn't automatically detect sea ice) in the space formed by σ^0 and maximum length. Icebergs with $\sigma^0 < -13.5$ dB were eliminated. These include the small and dim icebergs on the lower left of Figure 34. Icebergs with a maximum length below 400 m can suffer rollover and as a result are more likely to have lower σ^0 values, which then causes them to be missed. Two sea ice floes around 1 km and several more around 10 km in length are above the σ^0 threshold and hence result in false alarms. While the very large ice floes are easy to eliminate visually due to a rounded shape, but 1 km long floes might lead to confusion. In this dataset all the 3 ice floes initially classified as iceberg were correctly eliminated visually.

4.2.3 Summary of detection accuracy

The application of the iceberg detection algorithm to wide swath SAR images has been tested using two methods. By applying the algorithm to an area with a large number of small and medium icebergs and comparing its results with a manual classification on three higher resolution SAR PRI images, it was possible to characterise the detection performance. For winter conditions when thick sea ice is present, the detectability was higher than 90% for objects larger than 0.25 km^2. For this area it resulted in the correct detection of 88% of the total iceberg volume. We will see in section 4.4, what this means for the total volume of Antarctic iceberg population.

The radar backscattering coefficient of sea ice floes can overlap with that of icebergs making its separation, from SAR images alone, difficult. We collected ship-based observations for an area where both icebergs, sea ice floes and land-fast ice were present and compared them with SAR-based identification. For Summer conditions and when no obvious surface melting was taking place, land-fast ice and sea ice have similar σ^0 values that overlap with the σ^0 values of dimmer icebergs. The icebergs missed were mostly small and more eroded that tend to have lower σ^0 values. This resulted in successful detection of 97% of the iceberg volume on the validation dataset. For the small number of icebergs samples relative to the population size, and the specific summer and sea ice conditions observed here, the sea ice floes did not present a significant classification problem. Despite the ship-based validation, this experiment relies on WS images, and unlike the previous experiment, it does not include the errors created by small icebergs only detected by PRI images.

4.3 Iceberg distribution in the coastal Southern Ocean

The Canadian Space Agency and NASA produced a high resolution mosaic of Antarctica using RADARSAT SAR. The RADARSAT-1 Antarctic Mapping Project (RAMP) mosaic includes images from September and October 1997 at a resolution of 25 m. The main aim of RAMP was to create a map of the continent to be used in glaciological and geological studies, and as a baseline for future mosaics. It also covers a strip around the whole coast which we used for studying the spatial distribution of

icebergs. We used the version with resolution reduced to 125 m which is freely available from http://nsidc.org/daac/ramp/. The coastal strip is on average 235 km wide but it is particularly narrow in the southern and western Weddell Sea, which is the most important area for advection of icebergs further north. We completed this gap in the data by obtaining a second set of 16 WS SAR images (image details in the Appendix) covering the coastal Weddell Sea (Figure 35). The images were acquired between 26/8/2004 and 10/10/2004, so although it wasn't possible to acquire images for 1997 as in RAMP, we made sure that the second mosaic covered the same season. The parameters of the extra images are listed in the Appendix. It wasn't possible to obtain coverage of the northern Weddell as the sensor is normally switched from image mode to the low data rate wave mode once it is over open ocean.

The RAMP mosaic was partitioned into 20 smaller images along the coast to reduce the memory requirements of the iceberg detection algorithm. False alarms, mostly caused by bright multi-year sea ice, were excluded manually. The total number of icebergs and ice volume are presented on Table 10.

Table 10 - Summary of results from iceberg detection on SAR mosaics.

	Area (km^2)	Number of iceberg		Estimated ice volume (m^3)	
		< 100 km^2	All	<100 km^2	All
RAMP mosaic	2.957×10^{10}	25 993	26 009	2.97×10^{12}	6.20×10^{12}
Weddell Sea mosaic	1.336×10^{10}	7873	7 886	6.14×10^{11}	2.91×10^{12}

The total ice volume on the RAMP mosaic is almost three times the annual calving flux on the Antarctic Ice Sheet of $2072\pm304\times10^{12}$ kg a^{-1} [*IPCC*, 2001] despite the area constituting only 2.957×10^{6} km^2 or 15% of the area of the Southern Ocean. The Weddell Sea mosaic had even higher ice concentrations than the RAMP mosaic for the same areas, with very high concentrations of small icebergs on the Western Weddell and South-eastern Weddell (see Figure 35 and Figure 36). It is clear that in the Weddell Sea the ice flux is no longer confined to the coast and there might be an important part of it that is not sampled in the Weddell mosaic. The mass distribution around the coast is very patchy due to several factors, one of which is that areas with low bathymetry close to calving glaciers can become important iceberg traps. One such

example is the area around Land Glacier, in the Ruppert Coast, West Antarctica (~140°W) studied in section 4.2.1. Another factor is the presence of giant icebergs such as next to the Shackleton Ice Shelf (~100°E) in East Antarctica.

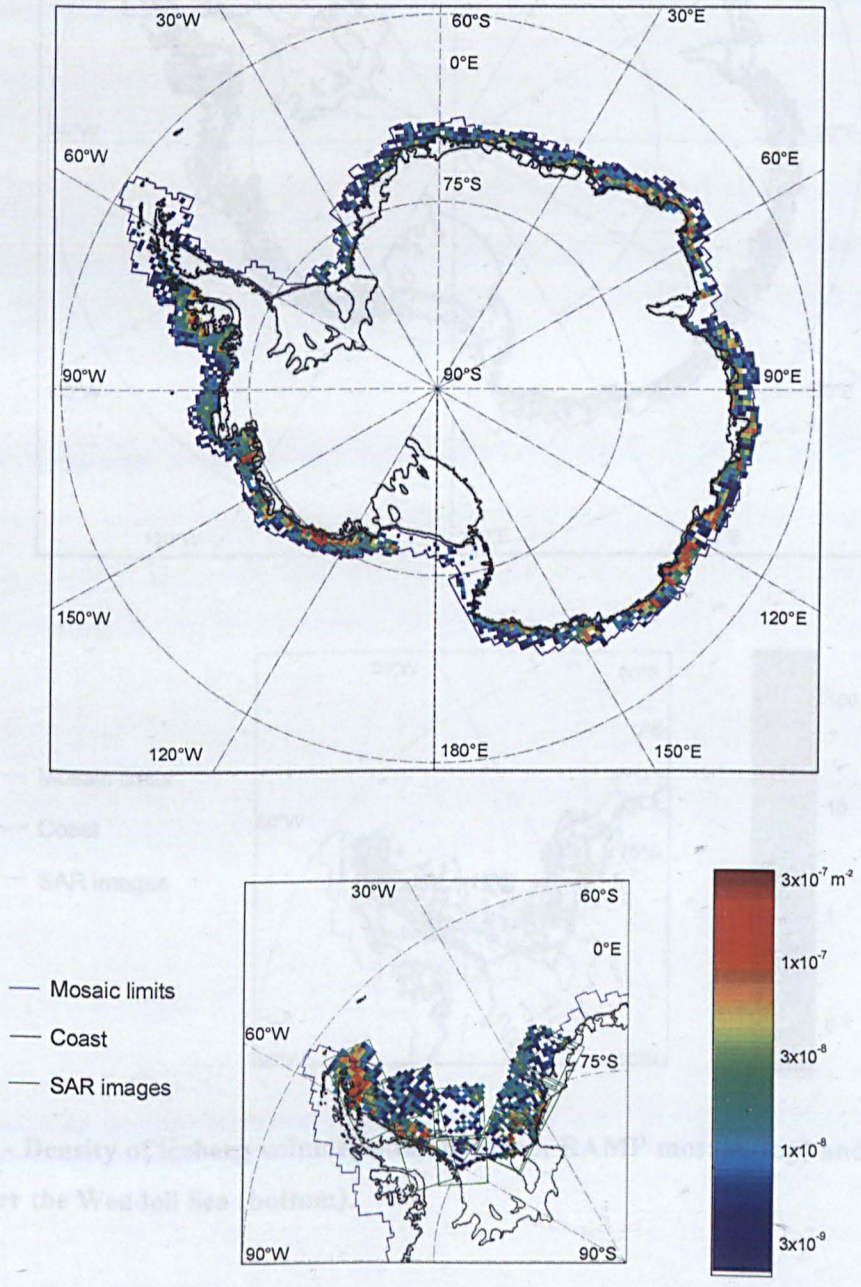

Figure 35 - Iceberg density estimated from RAMP mosaic (top) and from WS images over the Weddell Sea (bottom).

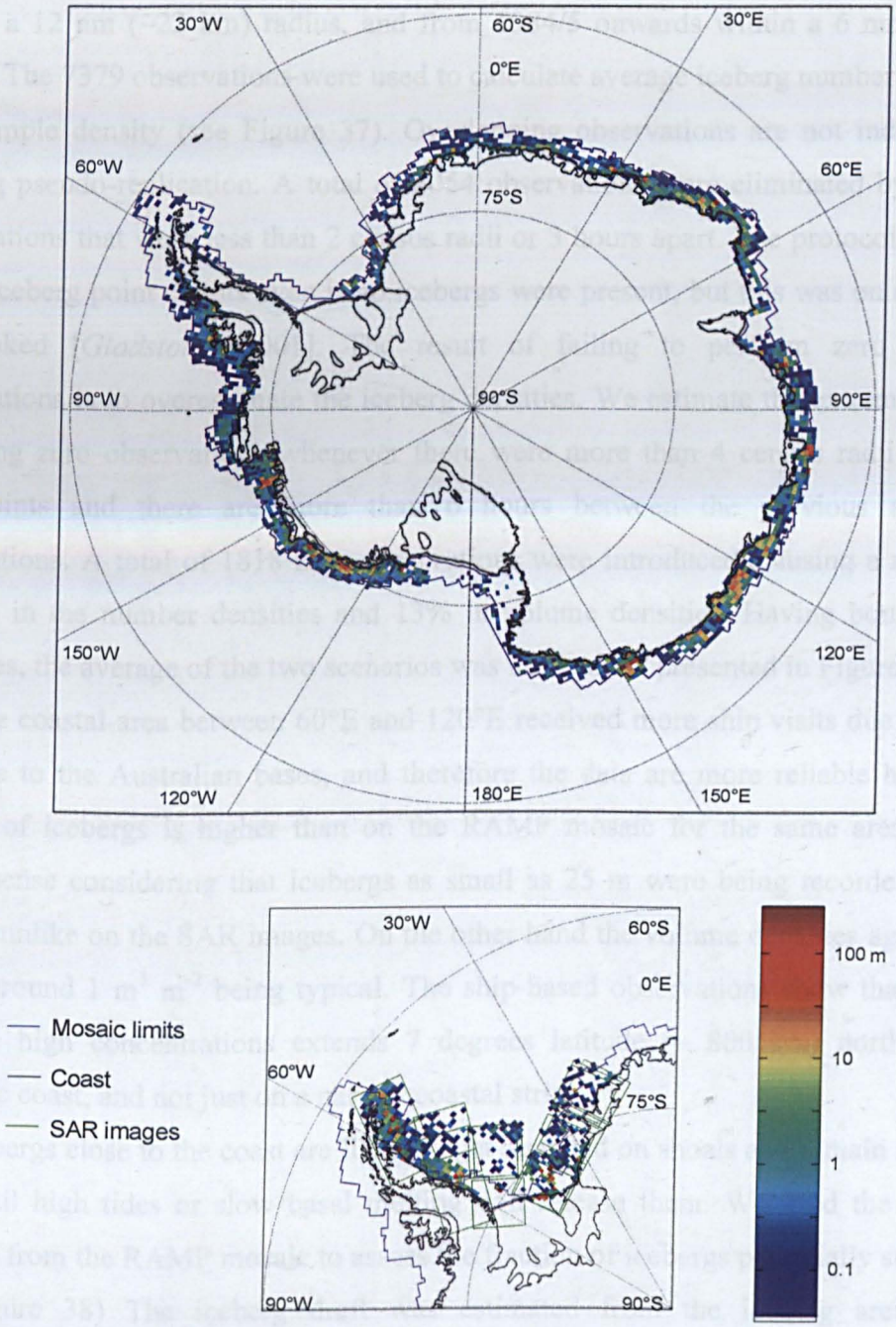

Figure 36 - Density of iceberg volume estimated from RAMP mosaic (top) and from WS images over the Weddell Sea (bottom).

These estimates can be compared with densities extracted from Australian ship-based observations. The Australian Antarctic Division, former ANARE, collected ship-based observations on Antarctic cruises from 1978/9 to 2000/1 which are maintained by Jo Jacka. The density of icebergs in several size categories was recorded

within a 12 nm (~22 km) radius, and from 1984/5 onwards within a 6 nm (11 km) radius. The 7379 observations were used to calculate average iceberg number and mass and sample density (see Figure 37). Overlapping observations are not independent, causing pseudo-replication. A total of 2054 observations were eliminated by purging observations that were less than 2 census radii or 3 hours apart. The protocol involved doing iceberg point counts even if no icebergs were present, but this was on occasions overlooked [*Gladstone*, 2001]. The result of failing to perform zero icebergs observations is to overestimate the iceberg densities. We estimate the extreme case of including zero observations whenever there were more than 4 census radii between two points and there are more than 6 hours between the previous and next observations. A total of 1818 zero observations were introduced, causing a reduction of 15% in the number densities and 13% in volume densities. Having bounded the estimates, the average of the two scenarios was used and is presented in Figure 37.

The coastal area between 60°E and 120°E received more ship visits due to being *en route* to the Australian bases, and therefore the data are more reliable here. The density of icebergs is higher than on the RAMP mosaic for the same area, which makes sense considering that icebergs as small as 25 m were being recorded on the cruises, unlike on the SAR images. On the other hand the volume densities agree with values around 1 m^3 m^{-2} being typical. The ship-based observations show that in this area the high concentrations extends 7 degrees latitude (~ 800 km) north of the Antarctic coast, and not just on a narrow coastal strip.

Icebergs close to the coast are likely to get stranded on shoals and remain there, at least until high tides or slow basal melting will release them. We used the iceberg database from the RAMP mosaic to assess the fraction of icebergs potentially stranded. (see Figure 38) The iceberg draft was estimated from the iceberg area using expression (4.1) for the thickness and multiplying this by the ratio of the densities of ice and water, 0.85. The bathymetry data were the 2-minute Gridded Global Relief Data, ETOPO2, from the National Oceanic and Atmospheric Administration, available from http://www.ngdc.noaa.gov/mgg/fliers/01mgg04.html. The ETOPO2 data were derived from satellite observations of gravity anomaly and microwave altimetry combined with selected shipboard echo-sounding measurements.

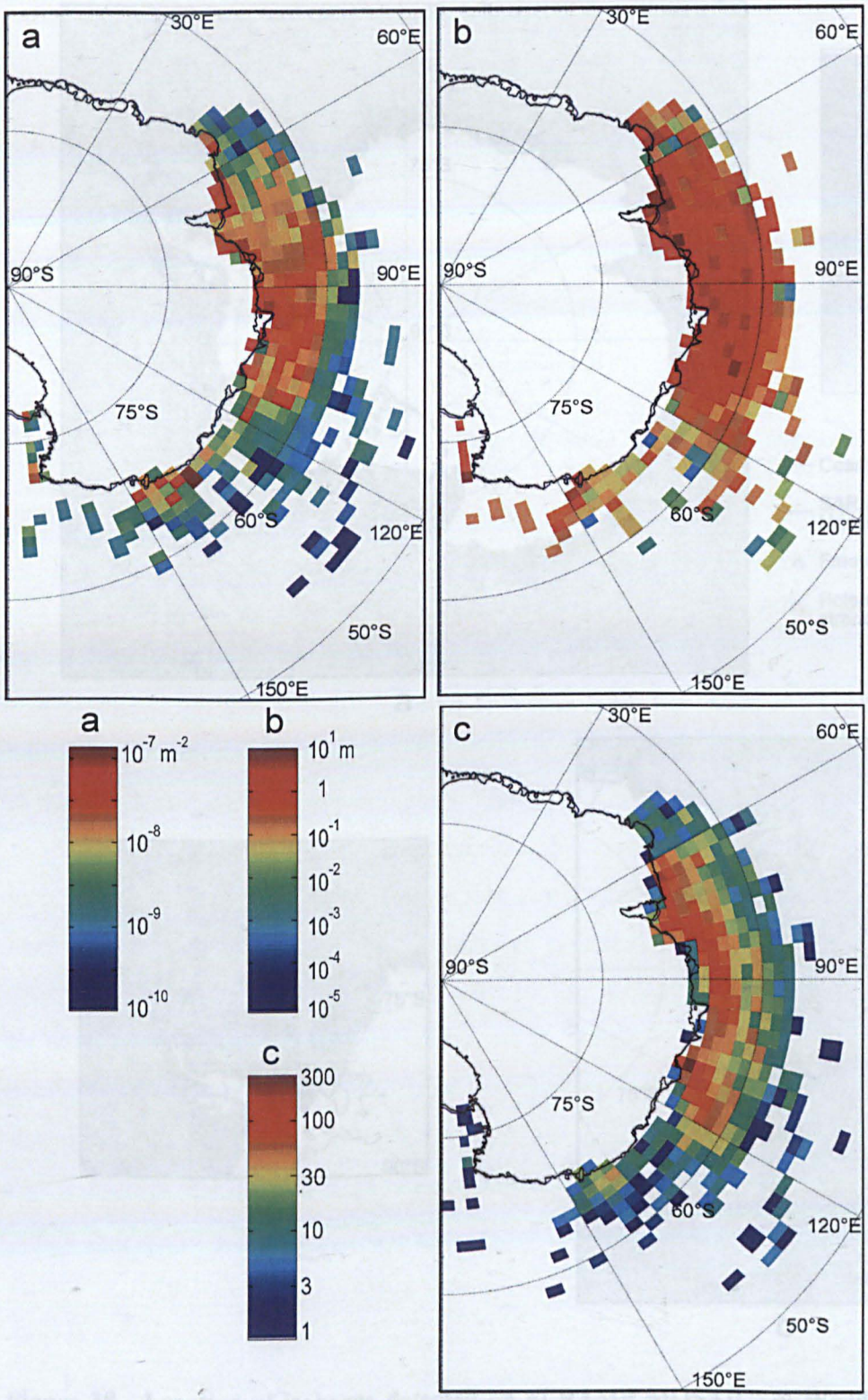

Figure 37 – Summary of Australian ship-based iceberg observations from 1978/9 to 2000/1 calculated for a 1°×3° grid: a) Iceberg density b) Iceberg volume density and c) Number of samples per grid cell. The data were corrected for pseudo-replication and missed zero observations (see text for details).

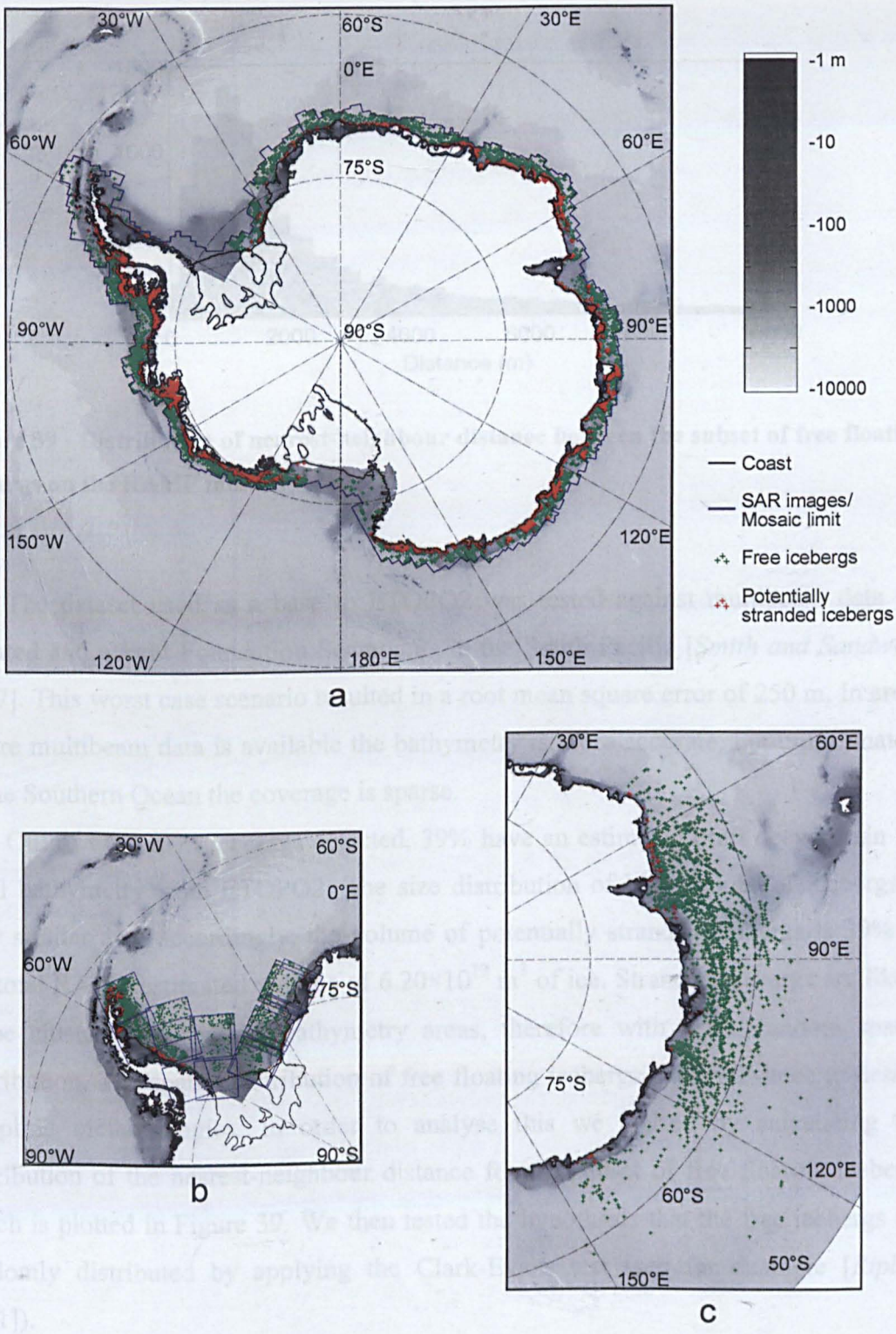

Figure 38 - Location of icebergs detected on a) RAMP MOSAIC, b) Weddell Sea SAR images and c) ANARE ship-based observations, overlayed on the ocean bathymetry from ETOPO2 data. Icebergs with an estimated draft larger than the local bathymetry are indicated as as potentially stranded.

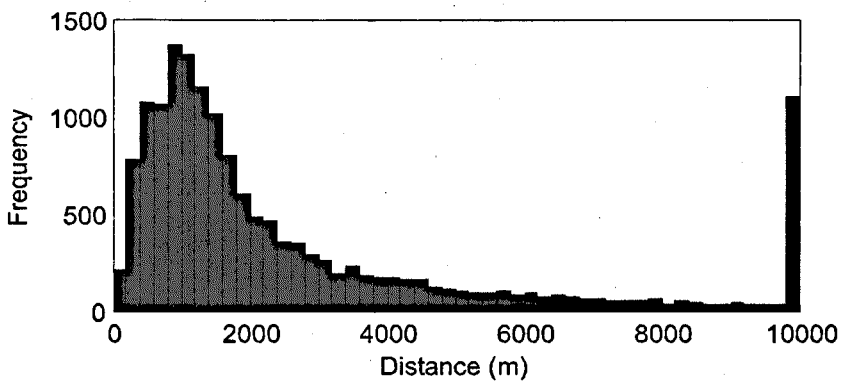

Figure 39 - Distribution of nearest-neighbour distance between the subset of free floating icebergs on the RAMP mosaic.

The dataset used as a base to ETOPO2 was tested against multibeam data for isolated and abrupt Foundation Seamounts in the South Pacific [*Smith and Sandwell*, 1997]. This worst case scenario resulted in a root mean square error of 250 m. In areas where multibeam data is available the bathymetry is more accurate, but unfortunately in the Southern Ocean the coverage is sparse.

Out of the 26673 icebergs detected, 39% have an estimated draft deeper than the local bathymetry from ETOPO2. The size distribution of both groups of icebergs is very similar and, accordingly, the volume of potentially stranded icebergs is 39% of the total RAMP estimated volume of 6.20×10^{12} m^3 of ice. Stranded icebergs are likely to be clustered in shallow bathymetry areas, therefore with a non-random spatial distribution. The spatial distribution of free floating icebergs is of relevance to design sampling methodologies. In order to analyse this we started by calculating the distribution of the nearest-neighbour distance for the subset of free floating icebergs which is plotted in Figure 39. We then tested the hypothesis that the free icebergs are randomly distributed by applying the Clark-Evans test (see for example [*Ripley*, 1981]).

Random distributed icebergs would have a Rayleigh distributed nearest-neighbour distance, but it follows from the *Central Limit Theorem* that independent sums of identically distributed random variables are approximately normally distributed[1]. This

[1] This applies for number of samples $m \geq 30$ as long as the distribution is not too skewed.

applies to the sample mean of the nearest-neighbour distance, $\hat{d} = \frac{1}{m}\sum_{i=1}^{m} d_i$, where m is the number of samples and d_i the measured nearest-neighbour distance i. The Clark-Evans test consist in testing if $\hat{d} \sim N(\mu_d, \sigma_d^2)$. The parameters are:

$$\mu_d = \frac{1}{2\sqrt{D}} \tag{4.2}$$

$$\sigma_d^2 = \frac{4-\pi}{m4D\pi} \tag{4.3}$$

and D is the average iceberg density. In order to be able to use standard normal tables the standardized sample mean is calculated

$$z = \frac{\hat{d} - \mu_d}{\sigma_d}. \tag{4.4}$$

and a two-tailed test for the hypothesis that z follows a Gaussian distribution, $N(0, 1)$, was calculated. Significant small values of $\hat{d}$ indicate clustering while significant large values indicate a regular distribution. From Table 10 the iceberg density in the RAMP mosaic is $D = 5.53\times10^{-3}$ km^2 and (4.2) and (4.3) result in $\mu_d = 6727$ m and $\sigma_d = 27.51$ m. For the free floating icebergs in the RAMP mosaic we observed the sample mean of the nearest-neighbour $\hat{d} = 3278$ m showing that the icebergs are highly clustered ($z = -125.4$, $p < 0.001$)[2].

A previous study had also found a high clustering in icebergs around East Antarctica [*Young et al.*, 1998]. There are several likely root causes for this pattern: i) the confluence of the forcing fields, the most important in the RAMP mosaic area being the narrow coastal current; ii) the effect of dense sea ice in binding and moving icebergs together as shown by Schodlok *et al.* [2006], iii) as a result of the break-up process calved icebergs will move along with the parent iceberg until they eventually diverge and iv) a synchronised release of icebergs, during calving or after being grounded for instance by storms or higher than average tides. The clustered

[2] One of the limitation of applying the Clark-Evans test, is the Central Limit Theorem assumption for independency that requires the subsampling of the data not to include duplicated distances between pairs or objects. Also it doesn't take into account edge effects and because the nearest neighbour is first-order statistic, only uses part of the information available. Still, this test was selected due to its simplicity and because the clustering is so pronounced the conclusions are robust.

distribution will command more intensive sampling for a monitoring scheme for icebergs, as discussed in section 4.7.

4.4 Size Distribution and Decaying Mechanisms

The iceberg size distribution for both mosaics was calculated and compared with the ANARE and the National Ice Centre giant icebergs' datasets. A combined mosaic was also created by using the Weddell Mosaic and outside its coverage, the RAMP mosaic. Three size distribution and total ice volume per size class for the RAMP, Weddell and combined dataset is presented in Figure 40. Two size modes in the iceberg size distribution account for most of the ice volume in both the mosaics (see right column in Figure 40): area classes around 10^6 and above 10^9 m^2; that is to say kilometric and multi-decakilometric icebergs. The cumulative distribution shows that each of these broad classes is responsible for around 30% of the floating ice mass in the coastal strip and Weddell Sea.

On the Australian ship-based observations larger icebergs were often grouped into the largest category – larger than 3200 m – without the size being recorded. Therefore the size distribution shows the predominance in volume and numbers of the kilometre long icebergs but underestimates the importance of very large icebergs (Figure 41).

The National Ice Center tracks icebergs larger than 18 km using satellite remote sensing. In Figure 42 we show the size distribution using the data from 1979 to 2004. Although the class of 500 km^2 is more frequent the 5000 km^2 class is the most important in terms of ice volume.

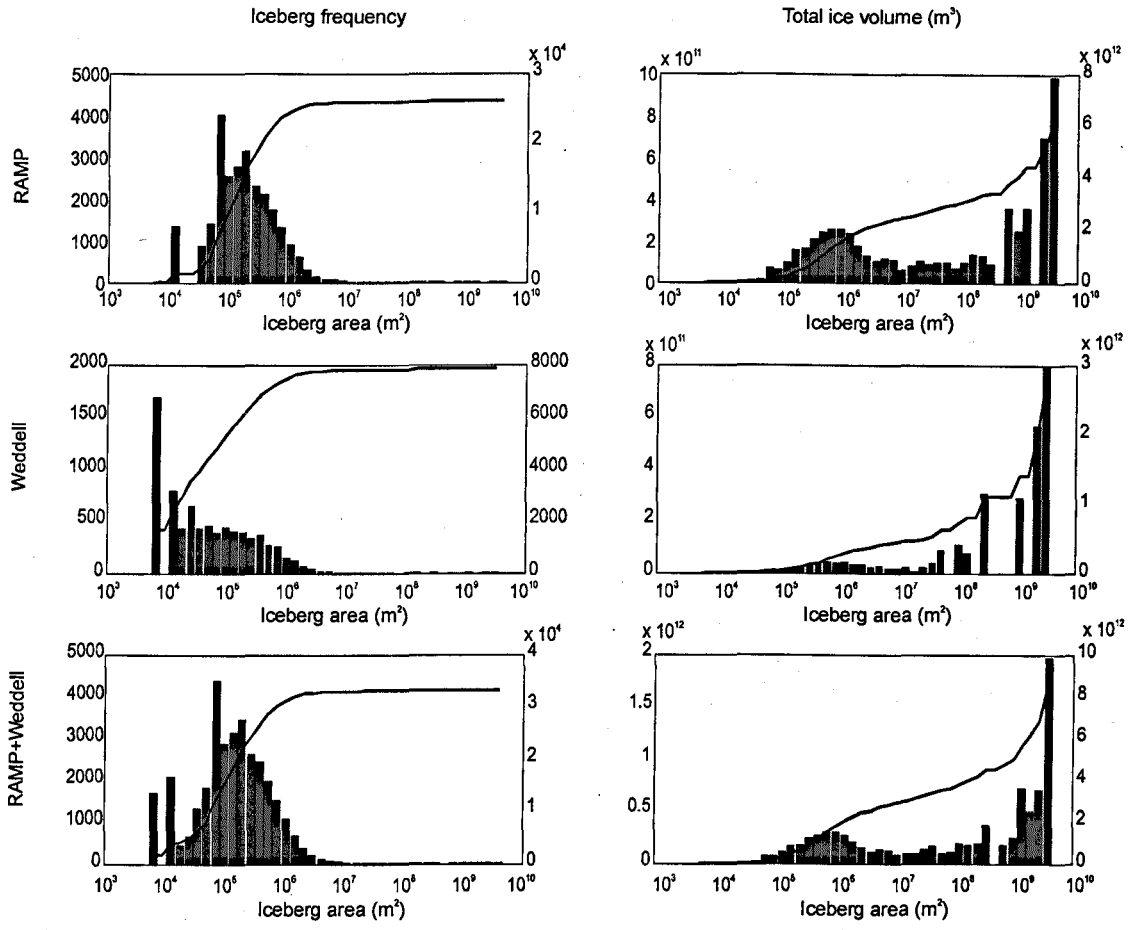

Figure 40 - Iceberg frequency and total ice volume per area class from three datasets: RAMP mosaic from 1997 (top); Weddell mosaic from 2004 (middle) and the combination of both mosaics (bottom). The dark line represents the cumulative distribution for both frequency and ice volume.

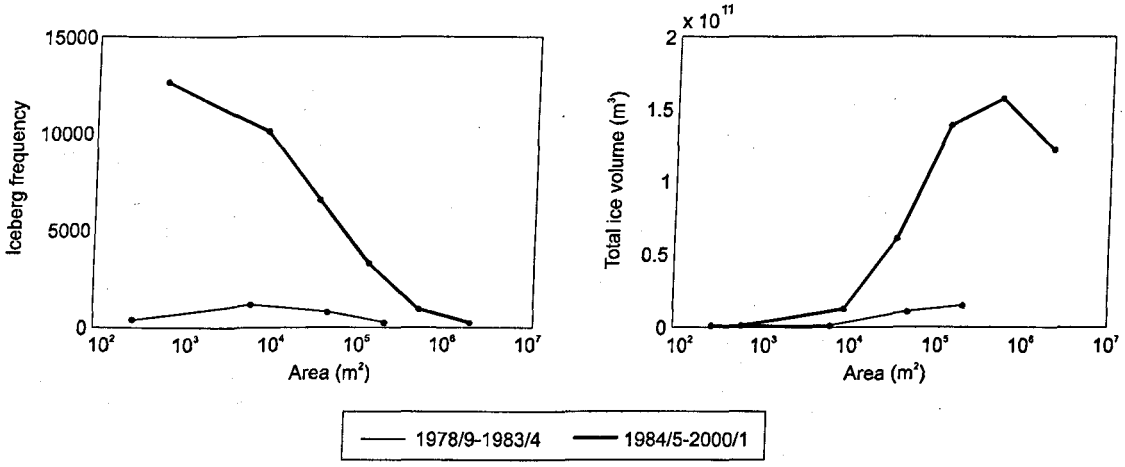

Figure 41 - Iceberg frequency and total ice volume per area class for ANARE ship-based observations. The period 1978/9-1983/4 and 1984/85-2000/1 were treated differently due to a change in the size classes used.

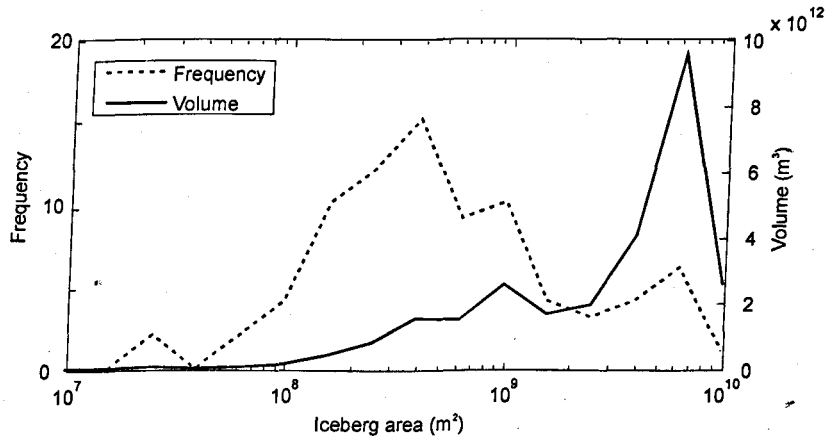

Figure 42 - Size distribution and equivalent volume of Giant icebergs calved between 1979 and 2003. Data from the National Ice Center giant iceberg database.

The effect of the partial detectability of the detection algorithm can be be assessed by correcting the observations using the detectability curve in Figure 28. By dividing the number of observed icebergs by the interpolated detectability values, corrected iceberg volumes can be estimated for the RAMP mosaic. For the population of icebergs of up to 100 km^2, 9.0 % of the iceberg volume is missed. Including all the

icebergs, the missed volume is only 3.8 %. It is more difficult to assess the volume of icebergs too small to be detected at all on the RAMP and Weddell Sea mosaics. If we assumed that in the ship-based ANARE observations (Figure 41) all icebergs down to 25 m were detected and calculated the volume for icebergs below 0.1 km^2 to be 2%. This iceberg size has a detectability value for WS images of 75% (Figure 28) so certainly less than 2% of the iceberg volume would be completely missed.

We expect to see in the calving process the same bimodal distribution as in the total population of icebergs. The stress fields on glaciers will produce regular crevassing and as a result small icebergs, while the large, more homogenous, ice-shelves will produce the very large tabular icebergs. We did not determine the calving size distribution from observations as this would require monitoring the calving front with long time-series of SAR images. As an indication, the size distribution of the icebergs around the Land Glacier used in section 4.2.1, that we assume that have not suffered much erosion since calving, shows the same dominance of kilometre sized icebergs (see Figure 27).

The size distribution of the population of icebergs will differ from the calving size distribution due to the erosion processes affecting icebergs. We now use a simple model for the size characteristics of a population of icebergs to test the importance of different erosion processes in the resulting size distribution. Both melting of submerged walls and break-up into smaller icebergs is included.

The model is a function of two discrete variables, time t and iceberg size class i. The area classes, $A(i)$, are defined so that by melting and break-up the ice volume in category i at time t migrates to the smaller category $i-1$ at time $t+1$. Thus

$$A(i) = \frac{A(i+1)\,T(i+1)\,M(i+1)}{B\,T(i)} \tag{4.5}$$

where $M(i)$ is the proportion of melted volume, $T(i)$ the iceberg thickness given by equation (4.1) and B the break-up factor or the number of icebergs originated from one iceberg in one time step Δt. As we assume that break-up and side melting is faster than basal melting, in equation (4.5) we use $T(i) \approx T(i+1)$. The volume of ice in each size class is defined as follows:

$$V(i,t) = V(i+1,t-1)M(i+1) + C(i), \tag{4.6}$$

with $C(i)$ being the volume of calving iceberg in size category i over Δt. This time-dependent model is run until the steady state has been attained, which typically takes

10 to 100 iterations. The proportion of nonmelted volume is defined as $M(i) = V(i-1)/V(i)$. Considering that the submerged surface of the icebergs – on the lower 5/6 of its total thickness – melts at a constant rate of k, in m per time interval Δt, and taking a parallelepipedic iceberg with dimensions $L \times 2/3\ L \times T$ and horizontal area A, results in the following expression for the proportion of non-melted or retained volume:

$$M(i,t) = 1 - \left(\frac{1}{T(i)} + \frac{25}{\sqrt{54}} A(i)^{-\frac{1}{2}} \right) k \tag{4.7}$$

The calving size distribution was modelled by a mixture of two lognormal distribution functions representing glacier calved icebergs and giant icebergs, respectively:

$$C(A) = \left(\aleph(A,14,1) + \aleph(A,30,2.5) \times 10^7 \right) K_N \tag{4.8}$$

with $\aleph(x,\mu,\sigma)$ being the lognormal function of x with mean μ and log standard deviation σ; and K_N a scaling constant so that $\int C(A)dA = 2 \times 10^{12}$ which is roughly the annual calving rate for Antarctica. Figure 43 shows the synthetic calving size distribution and the observed size distribution from RAMP.

The reduction in iceberg size accelerates for smaller icebergs due to the higher surface area-volume ratio. The M function for a constant melting of the submerged surfaces (equation (4.7)) is plotted in Figure 44. The iceberg model used by Gladstone [2001] and Gladstone *et al.* [2001] included melting of the bottom due to turbulent flow, buoyancy driven side melting and wave erosion but break-up was not included. The melting terms were driven by ocean, sea ice and atmospheric fields. We extracted the function M for every three days from a simulation output for the whole Southern Ocean and this shows a much larger variability but the same basic pattern as our simple approximation (Figure 44).

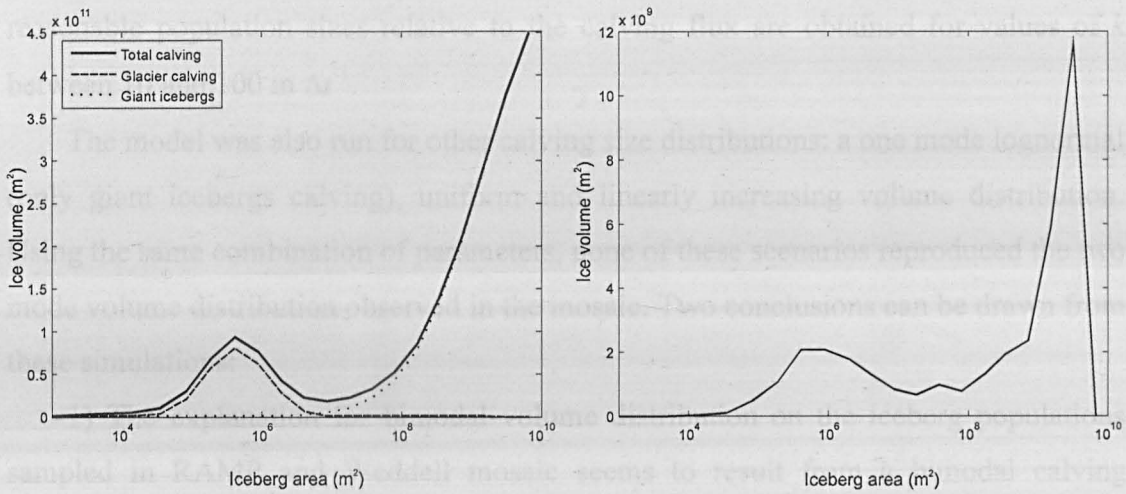

Figure 43- Iceberg size distributions: (left) calving distribution generated as a mixture of two lognormal distribution functions and (right) observed distribution on RAMP mosaic.

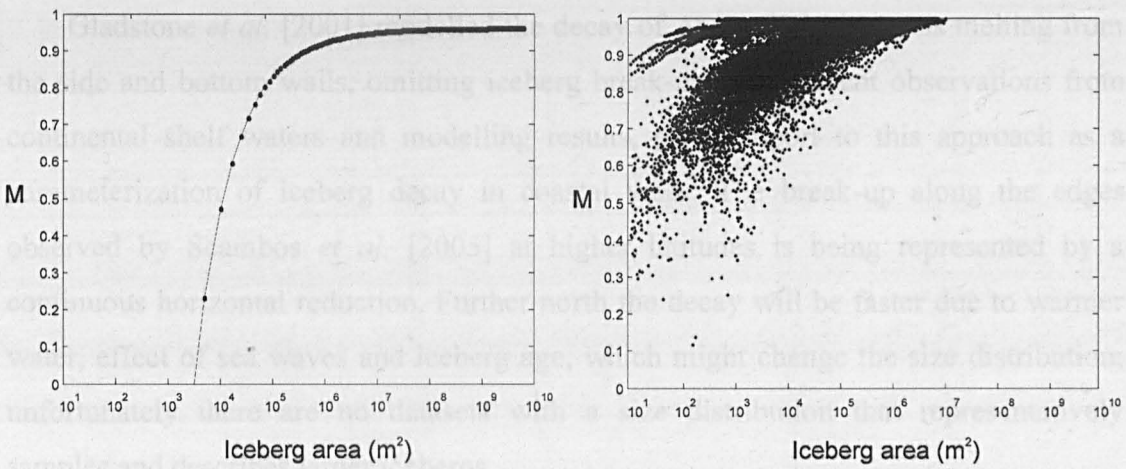

Figure 44 - Proportion of non-melted volume, M, for: (left) present model and (right) extracted from Gladstone [2001] model run.

Taking the bimodal calving size density from (4.8) the model was run with and without break-up and for three different melting rates, k. The resulting distribution of ice volume per size class, V(i), is shown in Figure 45. The melting functions that better reproduce the bimodal calving distribution observed on RAMP and Weddell mosaics are when no break-up is present (B=1). In this situation and with slow melting, $k = 1$ m Δt^{-1}, results in a very long iceberg longevity and a huge population of icebergs. More

reasonable population sizes relative to the calving flux are obtained for values of k between 10 and 100 m Δt^{-1}.

The model was also run for other calving size distributions: a one mode lognormal (only giant icebergs calving), uniform and linearly increasing volume distribution. Using the same combination of parameters, none of these scenarios reproduced the two mode volume distribution observed in the mosaic. Two conclusions can be drawn from these simulations:

1) The explanation for bimodal volume distribution on the iceberg populations sampled in RAMP and Weddell mosaic seems to result from a bimodal calving distribution, probably icebergs originating in glaciers and ice shelves. Simple physical models of erosion and break-up were not capable or reproducing the second mode.

2) The melting function, proportional to the submerged surface area, was able to replicate the observations better than when combined with a break-up process into N identical offspring.

Gladstone *et al.* [2001] modelled the decay of Antarctic icebergs as melting from the side and bottom walls, omitting iceberg break-up. The present observations from continental shelf waters and modelling results, give support to this approach as a parameterization of iceberg decay in coastal areas. The break-up along the edges observed by Scambos *et al.* [2005] at higher latitudes is being represented by a continuous horizontal reduction. Further north the decay will be faster due to warmer water, effect of sea waves and iceberg age, which might change the size distribution; unfortunately there are no datasets with a size distribution that representatively samples and describes larger icebergs.

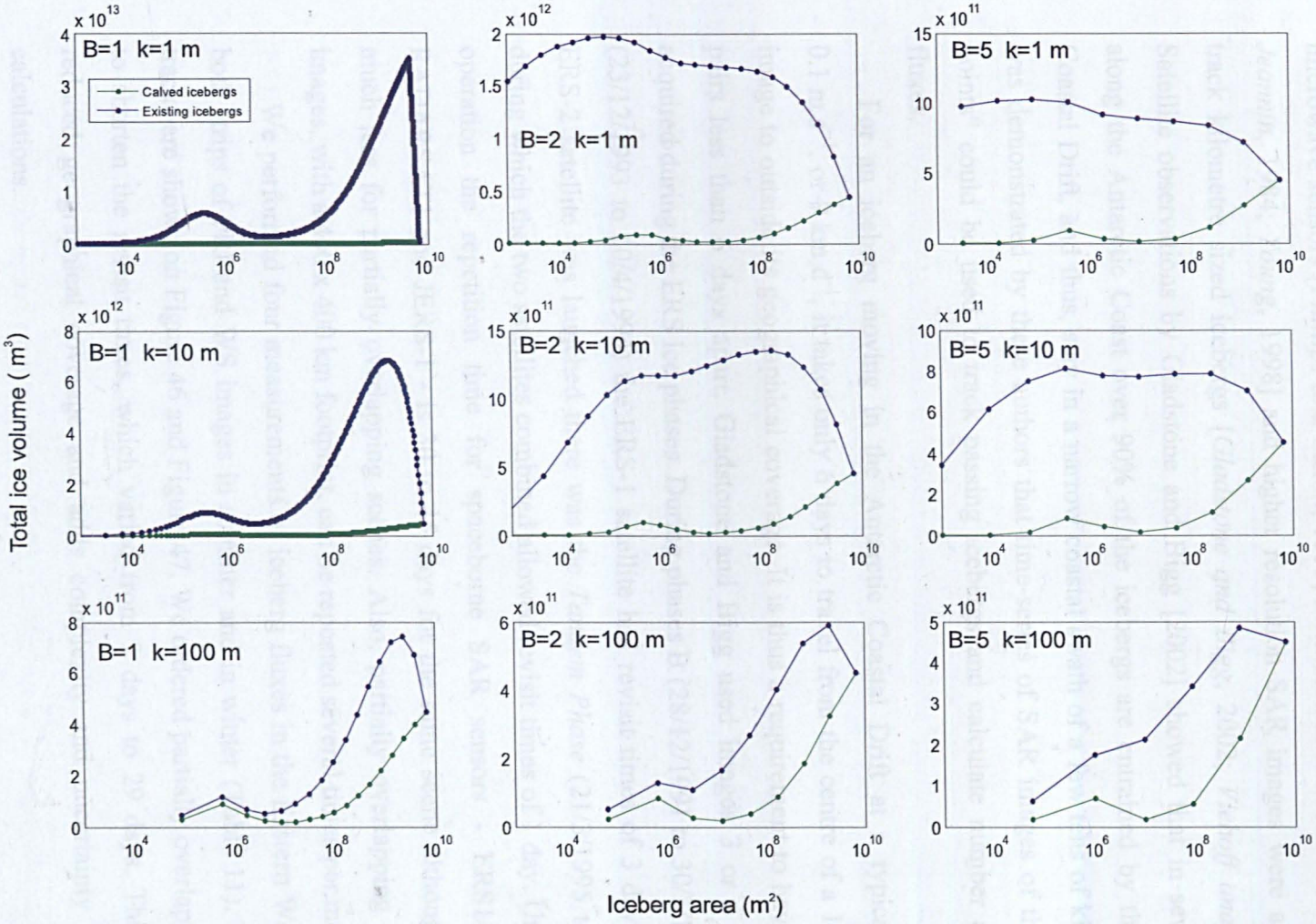

Figure 45 – Modelled iceberg size distributions for different values of break-up (B) and melting rate (k).

4.5 Iceberg Fluxes from SAR images

Giant icebergs have been tracked by satellite using both optical and passive microwave sensors [*Phillips and Laxon*, 1995; *Swithinbank et al.*, 1977; *Tchernia and Jeannin*, 1984; *Young*, 1998] and higher resolution SAR images were also used to track kilometre sized icebergs [*Gladstone and Bigg*, 2002; *Viehoff and Li*, 1995]. Satellite observations by Gladstone and Bigg [2002] showed that in several places along the Antarctic Coast over 90% of the icebergs are entrained by the Antarctic Coastal Drift, and thus, stay in a narrow coastal swath of a few tens of kilometres. It was demonstrated by these authors that time-series of SAR images of these "choke points" could be used to track passing icebergs and calculate number and volume fluxes.

For an iceberg moving in the Antarctic Coastal Drift at a typical speed of 0.1 m s^{-1}, or 9 km d^{-1}, it takes only 6 days to travel from the centre of a 100×100 km image to outside its geographical coverage. It is thus a requirement to have the image pairs less than 6 days apart. Gladstone and Bigg used images 3 or 6 days apart, acquired during the ERS Ice phases. During phases B (28/12/1991 to 30/3/1992) and D (23/12/1993 to 10/4/1994) the ERS-1 satellite had revisit times of 3 days. After the ERS-2 satellite was launched there was the *Tandem Phase* (21/3/1995 to 5/6/1996) during which the two satellites combined allowed revisit times of 1 day. Under normal operation the repetition time for spaceborne SAR sensors - ERS1/2, Envisat, RADARSAT1 and JERS-1 - is 30 to 45 days for the same scene although it can be much less for partially overlapping scenes. Also, partially overlapping wide swath images, with a 400 x 400 km footprint, can be repeated several times per month.

We performed four measurements of iceberg fluxes in the Eastern Weddell using both strips of PRI and WS images in summer and in winter (Table 11). The iceberg tracks are shown on Figure 46 and Figure 47. We ordered partially overlapping images to shorten the revisit times, which varied from 3 days to 29 days. This results in reduced geographical coverage and adds complexity and uncertainty to the flux calculations.

Table 11 - Measurements of iceberg fluxes along the coast using pairs of SAR images. (see Appendix for full image details). Flux measurements with an * were calculated excluding icebergs with more than 100 km^2.

Dataset	PRI_winter_92	WS_summer_03/4	WS_winter_04	WS_summer_04/5
Type of image	ERS-1 PRI	Envisat WS	Envisat WS	Envisat WS
Image dates (UTC time)	8/7/1992 1:24 11/7/1992 1:29 27/7/1992 1:27	26/12/2003 03:04 01/01/2004 03:15	11/09/2004 8:28 10/10/2004 8:18	23/12/2004 07:52 26/12/2004 07:56 05/01/2005 07:41
Num. of icebergs tracked	57	29	101	38
Num. of grounded icebergs	46 (81%)	19 (66%)	56 (55%)	22 (58%)
Average speed of non-grounded icebergs (m s^{-1})	0.053 (3 days) 0.045 (19 days)	0.065 (6 days)	0.041 (29 days)	0.076 (3 days) 0.042 (10 days) 0.040 (13 days)
Iceberg volume density (m3 m^{-2})	0.105	0.443 0.225*	3.95 1.11*	0.132
Iceberg area flux (×10^6 m^2 a^{-1})	63.1 (3 days) 0.03 (16 days) 34.8 (19 days)	216 (6 days) 50.6*	171.4 (29 days) 79.6*	31.3 (3 days) 15.5 (10 days) 15.9 (13 days)
Ice volume flux (×10^9 m^3 a^{-1})	15.8 (3 days) 0.01 (16 days) 8.71 (19 days)	53.9 (6 days) 12.6*	42.8 (29 days) 19.9*	7.83 (3 days) 3.88 (10 days) 3.98 (13 days)

For each image pair, the measured iceberg area flux was calculated as follows,

$$F_A = \sum_{i=1}^{N} \frac{A_i V_i}{D} \tag{4.9}$$

where the sum is performed for each non-grounded iceberg, i, A_i is the surface area and V_i is the along the coast component of the velocity. D is the length of the overlapping image pair that coincides with the coastal flow. In our study D varies from 65 km in PRI_winter_92 study to 1250 km in the mosaic of triple WS images on WS_summer_04. Equivalently, the volume flux is calculated by multiplying A_i by the estimated iceberg thickness, T_i:

$$F_V = \sum_{i=1}^{N} \frac{A_i T_i V_i}{D}. \tag{4.10}$$

where T_i is calculated as a function of the iceberg areas by using the approximation (4.1). The area and volume fluxes for each image or mosaic pair are presented in Table 11.

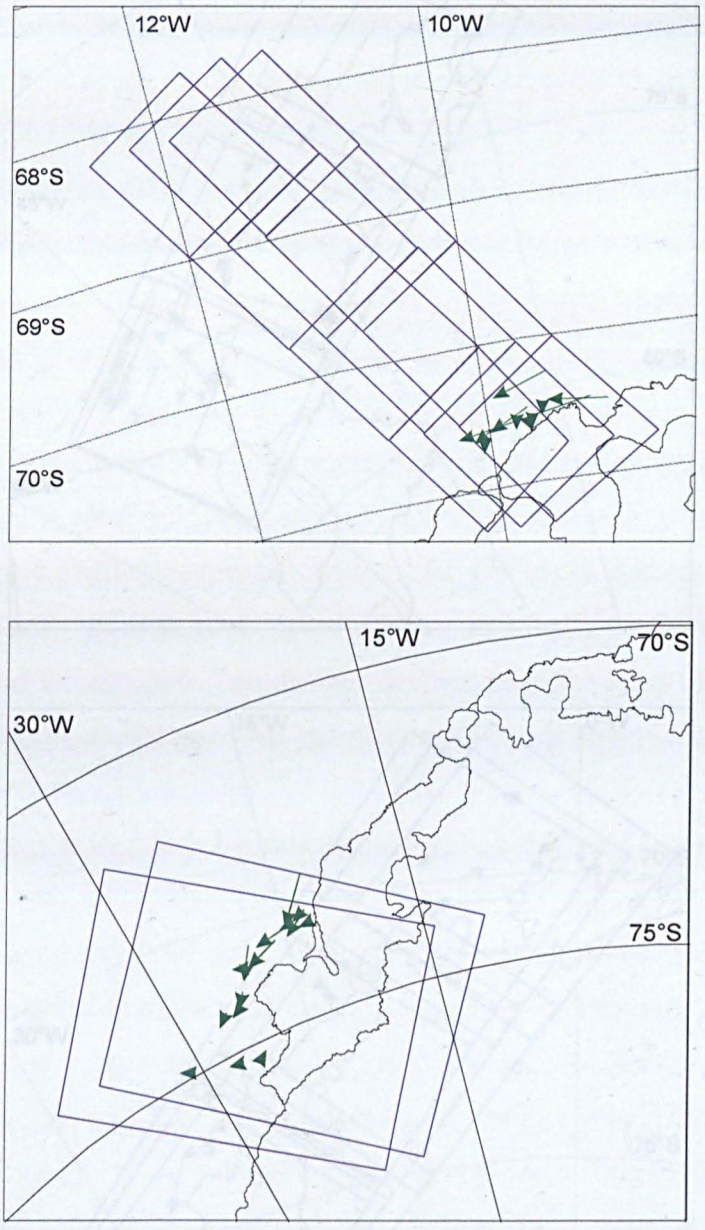

Figure 46 - Iceberg movements in the Weddell Sea in the winter of 1992 from PRI images (top) and summer of 2003/4 from WS images (top).

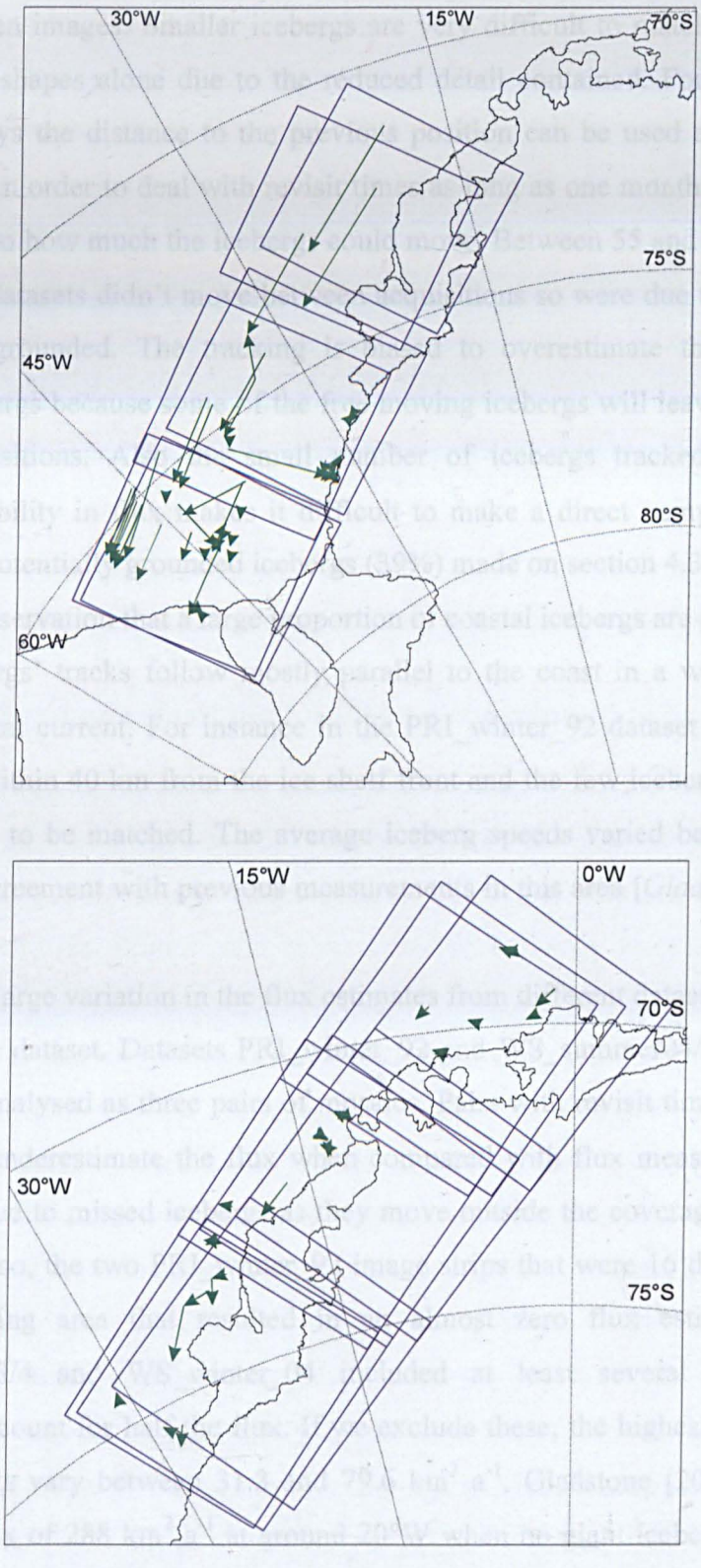

Figure 47 - Iceberg movements in the Weddell Sea in winter of 2004 (top) and the summer of 2004/5 (bottom).

Only icebergs longer than 250 m for PRI images and 750 m for WS images were tracked between images. Smaller icebergs are very difficult to match on the basis of their size and shapes alone due to the reduced detail contained. For revisit times of only a few days the distance to the previous position can be used as a criterion for matching, but in order to deal with revisit times as long as one month, no assumptions were made as to how much the icebergs could move. Between 55 and 81% of icebergs tracked in all datasets didn't move between acquisitions so were due to bathymetry or land-fast-ice, grounded. The tracking is biased to overestimate the proportion of grounded icebergs because some of the free moving icebergs will leave the study area between acquisitions. Also the small number of icebergs tracked and the large temporal variability in flux makes it difficult to make a direct comparison with the proportion of potentially grounded icebergs (39%) made on section 4.3. Nevertheless it supports the observation that a large proportion of coastal icebergs are grounded.

The icebergs' tracks follow mostly parallel to the coast in a westward fashion along the coastal current. For instance in the PRI_winter_92 dataset all the icebergs tracked were within 40 km from the ice shelf front and the few icebergs further away were too small to be matched. The average iceberg speeds varied between 0.04 and 0.08 m s^{-1} in agreement with previous measurements in this area [*Gladstone and Bigg*, 2002].

There is a large variation in the flux estimates from different datasets and different dates with each dataset. Datasets PRI_winter_92 and WS_summer04/5 covered three dates so were analysed as three pairs of mosaics. Pairs with revisit times larger than 8 days result in underestimate the flux when compared with flux measurement 3 days apart. This is due to missed icebergs as they move outside the coverage area between acquisitions. Also, the two PRI_winter_92 image strips that were 16 days apart had a small overlapping area that resulted in an almost zero flux estimate. Datasets WS_summer_03/4 and WS_winter_04 included at least several decakilometric icebergs that account for half the flux. If we exclude these, the highest measurements for each datasets vary between 31.3 and 79.6 km^2 a^{-1}. Gladstone [2001] recorded a much higher flux of 288 km^2 a^{-1} at around 20°W when no giant icebergs were in the area. As it was pointed out before, the average iceberg speed is comparable to Gladstone [2001]; the difference in the flux measurements relies on the higher iceberg densities observed by Gladstone over the one month of the study. The present results uses shorter time-series of two or three acquisitions, but cover a much larger area - up

to 1200 × 400 km - and for four different periods. These measurements are closer to the simulated coastal flux in the same study of 29 km^2 a^{-1} for an Antarctic calving flux of 1340 Gt a^{-1}.

The clustering in iceberg distribution that we identified in section 4.3 has resulted in a large variance in the flux measurements conducted here. In order to measure the average iceberg flux along the coast more accurately, more image pairs, covering a period of several months, would have to be used. The time difference between images should be under 6 days as even though most icebergs will still be within coverage, it might prove impossible to match them due to the uncertainty as to where they might have drifted. This limited the matching to larger, more identifiable, icebergs causing an underestimate in the total flux.

4.6 Recommendations for iceberg monitoring schemes

Icebergs are an important component of the climate system at high latitudes and by transferring heat and fresh water between the ice sheets and the ocean have the potential to influence oceanic processes and its interaction with the atmosphere. The knowledge of the distribution and movements of icebergs would allow a better understanding of the role played by icebergs in altering the stability of the water column, sea water chemistry and release of nutrients to the ocean.

In order to attain these aims, it is desirable to characterise **the average distribution of iceberg meltwater in the ocean**. A first objective would be to establish a baseline as an average of several years within a decade and a secondary objective to keep a monitoring scheme in place and possibly to extend it back in time, as allowed by archived data. Due to the extent of the Southern Ocean and its limited accessibility in winter, microwave satellite remote sensing is the most powerful tool for a monitoring scheme of this type. Synoptic descriptions of iceberg distribution in the Southern Ocean, as produced here for the coastal area, can be used to determine meltwater loss to the ocean. An average iceberg distribution can be combined with an iceberg trajectory and melting model, forced by an ocean circulation and atmospheric model, to estimate meltwater losses.

In this chapter we have produced a map of iceberg distribution map in coastal areas around September 1997 and part of the Weddell Sea around September 2004. A distribution for the whole Southern Ocean does not yet exist, therefore in Chapter 6 we used a different approach from the one proposed above. The melting of icebergs up to 2 km was obtained from an iceberg model simulation for the whole Southern Ocean [*Gladstone*, 2001; *Gladstone et al.*, 2001]. The positions of very large bergs are monitored by satellite, so we used these tracks to model iceberg erosion. While in this case a lagrangian approach was used for the tracks of large icebergs, with an observed iceberg distribution a eulerian approach would be used. Also, the grounding of icebergs could be taken into account by using the bathymetry data, as done in section 4.3.

The average iceberg distribution can be determined by analysis of several SAR mosaics of the Southern Ocean. An area of 20×10^6 km^2 requires from 200 to 300 Envisat WS or RADARSAT-1/2 ScanSAR scenes. These can be processed using the computer-based algorithm of Chapter 3 and [*Silva and Bigg*, 2005] to detect icebergs according to the dectability function in Figure 28. We didn't observe differences in iceberg velocities between summer and winter, but in winter a large number of icebergs are immobilised close to the coast, embedded in land-fast sea ice. With the break-up of the sea ice at the beginning of summer there might be larger iceberg fluxes. Therefore it is important to standardize the image acquisitions for the synoptic mosaics always from the same month. The first priority in choosing a date is to avoid temperature close or above melting, as this will depress the ice backscattering coefficient and reduce the contrast that allows the detection of icebergs to be automatically detected. As a second priority the sea ice cover should be low or young ice should be present to allow icebergs to be easily detected against the dark background and avoid false alarms from compression ridges on multiyear sea ice. Because both priorities are in conflict, an optimal time will be March to May, when air temperatures dip below zero, even on the Antarctic Peninsula, but sea ice cover is still low [*King and Turner*, 1997].

The following errors will affect the final distribution map: i) missed icebergs; ii) underestimated area due to segmentation algorithm (see Chapter 3); iii) uncertainty in estimating iceberg thickness and ice density. The detectability of icebergs of 0.25 km^2 is 90% and it increases with iceberg size. This, for a population of small icebergs such as on the test on Ruppert Coast (Figure 27) the analysis results in an underestimate of

12% on the surface volume compared with the reference classification. Using the detectability curve to correct for missed icebergs on the RMAP mosaic it was shown in section 4.3 that this resulted in underestimating 9% of volume of icebergs smaller than 100 km^2 and only 3.8 % of the total volume of icebergs in the RAMP mosaic.

As long as error ii) is corrected for as described in Chapter 3, the total area classification error for a typical iceberg population will under 15%. Error iii) will accrue to volume and mass estimates which will reflect on meltwater errors.

A second objective is to describe the **distribution and movements of all icebergs larger than 10 km^2**. This accounts for around two thirds of the total Antarctic iceberg mass as can be seen on the cumulative volume plot in Figure 40. An accurate, exhaustive and long term trajectory database for large icebergs allows us to:

- study the longevity, melting and break-up of giant icebergs;
- study the impact of giant icebergs on the ecosystems, sea ice cover, and on the atmospheric and oceanic conditions;
- monitor the temporal variability of iceberg calving in an economical fashion.

The National Ice Centre (NIC) monitors the position of icebergs longer than 18 km since 1978 (the database is available from their website http://www.natice.noaa.gov/products/iceberg/). The major limitations are: high iceberg size limit; not having iceberg shape or orientation information (only major and minor axis length); poor geographic resolution, size measurements, temporal frequency and break-up information. David Long, from the Brigham Young University, keeps another iceberg database that is meant to supplement the NIC database (available for download at http://www.scp.byu.edu/current_icebergs.html). This is in fact a collection of databases, each produced with a satellite sensor and for a different period of time. For example the microwave scatterometer QuikSCAT is used from the period 1999 to the present and detects icebergs larger than 5 km [*Long et al.*, 2002]. However it does not have iceberg size or shape information and has a different database for each sensor, covering a different period, instead of having a unified and comparable timeline. The QuikSCAT sensor has 6×25 km resolution, but using a resolution enhancing technique it can be increased to 5 km. A better imagery for tracking large icebergs is the Global Monitoring Mode of the ENVISAT ASAR instrument which

started in early 2004. It has a resolution of 1 km and produces global strips of 40000 × 400 km allowing for better than daily revisits in high latitude areas. For the period covered by these data it should be possible to significantly improve the description of iceberg calving, movements and erosion for a wide range or iceberg sizes compared with the NIC or BYU databases.

4.7 Conclusions

The iceberg detection and tracking algorithm has been validated and its performance characterised on medium resolution SAR images that afford a wider spatial coverage. This was applied to two SAR mosaics and allowed the first census of iceberg distribution for the whole coast and part of the Weddell Sea. According to our estimates as much as 39% of the detected icebergs might be stranded and even the free floating icebergs exhibit a strongly clustered distribution pattern.

The size distribution shows the relevance in terms of ice volume of two iceberg size classes: one kilometre and multi-decakilometric icebergs. A simple time-dependent model for iceberg size was used to try and reproduce the observed bimodal size distribution. The simple melting model was able to reproduce the observed size distribution so this indicates that it to be an adequate parameterisation of several iceberg erosion processes. The results also indicate that the one kilometre mode exists in the calving distribution and is not exclusively a result of break-up process.

Four measurements of iceberg fluxes along the coast were produced for different periods. Images acquired less than 9 days apart are less prone to icebergs being missed and these escape detection, but nevertheless there is a large variation in the densities and consequently iceberg fluxes measured. This is a result of the high clustering of icebergs already measured in section 4.4. It was concluded that if this method is to return accurate results, a more intensive sampling has to be employed.

In order to integrate the knowledge of iceberg distribution into climate models it is considered desirable to characterise the average distribution of iceberg meltwater in the ocean. This can be done using several censuses such as the ones presented here, but covering the Southern Ocean south of the Polar Front, where the ocean is weakly stratified and therefore meltwater is likely to have a stronger effect.

Another desirable objective is to monitor the distribution and movements of all icebergs larger than 10 km^2. According to the observations from coastal Antarctica, this accounts for over two thirds of the iceberg ice volume so it is an effective way of iceberg monitoring. This is achievable by using ENVISAT global coverage imagery, available since 2004 only, which provides daily 1 km resolution images.

Chapter 5 The contribution of giant icebergs to the Southern Ocean freshwater flux

The contents of this chapter were published as a paper in the Journal of Geophysical Research-Oceans [*Silva et al.*, 2006]. The other two co-authors participated through discussing and revising the manuscript.

5.1 Introduction

Very large, tabular icebergs calve from the Antarctic ice shelves and glacier tongues. Some of these icebergs more than a hundred kilometres long and can take over than a decade to melt, slowly drifting in the counter-clockwise coastal current or grounded in the very cold waters close to the coast. Such large masses of ice can affect water circulation in their vicinity [*Grosfeld et al.*, 2001], block sea ice movements [*Markus*, 1996] and consequently cause disruption to marine ecosystems [*Arrigo et al.*, 2002], and can cause other icebergs to calve through collision with the ice front [*Swithinbank et al.*, 1977]. Icebergs larger than 100 km^2 are thought to carry around half the ice volume of the entire iceberg population [*Jacobs et al.*, 1992]. This proportion was confirmed by our observations of icebergs floating in coastal Southern Ocean and the Weddell Sea (Figure 40).

The effect of the melting of icebergs (and ice shelves) differs from precipitation or sea ice melting in that the freshwater can be released below the very cool surface Winter Water (WW) and, by mixing with the warmer Circumpolar Deep Water (CDW), it may increase its buoyancy and cause warm water intrusions at the surface [*Jenkins*, 1999]. This has the effect of warming the surface, potentially reducing sea ice formation and increasing the water column stability. On the other hand, as Jenkins [1999] points out, if the mixing of the iceberg meltwater occurs above the pycnocline the result would be to cool the upper-layer water favouring the thickening of sea ice. Accordingly, the inclusion of an ice shelf basal melting parameterization in a global ice-ocean model produced thickening of sea ice in the Weddell Sea, Ross Sea and in front of the Amery ice shelf [*Beckmann and Goosse*, 2003]. Another effect in this simulation was the freshening and cooling of the shelf waters. Freshening of the

coastal waters has also been related to intensification of the shelf break current [*Hellmer and Beckmann*, 1998].

In this study giant icebergs contributed alone with an average of 21 mSv (1 mSv = 10^3 m^3 s^{-1}) of freshwater to the Southern Ocean south of 63°S, although it has a large temporal and spatial variability which can make it more significant locally. Gladstone *et al.* [2001] used an iceberg trajectory model seeded with climatological calving fluxes to calculate the climatological pattern of meltwater injection around Antarctica. They estimated that the rate of injection could be higher than 0.5 m m^{-2} yr^{-1} in some locations around the coast, comparable to the precipitation minus evaporation contribution calculated by Turner *et al.* [1999]. The simulation by Gladstone *et al.* [2001] only considered icebergs up to 2.2 km in length. As they noted, very large icebergs appear to have different dynamics. For instance, Lichey and Hellmer [2001] used an iceberg drift model to show that the trajectory of giant iceberg C17 in the Weddell Sea was more dependent on sea ice than previously thought. Here we present the meltwater distribution estimated from observed giant iceberg tracks for the period 1987-2003, study its temporal variability and discuss its relevance to the freshwater flux of the Southern Ocean and in particular to the Weddell Sea.

5.2 Iceberg observations

The National Ice Center (NIC) maintains a database of "giant icebergs", i.e. bergs larger than 10 nautical miles (1 nm ≈ 1.853 km) in the long axis, which is available from their website (http://www.natice.noaa.gov/). The unique identifier, position and approximate measurements for the long and short axis are recorded every 9 days (median value). Icebergs larger than 10 nm, or smaller than 10 nm but resulting from the break-up of a larger iceberg, are recorded in the database for as long as they stay south of 60°S. The database spans from 1979 to the present.

The NIC uses several types of satellite imagery depending on the iceberg size and position. These include optical imagery, microwave radiometry and synthetic aperture radar (SAR). In 1986 the NIC started using the Operational Line Scan sensor onboard the Defence Meteorological Satellite Program series. This wide swath optical radiometer improved the available satellite coverage and resulted in a larger number of

icebergs being tracked [*Long et al.*, 2002]. As this gave longer and more complete iceberg tracks, we restricted the dataset used in our analysis of iceberg melting to the period 1987-2003. The complete 1979-2003 dataset is used, however, for the calculation of yearly average calving mass and numbers. Numerous errors in the data, which became apparent by plotting the trajectories, were corrected from the database.

The NIC database contains information about both the iceberg position and changes in horizontal size. However, the size measurements (in nautical miles) are coarse and updated infrequently. In order to find out if these reductions corresponded to abrupt changes in size or to progressive melting we used freely available AVHRR and MODIS satellite images with resolutions of 1 km in summer and 4 km in winter [*Scambos et al.*, 2001] to analyze the size reductions recorded in the database. In 15 out of the 90 recorded reductions in size it was possible to find satellite images of the target iceberg before and after the date of the size reduction on the NIC database. In 12 of these, there were no measurable changes in size, indicating a progressive melting or break-up of icebergs below the image resolution, combined with infrequent updating of the iceberg size measurements.

We estimated the spread of meltwater resulting from this progressive reduction by smoothing the size observations, resampling each iceberg dimension every 365 days and interpolating it onto the observed dates using a piecewise cubic Hermite function. This procedure yields a continuous, monotonically decreasing, smoothed version of the size measurements: it is equivalent to spreading the meltwater associated with a reduction in the measurements along the iceberg tracks, and over a period of one year (Figure 48). We also used resampling periods of 100 and 1000 days, and only slight changes in meltwater distribution were observed. For a conservative estimate of rate of change of local meltwater injection for the Weddell and Ross Seas, an extreme smoothing was used by interpolating linearly between the first and last observation.

5.3 Calving and drifting of giant icebergs

The calving of a large giant iceberg is an infrequent event for any ice shelf. As what might be an extreme example, an iceberg of 10000 km^2 in area broke from the Amery Ice Shelf in 1964 and Fricker and colleagues [2002] estimated that it would

take 60 to 70 years for another such iceberg to be produced by the same ice shelf. Furthermore, only a small number of ice-shelves and glacier tongues can produce icebergs of this size. This leads to a large variation in the number, but especially the mass of giant icebergs calved each year, as can be seen on Figure 49. There are two prominent peaks in the calving history of giant icebergs for the period 1979-2003, and these are attributed to a small number of very large calving events: in 1986 iceberg A20 calved from the Larsen Ice Shelf and icebergs A22, A23 and A24 calved from Filchner Ice Shelf; icebergs A43 and A44 calved from Ronne Ice Shelf and iceberg B15 from Ross Ice Shelf in 2000. For comparison, the final collapse of the remains of Larsen B Ice Shelf in 2002 only involved approximately 500 Gt of ice [*Shepherd et al.*, 2003], although the icebergs resulting from this highly crevassed ice shelf were mostly too small to be tracked by the NIC. According to these data, the average freshwater mass calved annually as giant icebergs in the period 1979-2003 was 1089±300 Gt yr^{-1}. This was calculated by approximating the iceberg as an ellipsoid parallelepiped with the long axis, L_a, and short axis, L_b, as given by the NIC [*Jacobs et al.*, 1992]. The basal area

$$A_B = \frac{\pi}{4} L_a L_b \tag{5.1}$$

was multiplied by an initial iceberg thickness of 250 m [*Jacobs et al.*, 1992] and by an average density of 850 kg m^{-3} [*Keys et al.*, 1990; *Keys and Fowler*, 1989] to obtain the total ice mass. The error margin of 300 Gt yr^{-1} was estimated taking into consideration the possible range of average ice density and ice shelf thickness.

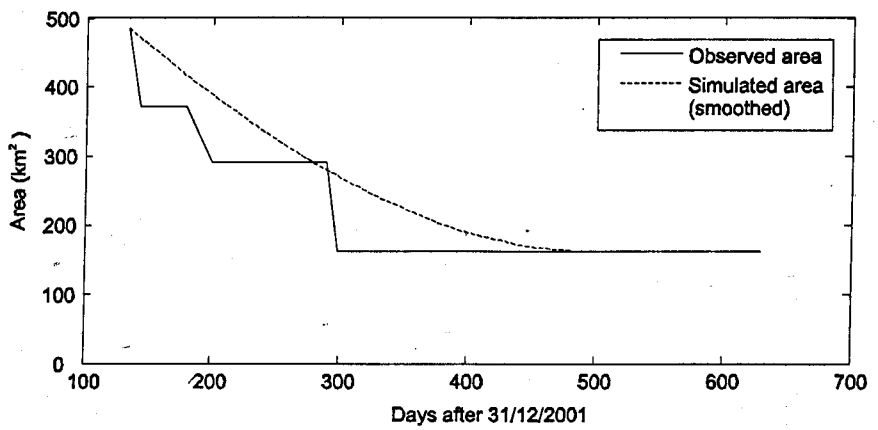

Figure 48 - Area of iceberg D17 i) estimated from observations and ii) smoothed to simulate spreading of meltwater from smaller icebergs along its trajectory.

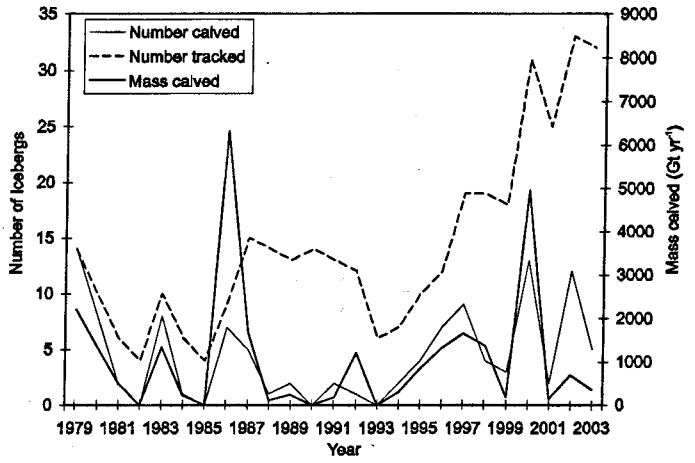

Figure 49 - Number and mass of giant icebergs (>10 nm or ≈ 18.5 km) recorded by the National Ice Center from 1979 to 2003. "Calved" icebergs are considered to be the icebergs first detected in a specific year, while "tracked" icebergs are all "mother" icebergs observed in the same year. The mass was calculated by approximating each iceberg as an ellipsoidal parallelepiped, assuming an initial thickness of 250 m and an average ice density of 850 kg m^{-3}.

A complementary iceberg drift database covering the period 1992 to the present [*Long et al.*, 2002] lists several tens of additional icebergs missed by the NIC in recent years. Long and colleagues were able to detect these additional bergs by using an improved resolution algorithm applied to frequent, large coverage, but low resolution, microwave scatterometer images. The extra observations were not included in our survey as it constitutes a shorter time series and does not include iceberg size measurements. Although not including these extra icebergs might result in underestimating the total mass of giant icebergs, most of those missing from the NIC database are icebergs too small to be detected by the NIC that resulted from the large calving events of 1999-2000 [*Long et al.*, 2002].

The calving flux of icebergs smaller than 10 nm bears more uncertainties as these are not detected in the daily low resolution satellite imagery. Previous sources of iceberg drift include the Soviet Antarctic Survey [*Bakayev*, 1966], icebergs tracked

using satellite beacons [*Tchernia and Jeannin*, 1984] and modelled trajectories [*Gladstone*, 2001; *Gladstone et al.*, 2001]. These sources show that the pattern of drift of smaller bergs differs from that of giant icebergs (Figure 50) in that giant icebergs generally stay closer to the coast. This is because the Coriolis force, which pushes icebergs flowing counter-clockwise in the coastal current towards the coast, is proportional to the iceberg's mass and hence volume. For an increasing iceberg size the Coriolis force will grow faster than the drag from water and wind, which is proportional to the area over which the respective drag acts. For the same reason smaller bergs are more likely to drift away from the coast around the Kerguelen plateau in East Antarctica, as the topographic steering more easily overcomes the weaker Coriolis force. As we will see in the next section, by comparing the simulation output for smaller bergs [*Gladstone et al.*, 2001] with the present study, another difference becomes evident: only 3% of the mass of smaller icebergs passes north of 63°S compared with an estimated 35% for giant icebergs. This is again because of the smaller area:volume ratio for larger icebergs, leading to slower attrition.

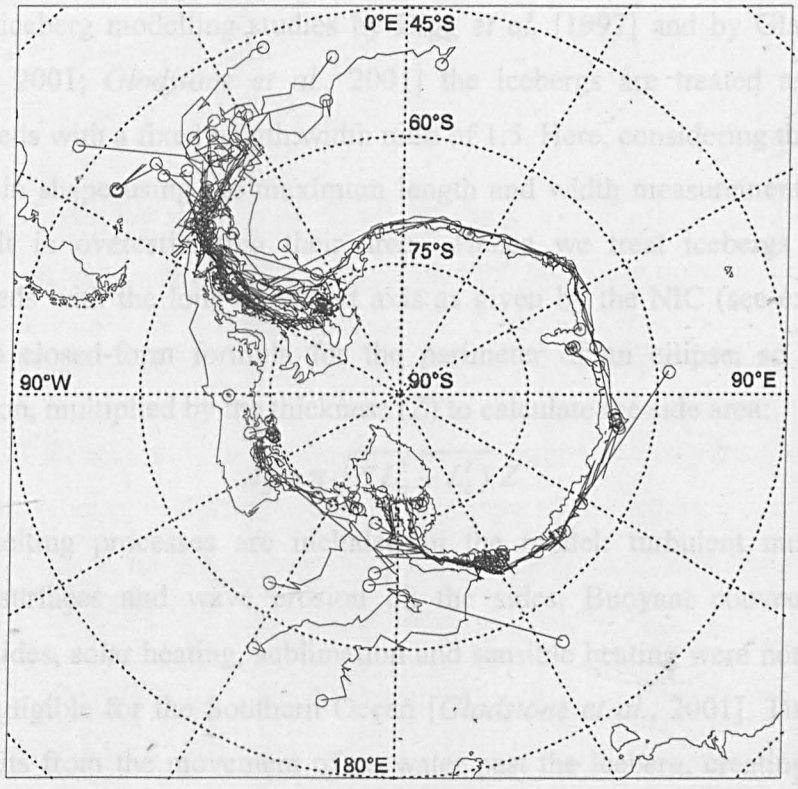

Figure 50 - Trajectories of giant icebergs as tracked by the National Ice Center for the period 1987-2003. Circles mark where tracks end.

5.4 Iceberg melting

5.4.1 Observations and modelling

We combined the observations of giant icebergs' drift and size with modelling of basal melting to calculate meltwater injection in the ocean. The side wall melting was also simulated to compare with the observations.

Additionally to the NIC database, we used several climatological forcing fields for the simulations. Fields of ocean temperature and currents were obtained from the averages of years 8 to 11 of the OCCAM ocean model output [*de Cuevas et al.*, 1999]. For each of the top layers of the model ocean temperatures were averaged monthly, and currents seasonally. The 0.25° spatial resolution was averaged to 1°, as giant icebergs can be thousands of square kilometres in area. Monthly averages of surface winds were obtained from European Centre for Medium-Range Weather Forecasts (ECMWF) 2.5° ERA-40 reanalysis data, averaged over the period 1987 to 2003. The monthly average sea ice concentrations were taken from remote sensing derived data (SMMR and SSM/I microwave radiometers) averaged over the period 1973 to 1991 [*Schweitzer*, 1993].

In the iceberg modelling studies by Bigg *et al.* [1997] and by Gladstone *et al.* [*Gladstone*, 2001; *Gladstone et al.*, 2001] the icebergs are treated as rectangular parallelepipeds with a fixed length:width ratio of 1.5. Here, considering the bergs to be rectangular in shape using the maximum length and width measurements from NIC, would result in overestimating their areas. Hence we treat icebergs as ellipsoid parallelepipeds with the long and short axis as given by the NIC (see expression 1). There is no closed-form formula for the perimeter of an ellipse, so we used an approximation, multiplied by the thickness (Z) to calculate the side area:

$$A_S \approx \pi\sqrt{2(L_a^2 + L_b^2)}\, Z \qquad (5.2)$$

Two melting processes are included in the model: turbulent melting at the submerged surfaces and wave erosion on the sides. Buoyant convection on the submerged sides, solar heating, sublimation and sensible heating were not included as these are negligible for the Southern Ocean [*Gladstone et al.*, 2001]. Turbulent heat transfer results from the movement of seawater past the iceberg, creating turbulence that transports heat to its surfaces. We calculated the turbulent melt rate using the three equation formulation of Holland and Jenkins [1999], assuming a neutral boundary

layer with no effect of melting on the stratification. The temperature at the interface between the iceberg base and the ocean, T_B, is given by the local freezing point:

$$T_B = aS_B + b + cp_B \tag{5.3}$$

where the equation of state was linearised and the following constants were used: a = -5.73×10^{-2} °C psu^{-1}; b = 8.32×10^{-2} °C and c = -7.61×10^{-4} °C dbar^{-1}. S_B is the salinity at the iceberg base and p_B the pressure at the base. The remaining two equations result from the conservation of heat and conservation of salt, respectively:

$$|u|\gamma_T(T_\infty - T_B) = -M_T \frac{L + \Delta T c_i}{c_w} \tag{5.4}$$

$$|u|\gamma_S(S_\infty - S_B) = -M_T S_B \tag{5.5}$$

where $|u|$ is the water speed relative to the iceberg surface; γ_T = 6×10^{-4} and γ_S = 2.2×10^{-5} are coefficients of heat and salt transfer, respectively, from water to ice; S_∞ and S_B are the far-field and basal salinities and, equivalently, T_∞ and T_B are the far-field and basal temperatures; L = 3.35×10^5 J kg^{-1} is the latent heat of fusion of ice; c_w = 4000 J kg^{-1} °C^{-1} and c_i = 2010 J kg^{-1} °C^{-1} are the specific heat capacities of water and ice, respectively; ΔT = 20°C is an average value for the temperature difference between the iceberg core and the bottom surface [*Weeks and Mellor*, 1978]; and M_T is the turbulent melt rate. Far-field values are taken as the OCCAM model values for the layer below the iceberg base: *e.g.* for an iceberg draft of 200 m the model layer below is centred at 244 m.

S_B and T_B can be eliminated from the three equations (5.3), (5.4) and (5.5), resulting in a quadratic equation for M_T. The solution of the quadratic gives M_T as a function of water speed and of superheating, T_{sh}, here defined as

$$T_{sh} = T_\infty - (aS_\infty + b + cp_B) \tag{5.6}$$

This is the difference between the far field *in situ* water temperature and its freezing point, the latter being calculated using the pressure at the ice base and the far-field salinity. Of the two solutions to the quadratic only one is physically meaningful as it is shows melting (negative values of M_T) for positive values of T_{sh}:

$$M_T = \frac{-B - \sqrt{B^2 - 4AC}}{2A}, \text{ where} \tag{5.7}$$

$$A = \frac{L + \Delta T c_i}{|u|\gamma_T c_w} \tag{5.8}$$

$$B = T_{sh} + aS_{\infty} - \frac{L + \Delta T c_i}{c_w \gamma_T} \gamma_S \tag{5.9}$$

$$C = -|u| \gamma_S T_{sh} \tag{5.10}$$

Figure 51 shows that the meltrate, M_T, varies almost linearly with the ambient water temperature, T_∞. The fixed parameter ΔT depends on the iceberg's origin and on its age and it is likely to vary between -15°C (a core temperature of -13°C) and -25°C, but the this uncertainty causes a variation on M_T of only 5% (see Figure 51).

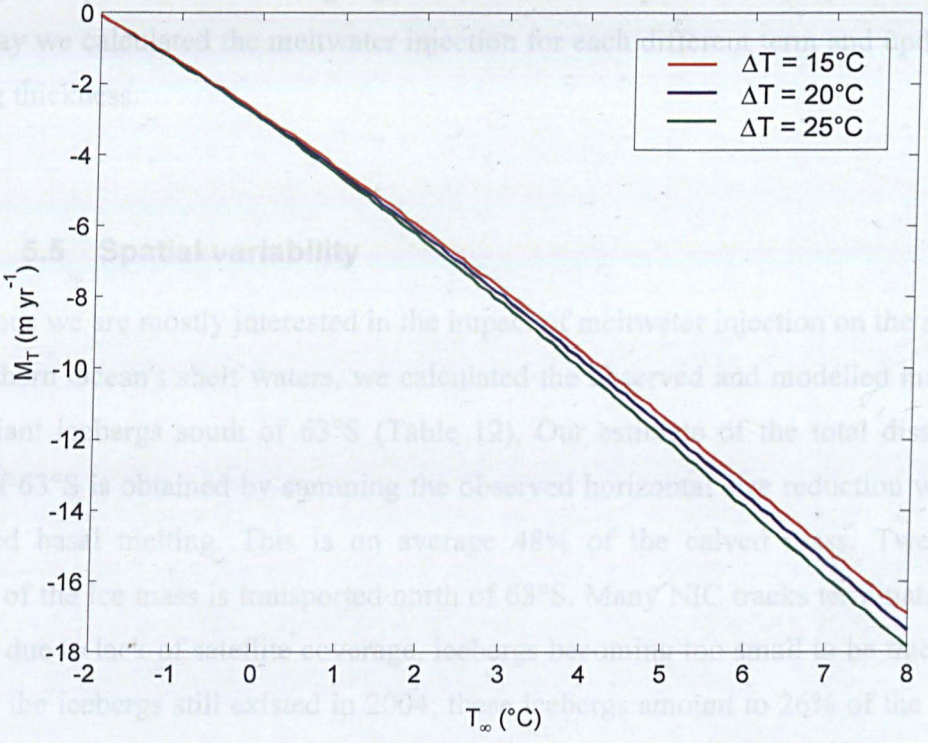

Figure 51 - Melting model as a function of the water temperature in the far field, T_∞, and difference between the iceberg core temperature and the bottom temperature, ΔT. This response was calculated for a depth of 200 m and a water salinity of 35 psu.

Waves are responsible for eroding the iceberg sides, both below and above the water line, as overhanging slabs are also considered to fall. Gladstone *et al.* [2001] parameterized an empirical term [*Bigg et al.*, 1997] to take into account the dependence of erosion on the water temperature, and the damping effect of the sea ice. The wave erosion, M_W, (in m day^{-1}) is given by

$$M_W = \frac{1}{12} S_S \left[1 - \cos(C^3 \pi)\right](T_W + 2) \qquad (5.11)$$

where S_s is the sea state on the Beaufort scale, calculated from the wind speed, and C is sea ice concentration (in %).

In order to calculate the meltwater flux these two terms must be multiplied by the appropriate iceberg surface areas. Turbulent melting is applied to both the bottom of the iceberg and the submerged sides and wave erosion to half the side area (the half exposed to the wind). The NIC observations are generally spaced days apart so we linearly interpolated the iceberg's position and re-sampled it at daily intervals. For each day we calculated the meltwater injection for each different term and updated the iceberg thickness.

5.5 Spatial variability

Since we are mostly interested in the impact of meltwater injection on the stability of Southern Ocean's shelf waters, we calculated the observed and modelled mass loss from giant icebergs south of 63°S (Table 12). Our estimate of the total dissolution south of 63°S is obtained by summing the observed horizontal size reduction with the modelled basal melting. This is on average 48% of the calved mass. Twenty-six percent of the ice mass is transported north of 63°S. Many NIC tracks terminate south of 63°S due to lack of satellite coverage, icebergs becoming too small to be tracked or because the icebergs still existed in 2004; these icebergs amount to 26% of the calved mass. Incomplete tracks are spread all around the coast (Figure 50), and we assume that these icebergs will eventually melt south of 63°S and be transported north in the same proportion as the remaining icebergs. This results in an estimated 65% of the giant icebergs' mass melting south of 63°S, and 35% being transported further north (Table 12) compared with only 3% in the simulations performed for smaller bergs [*Gladstone et al.*, 2001]. Observed reductions in size were more than five times the modelled side melting, and we attribute at least some of this difference to break-up into smaller icebergs, the latter not being accounted for by the model. The turbulent basal melting was comparable in size with the observed size reduction. Within the side melting terms the wave erosion is by far the most important. The errors intervals included in Table 12 were the result of a sensitivity analysis that is detailed in section 5.6.

Table 12 - Yearly averages of ice mass lost by giant icebergs for 1987-2003 south of 63°S. The observed iceberg sizes were smoothed by resampling every 365 days and interpolated as described in the text. Corrected terms assume that icebergs with interrupted tracks melted in the same proportion as the ones with tracks that reach north of 63°S. Modelled side melting is included for comparison with the observed reduction but was not included in the remaining results. The error intervals result the model's sensitivity to iceberg thickness and seawater temperature (see section 5.6).

	Mass flux (Gt yr^{-1})	
	Measured	Corrected for incomplete tracks
Calved giant icebergs	1035±414	–
Mass lost south of 63S	493±164 (48%)	668±237 (65%)
Observed side reduction	241±114	327±198
Modelled bottom melting	252±64	341±144
Transport north of 63°S	271±145 (26%)	533±247 (35%)
Incomplete tracks	272±172 (26%)	–
Modelled side melting	43.7±27	59.2±39
Wave erosion	39.0±23	52.9±33
Turbulent melting	4.6±4	6.3±5

Existing estimates of the total number of smaller icebergs rely on ship-based observations [*Hamley and Budd*, 1986; *Orheim*, 1988] which are biased by the location of ship's routes. Also, these estimates do not take into account the fact that a portion of the small bergs resulting from the break-up of giant icebergs. Orheim [personal communication in *Jacobs et al.*, 1992] estimated the calving flux of small icebergs as 1200 Gt yr^{-1} although Jacobs *et al.* [1992] chose to use a more conservative estimate of 1008 Gt yr^{-1}. This incorrectly includes in the calving flux small icebergs resulting from the breaking up of giant icebergs. Assuming that the side melting is correctly represented in our model, then the difference between observed size reduction and side melting (327-59 = 268 Gt yr^{-1}) is the outcome of break-up. Subtracting this term from the ship-based estimates of 1200 Gt yr^{-1} results in a small-iceberg calving flux of 932 Gt yr^{-1} of freshwater. The total iceberg meltwater (Figure 52c) is the combination of three terms: giant icebergs scaled to take into account the incomplete tracks, so that 668 Gt yr^{-1} will melt south of 63°S (see Table 12); small icebergs (from Gladstone *et al.* [2001]) scaled down to the calving flux of 932 Gt yr^{-1}; and small icebergs resulting from giant bergs, taken to be the Gladstone *et al.* map scaled down to a total of 268 Gt

yr^{-1}. This simplification ignores the fact that small icebergs resulting from the break up of giant icebergs will generally "calve" further away from the coast and further west than assumed by Gladstone *et al.* [2001].

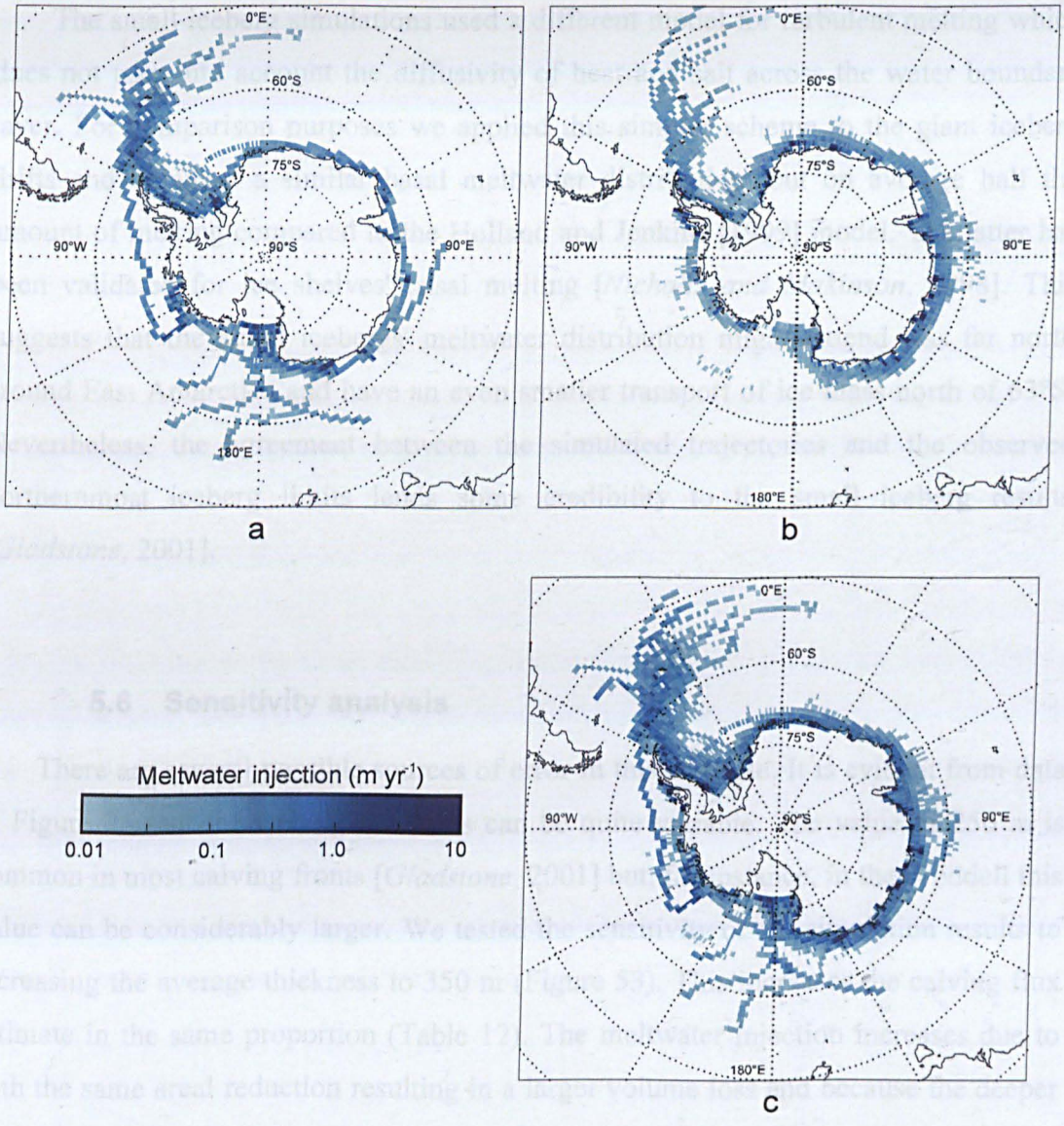

Figure 52 - Distribution of iceberg meltwater in the Southern Ocean calculated from: (a) giant iceberg trajectories for the period 1987-2003 in this study; (b) climatological run of a model for icebergs up to 2.2 km in size [*Gladstone*, 2001] and (c) the combination of the giant and small icebergs (see text for details).

The average giant berg meltwater distribution (Figure 52a) differs from the simulations performed for smaller icebergs (Figure 52b): as a consequence of greater

longevity, many giant icebergs reach the Weddell Sea and are often transported further north. Smaller bergs tend to melt closer to their sources. In East Antarctica, for example, smaller bergs drift further away from the coast, entering warmer waters that accelerate their decay.

The small iceberg simulations used a different model for turbulent melting which does not take into account the diffusivity of heat and salt across the water boundary layer. For comparison purposes we applied this simpler scheme to the giant iceberg drifts and obtained a similar basal meltwater distribution, but on average half the amount of melting compared to the Holland and Jenkins [1999] model. The latter has been validated for ice shelves' basal melting [*Nicholls and Makinson*, 1998]. This suggests that the small icebergs' meltwater distribution might extend less far north around East Antarctica and have an even smaller transport of ice mass north of 63°S. Nevertheless, the agreement between the simulated trajectories and the observed northernmost iceberg limits lends some credibility to the small iceberg results [*Gladstone*, 2001].

5.6 Sensitivity analysis

There are several possible sources of error in this estimate. It is evident from data in Figure 25 that the iceberg thickness can be quite variable. The value of 250 m is common in most calving fronts [*Gladstone*, 2001] but, for instance, in the Weddell this value can be considerably larger. We tested the sensitivity of the simulation results to increasing the average thickness to 350 m (Figure 53). This increases the calving flux estimate in the same proportion (Table 12). The meltwater injection increases due to both the same areal reduction resulting in a larger volume loss and because the deeper draft is generally in contact with warmer water, thus melting faster.

The melting estimates rely on an accurate average description of the water velocity and temperature near the ice, for which monthly averages of the OCCAM model were extracted. An analysis of OCCAM model results for the Pacific Ocean showed the near-surface currents to agree well with drifter observations outside the tropical belt [*Saunders et al.*, 1999]. The temperature below the boundary layer in the South Pacific exceeded in places up to 2 degrees the Levitus *et al.* [1994] climatology used to set the initial state [*Saunders et al.*, 1999]. But it is debatable that the

observational climatologies are more accurate than OCCAM fields in coastal areas, due to the sparse sampling and strong smoothing. For instance, Levitus [1994] data does not represent well Western Boundary Currents [*Saunders et al.*, 1999]. Southern Ocean south of the Polar front exhibits a small temperature range leaving little space for OCCAM to produce errors: in the continental shelf waters the temperature down to 200-300 m remains between -2° and 0°C year round, and increases only up to +2°C just south of the Polar Front. We tested the sensitivity of the melting model to an error in the temperature fields of +-20% of the temperature above the freezing point of seawater (~ -1.9°C), or ±0.2× (T+1.9), which is higher that the error observed in the South Pacific (a maximum error or 2°C in 14°C water). The resulting error in the meltwater distribution from giant icebergs was plotted in Figure 53a and b. This resulted in an error approximately of ±20% on the basal melting of giant icebergs bue to the model being approximately linear to the water temperature above freezing (Figure 51). Table 12 includes the error intervals resulting from the sum of the sensitivity to iceberg thickness and water temperature.

This serves to evaluate the sensitivity to uncertainty in the OCCAM temperature field but does not serve as an total error interval for the meltwater estimates. |Other sources or error are likely to be the result of missed iceberg tracks and the crude approach used to spread meltwater along an iceberg track, when in fact the small icebergs will drift away and possibly melt elsewhere. Therefore the usefulness of this study is not to give a realistic mapping of the meltwater distribution in the period 1987-2003 but to show the general pattern of meltwater distribution with realistic general features such as spatial heterogeneity and volume transport north of the polar front.

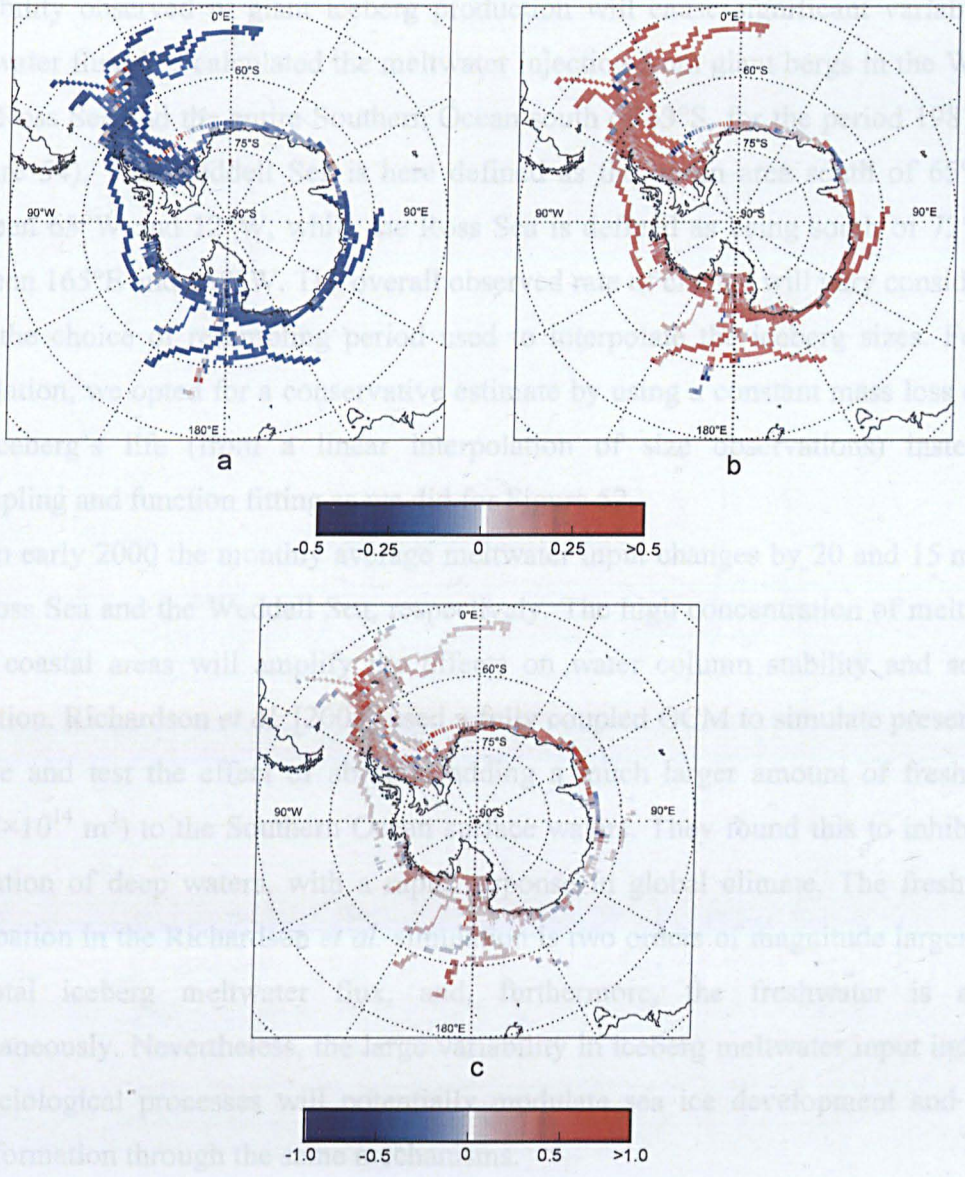

Figure 53 – Sensitivity of the meltwater simulation to changes in water temperature and iceberg thickness. The figures show the variation in the meltwater relative to the original simulation in Figure 52a, by considering: a) 20% reduction in the above freezing water temperature b) a 20% increase in the above freezing water temperature and c) maximum iceberg thickness of 350 m instead of 250 m.

5.7 Temporal variability

Whereas we expect only relatively weak interannual variation in the production of small icebergs [*Orheim*, 1985b; *Orheim*, 1990], the high spatial and temporal

variability observed in giant iceberg production will cause significant variability in meltwater flux. We calculated the meltwater injection from giant bergs in the Weddell Sea, Ross Sea and the entire Southern Ocean south of 63°S, for the period 1987-2003 (Figure 54). The Weddell Sea is here defined as the ocean area south of 65°S and between 63°W and 12°W, while the Ross Sea is defined as being south of 72°S and between 165°E and 150°W. The overall observed rate of change will vary considerably with the choice of resampling period used to interpolate the iceberg sizes. For this calculation, we opted for a conservative estimate by using a constant mass loss during the iceberg's life (from a linear interpolation of size observations) instead of resampling and function fitting as we did for Figure 52.

In early 2000 the monthly average meltwater input changes by 20 and 15 mSv in the Ross Sea and the Weddell Sea, respectively. The high concentration of melting in some coastal areas will amplify the effects on water column stability and sea ice formation. Richardson *et al.* [2005] used a fully coupled GCM to simulate present day climate and test the effect of abruptly adding a much larger amount of freshwater (1.677×10^{14} m^3) to the Southern Ocean surface waters. They found this to inhibit the ventilation of deep waters, with a rapid response in global climate. The freshwater perturbation in the Richardson *et al.* simulation is two orders of magnitude larger than the total iceberg meltwater flux, and, furthermore, the freshwater is added instantaneously. Nevertheless, the large variability in iceberg meltwater input induced by glaciological processes will potentially modulate sea ice development and deep water formation through the same mechanisms.

The meltwater peaks observed in the Weddell and Ross Seas in 2000 were caused by independent groups of icebergs. These included newly calved icebergs such as A43 and A44 in the Weddell Sea and B15 and B17 in the Ross Sea, together with older bergs such as A22 and A23. Other abrupt variations were observed in other regions in different years, as can be seen in the meltwater injection for the whole area south of 63°S (Figure 54). No melting occurred in the Ross Sea during the 1990s because few giant icebergs were tracked in the region and no size reduction occurred. It is also worth noting that there is very little modelled side-wall melting in the Weddell Sea during winter: the high sea ice concentration dampens waves and reduces wave erosion.

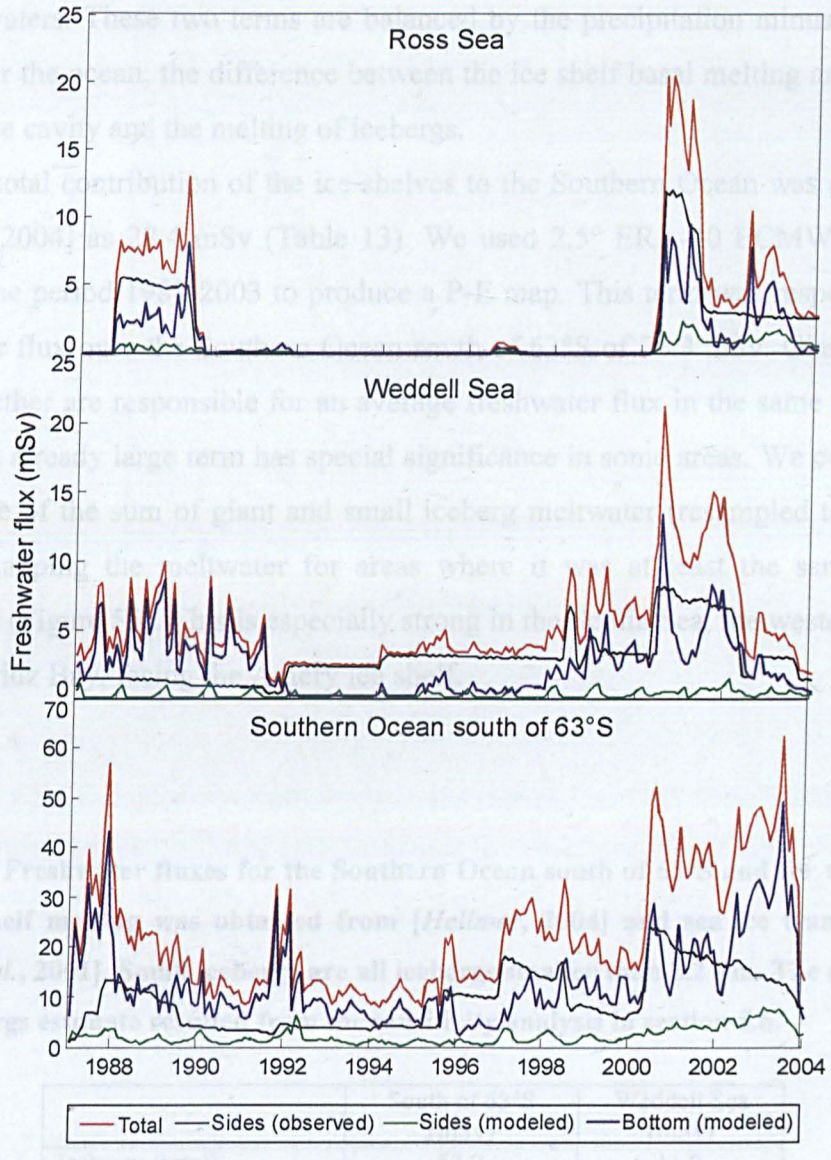

Figure 54 – Monthly averaged meltwater flux from giant icebergs (1 mSv = 10^3 m^3 s^{-1}). Total flux is the sum of observed side reductions and modeled bottom reductions. Changes in total meltwater injection in the Ross and Weddell Seas are as high as 15 mSv over a month.

5.8 Contribution to the freshwater flux

Sea ice forms mostly in open leads near the coast and is transported by wind and currents further north, exporting very large amounts of freshwater from Southern Oceans shelf seas. To this accrues the sinking and export off the shelf of fresh and cold

surface waters. These two terms are balanced by the precipitation minus evaporation (P-E) over the ocean, the difference between the ice shelf basal melting and refreezing deep in the cavity and the melting of icebergs.

The total contribution of the ice shelves to the Southern Ocean was estimated by Hellmer [2004] as 28.4 mSv (Table 13). We used 2.5° ERA-40 ECMWF reanalysis data for the period 1987-2003 to produce a P-E map. This term was responsible for a freshwater flux over the Southern Ocean south of 63°S of 76.3 mSv. Giant and small bergs together are responsible for an average freshwater flux in the same area of 50.7 mSv. This already large term has special significance in some areas. We compared the importance of the sum of giant and small iceberg meltwater (resampled to 2.5°) with P-E by mapping the meltwater for areas where it was at least the same order of magnitude (Figure 55). This is especially strong in the Scotia Sea, the western Weddell Sea and Pridz Bay, facing the Amery ice shelf.

Table 13 – Freshwater fluxes for the Southern Ocean south of 63°S and for the Weddell Sea. Ice shelf melting was obtained from [*Hellmer*, 2004] and sea ice transport from [*Harms et al.*, 2001]. Small icebergs are all icebergs smaller than 2.2 km. The error in the giant icebergs estimate resulted from the sensitivity analysis in section 5.6.

	South of 63°S (mSv)	Weddell Sea (mSv)
Icebergs (total)	53.0	11.9
Giant icebergs	24.9 ± 8.9	7.0 ± 2.5
Small icebergs	29.2	4.9
P-E (ECMWF)	76.3	6.1
Ice shelf melting	28.4	10.1 to 17.9
Sea ice (net input)	–	-50 ± 19

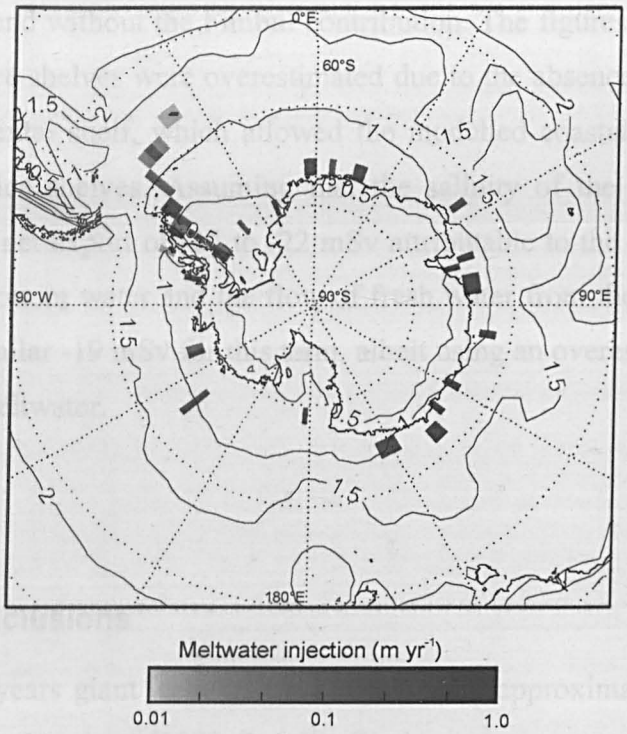

Figure 55 - Climatological precipitation minus evaporation (P-E) from ECMWF ERA40 data (contours in m m^{-2} yr^{-1}) and total iceberg meltwater injection, at 2.5° resolution. The latter is shown only where it is at least of the same order of magnitude as P-E (Meltwater > 0.2×(P-E)).

We have studied the Weddell Sea in more detail and calculated its freshwater balance. Harms *et al.* [2001] used hydrographic observations, satellite passive microwave data and moored upward looking sonar from 1990 to 1994 to study the flux of sea ice in the Weddell. They estimated an average net export of freshwater of 50±19 mSv. In the cited study iceberg meltwater was not taken into account and the P-E estimate did not rely on reanalysis or model output data. We estimate the flux due to all icebergs to be 11.9 mSv and the ECMWF data yielded a P-E flux of 6.1 mSv. *Harms et al.* omitted iceberg meltwater but by using an older and much larger estimate for P-E of 20 mSv ended up with a value comparable to our estimate of 18 mSv for iceberg meltwater plus P-E. The Larsen, Ronne-Filchner and Eastern Weddell ice shelves all contribute freshwater to the Weddell Sea. Some of the water from Fimbul Ice Shelf, further NE, will also enter the Weddell. Hellmer [2004] used an ice-ocean model to estimate the contribution of these ice shelves to be 17.9 and 10.1 mSv,

respectively with and without the Fimbul contribution. The figures for the Fimbul and Eastern Weddell ice shelves were overestimated due to the absence from the model of the narrow continental shelf, which allowed the modelled coastal current to interact directly with the ice shelves. Assuming that the salinity of the Weddell Sea is in balance, there is a net export of -14 to -22 mSv attributable to the difference between newly ventilated bottom water and the flow of fresh water from the east. *Harms et al.* had estimated a similar -19 mSv for this term, albeit using an overestimate for P-E and ignoring iceberg meltwater.

5.9 Conclusions

In the last 25 years giant icebergs have represented approximately half the mass loss of the Antarctic ice sheet (1089 Gt yr^{-1}). We have demonstrated the need to take into account giant icebergs when studying Antarctic iceberg drifting and melting, as these differ from the smaller bergs in both spatial distribution and temporal variability. The differences in drifts are at mostly explained by giant icebergs' large volume:area ratio which causes longer longevity and a stronger Coriolis force in relation to the water, sea ice and wind drag. This causes three observed phenomena: concentration of both icebergs and meltwater very close to coastal areas around most of Antarctica; high concentration of iceberg tracks in the Weddell Sea; and higher transport of mass north of 63°S, that will go mostly into the Antarctic Circumpolar Current (an estimated 35% of calved mass as compared to 3% for small modelled icebergs).

The temporal variability of the distribution of meltwater from giant icebergs might be as important for its effects on the oceans as the amount injected. For the Ross Sea we made a conservative estimate of changes in the local meltwater injection of up to 20 mSv over a month, for the period 1987 to 2003. Smaller variations but of the same order of magnitude were also observed in the Weddell Sea.

Our estimates of iceberg meltwater, taking into account giant icebergs, are shown to be significant in the freshwater balance of both the Southern Ocean overall, where it exceeds ice shelf basal melting, and for the Weddell Sea, where it is larger than P-E.

Chapter 6 Measurements of iceberg thinning and comparison with basal melting simulations

6.1 Introduction

The very large icebergs produced by the Antarctic ice sheet melt over periods of several years. South of the polar front the air temperature is not high enough to cause significant mass loss due to melting. It is the underwater melting, resulting from the conduction of heat from the flowing of seawater around it to the iceberg itself, that is the dominant melting form. SAR imagery can be used to locate icebergs and to observe its contour at water level but the vertical dimension is not observed directly. Satellite altimetry sensors can provide a coarse mesh of point measurements which can then be used to derive basal melting. This chapter contains an attempt at measuring variations in iceberg thickness using a spaceborne laser altimeter. The results together with other published measurements are compared with a simulation of basal melting. This study also serves to test the approach used in the previous chapter to model basal melting for observed tracks of giant icebergs.

6.2 Observations of Iceberg Basal Melting

Icebergs are notoriously difficult objects to study *in situ* due to the logistic requirements for accessing them and the danger of breaking up or rolling over, so it should come as no surprise that few measurements of basal melting have been made. Morgan and Budd [1978] indirectly estimated iceberg basal and side melting off East Antarctica, from iceberg census data: average concentration of icebergs as a function of the distance from the coast; iceberg size distribution and northward drift rates. The melting rate was then related to temperature by using an average sea temperature-latitude relationship for East Antarctica. They obtained basal melt rates of 36-72 m a^{-1} for sea water temperature between 0° and 3°C. Frezzotti *et al.* [1998] estimated basal melting of two giant icebergs on George V Coast, East Antarctica, by measuring the

iceberg shadow on Landsat TM satellite images with the sun at around 20° over the horizon. Over the period 1973 to 1989 these two icebergs stranded close to the coast, at 69°S, suffered an average vertical reduction of 12 m a^{-1}.

One laboratory study contemplated the basal melting of a block of ice. Russell-Head [1980] submerged a flat ice block in homogenous saline water at various temperatures and found comparable basal melting rates to Morgan and Budd's for water between 0° and 3°C. It is worth pointing out that in an ocean environment even a free drifting iceberg would have a turbulent flow at its base caused by the difference between the iceberg's and the current's velocities. This would enhance the heat transfer and accelerate melting.

Satellite based altimeters are potential tools to measure iceberg freeboard changes and have been used for profiling icebergs. This was first done using the microwave altimeter onboard the short-lived Seasat mission [*McIntyre and Cudlip*, 1987; *Rapley et al.*, 1989; *Thomas*, 1984]. The laser altimeter onboard ICESat, called Geoscience Laser Altimeter System (GLAS) [*Zwally et al.*, 2002], produces a footprint of around 70 m while microwave satellite altimeters have footprints of several kilometres. Laser altimeters are also potentially more precise over ice as the near infrared radiation, in the case of GLAS, is backscattered by the top millimetres of the ice surface. The longer wavelength microwaves used in other altimeters can penetrate on ice down to several metres depending on several factors, notably the snow grain size [*Ridley and Partington*, 1988]. One major disadvantage is the scattering and absorption of laser radiation by clouds, biasing estimates [*Fricker et al.*, 2005]. If not corrected for, this can be a serious problem, particularly in coastal Antarctica where the fraction of cloud cover is very high [*Spinhirne et al.*, 2005].

Scambos *et al.* [2005] used GLAS laser altimetry to measure iceberg profiles. They estimated thickness changes for giant icebergs A38A, A38B and A43A by comparing freeboard changes over a period of up to one year, as these drifted northwards on the Weddell Sea. In order to reference each track to a moving iceberg they used 250 m resolution MODIS images near-coincident in time. When the time difference between the image acquisition and the GLAS track was sufficient for the iceberg to move significantly, its contour was translated to fit the track. The measured reductions in freeboard can be seen on Table 14. In this study GLAS altimetry was also used to profile several icebergs in the Ross Sea in two different periods one year

apart with the aim of estimating basal melting. The icebergs studied were B15A, B15J and C16, according to the National Ice Center denomination, and were chosen due to their having an unmanned weather station with GPS. This data was made available to us by Douglas MacAyeal's team from the University of Chicago. The GPS data were used to locate the iceberg at the time of the GLAS tracks so that the laser profile could be referenced on the moving iceberg. Figure 56 show two MODIS images of western side of the Ross Sea with the three icebergs during Laser periods 2a and 3a, respectively.

Table 14 - Iceberg freeboard observations from Scambos et al. [2005]. Thickness was calculated using an iceberg average density of 850 kg m^{-3} and errors were determined by propagating the uncertainty from the elevation measurements.

Iceberg	Freeboard (m)		Date		Days	Thickness change (m a-1)
	Initial	Final	Initial	Final		
A38A	36.5 ±0.5	34.5 ±0.5	21/02/2003	31/10/2003	252	19.3 ±9.7
A38B	31.5 ±0.3	26.5 ±0.5	08/03/2003	19/03/2004	377	32.3 ±5.2
A43A	48.3 ±0.2	47.5 ±0.2	18/03/2003	27/09/2003	193	10.1 ±5.0
A43A	47.8 ±0.2	46.7 ±0.2	18/03/2003	15/03/2004	363	7.4 ±2.7

6.3 GLAS data processing

The pre-processing of GLAS data by NASA was, at the time this study, still work in progress. We used Laser periods 2a and 3a, covering 25/9 to 18/11/2003 and 3/10 to 08/11/2004, in their latest available release (release 21). Laser period 2a is though to be the reference for quality [*Martin et al.*, 2005]. We extracted the fields for elevation, geographic location of the laser spots, transmit time, geoid height and reflectivity (not corrected for atmospheric effects) from GLA06 Global Elevation Data product. Ancillary fields receiver gain, received pulse waveform and background noise mean value were extracted from GLA01 Global Altimetry Data Product. The GLAS field names are listed on Table 15.

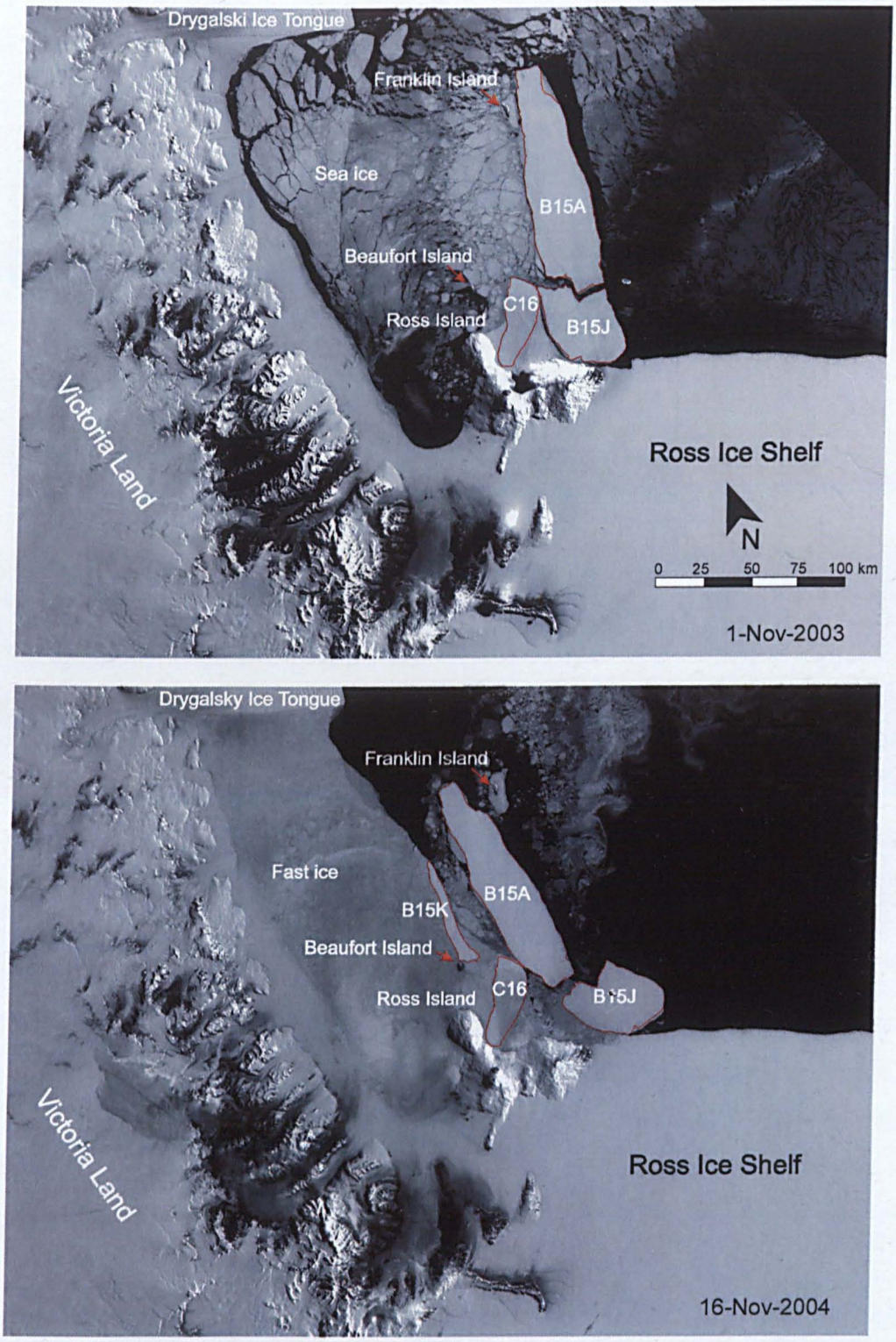

Figure 56 - MODIS visible satellite image [*Scambos et al.*, 2001] of icebergs B15A, B15J and C16 on the Southwest Ross Sea. Top: during Laser 2a and Bottom: after Laser 3a.

Table 15 - Fields extracted from GLAS files.

Field name	Description	GLAS product
i_rec_ndx	GLAS record index	GLA01, GLA06
i_UTCTime	Transmit time	GLA01, GLA06
i_gainSet1064	Receiver gain for 1064 nm laser	GLA01
i_4nsBgMean	Background mean value (noise)	GLA01
i_tx_wf	Sampled transmit pulse waveform	GLA01
i_RecNrgLast_EU	Received energy for 1064 nm laser	GLA06
i_lat	Shot latitude	GLA06
i_lon	Shot longitude	GLA06
i_elev	Surface elevation	GLA06
i_gdHt	Geoid height above ellipsoid	GLA06
i_reflctUncorr	Reflectivity not corrected for atmospheric effects	GLA06

GLAS accuracy is compromised by three factors: i) saturation from bright reflective surfaces; ii) forward scattering within clouds and iii) cloud absorption. Saturation is caused by the lower setting of the automatic gain being too high for high reflectance target, notably for ice targets. This results in an overestimate in range and thus an underestimate in elevation. Mild saturation can be corrected for using an empirical function provided by NASA [*Fricker et al.*, 2005]. If the received power is between 13.1 and 60 fJ the elevation, E, should be corrected by adding the following term,

$$\delta E = \frac{c\alpha}{2}(e - e_{sat}) \tag{6.1}$$

where c is the speed of light, α = 0.149 ns fJ^{-1} is an empirically derived corrective factor, e is the received energy and e_{sat} = 13.1 fJ is the energy saturation threshold. The received energy in GLA01 is incorrect due to due to errors in GLAS product generation, thus one has to recalculated it from the echo waveform:

$$e = \frac{0.1165}{k}\sum_{i=1}^{48}(w_i - \varepsilon) \tag{6.2}$$

k = 13 being the receiving gain, w_i the waveform counts for bin i, and ε the waveform background mean noise. When e>60 fJ the data was discarded. Figure 57 shows an example of a GLAS track with saturation over ice which was corrected for.

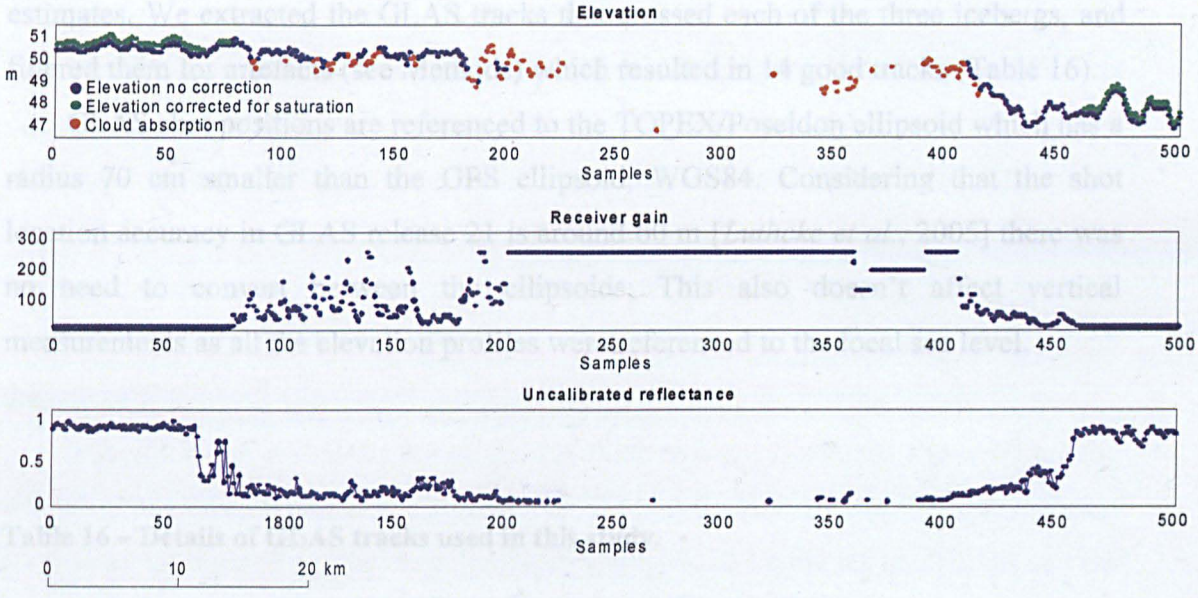

Figure 57 - GLAS profile from Laser 3a (23/10/2004 09:33:38 GMT) over the Ross Ice Shelf showing the effect of i) saturation and ii) cloud absorption. Saturation occurs at the very left and right of this section when the gain is at the minimum setting (13) and the reflectivity is almost 1. This was corrected for (see text) resulting in higher elevations. Cloud blocking, in the middle of the section, is identifiable by a very large receiver gain, abnormally low target reflectance and, in this case, missing data.

Forward scattering of the laser within clouds can cause a longer optical path with an attenuated echo. This leads to an overestimate in the elevation. Due to technical problems with the onboard lasers, there was a degradation of the laser's transmitted energy with time [*Abshire et al.*, 2005]. The first periods of Lasers 2 and 3, periods Laser 2a and Laser 3a, used in this study, were the least affected. Nevertheless, under some circumstances the laser is not powerful enough to penetrate the clouds (see Figure 57), but often it results in a faint echo with increased noise in the elevation estimate. At the moment GLAS products don't have reflectivity calibrated for atmospheric effects and don't correct for cloud forward scattering. As a filter for cloud covered areas, we eliminated all echoes with gain smaller than 50. Also, by inspecting other ancillary data fields from each track, we excluded data with a suspiciously low returned energy, namely reflectivity below 0.4 over glacial ice and below 0.2 over sea ice. The nature of the target was identified by the geographic position and elevation

estimates. We extracted the GLAS tracks that crossed each of the three icebergs, and filtered them for artefacts (see Methods) which resulted in 14 good tracks (Table 16).

GLAS shot positions are referenced to the TOPEX/Poseidon ellipsoid which has a radius 70 cm smaller than the GPS ellipsoid, WGS84. Considering that the shot location accuracy in GLAS release 21 is around 60 m [*Luthcke et al.*, 2005] there was no need to convert between the ellipsoids. This also doesn't affect vertical measurements as all the elevation profiles were referenced to the local sea level.

Table 16 – Details of GLAS tracks used in this study.

Laser	Iceberg	Date	Time
L2a	B15A	13-Oct-03	07:28:32
L2a	B15A	21-Oct-03	07:10:06
L2a	B15A	05-Nov-03	20:59:53
L2a	C16	12-Oct-03	21:55:14
L2a	C16	12-Oct-03	21:36:48
L2a	C16	30-Oct-03	07:01:24
L2a	C16	07-Nov-03	06:42:58
L2a	B15J	07-Nov-03	06:42:45
L3a	B15A	16-Oct-04	19:35:55
L3a	C16	08-Oct-04	10:21:07
L3a	C16	02-Nov-04	09:35:28
L3a	B15J	16-Oct-04	10:02:45
L3a	B15J	17-Oct-04	19:45:33
L3a	B15J	02-Nov-04	19:08:40

6.4 Iceberg profiles

Icebergs B15A and B15J split apart in October 2003 (see Figure 56) shortly before the beginning of Laser 2a. They were part of B15, a huge iceberg measuring 295 by 37 kilometres and the largest observed since the advent of satellite imagery. B15 had calved from the eastern side of the Ross Ice Shelf in March 2000. Iceberg C16 calved in September 2000 from the western side, close to Ross Island. Both icebergs have resided immediately east of Ross Island during the period of this study constrained by the ice shelf front, and the cirque formed by Ross, Beaufort and Franklin islands.

Vertical profiles of iceberg C16 reveal a strongly convex shape, varying from an altitude of 15 m on the ice front to 32 m in the middle (Figure 58 and Figure 59). This equates to a slope of up to 2.5 m km^{-1}, the highest observed in this study. This shape must have been formed prior to calving since at this southern latitude the summers are too cold for any significant surface runoff. Furthermore, on the eastern side of the Ross Ice Shelf, where C16 originated, comparable slopes in GLAS altimetry were observed. This is probably caused by the Ross Island acting as an obstruction to the ice shelf growth.

Icebergs B15A and B15J are thicker, with an average freeboard above 40 m, and show a comparably flatter shape with slopes of up to 0.4 m km^{-1}. On all three icebergs there is an asymmetry in thickness between what used to be the ice shelf front and the inland side. These are the eastern side for C16 and western sides for B15A and B15J, which have a lower freeboard as can be seen on Figure 59. This might be caused by stronger basal melting at the ice edge.

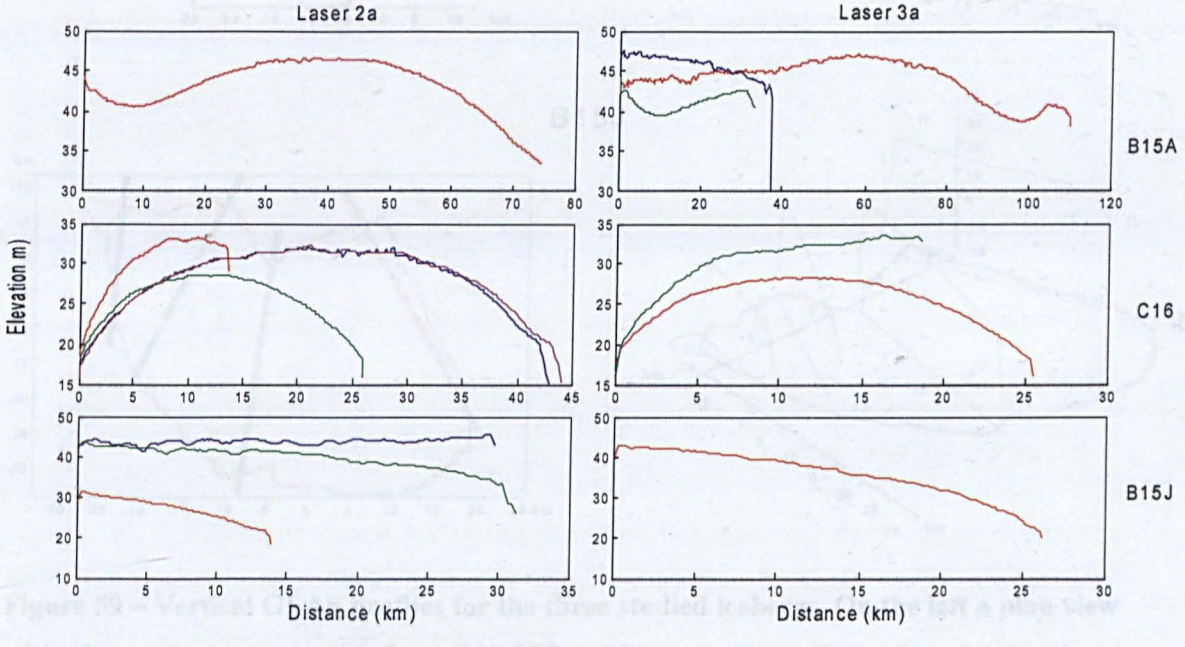

Figure 58 - Elevation profiles for icebergs B15A, C16 and B15J for the two laser periods considered. Different colours represent different GLAS tracks for the same icebergs.

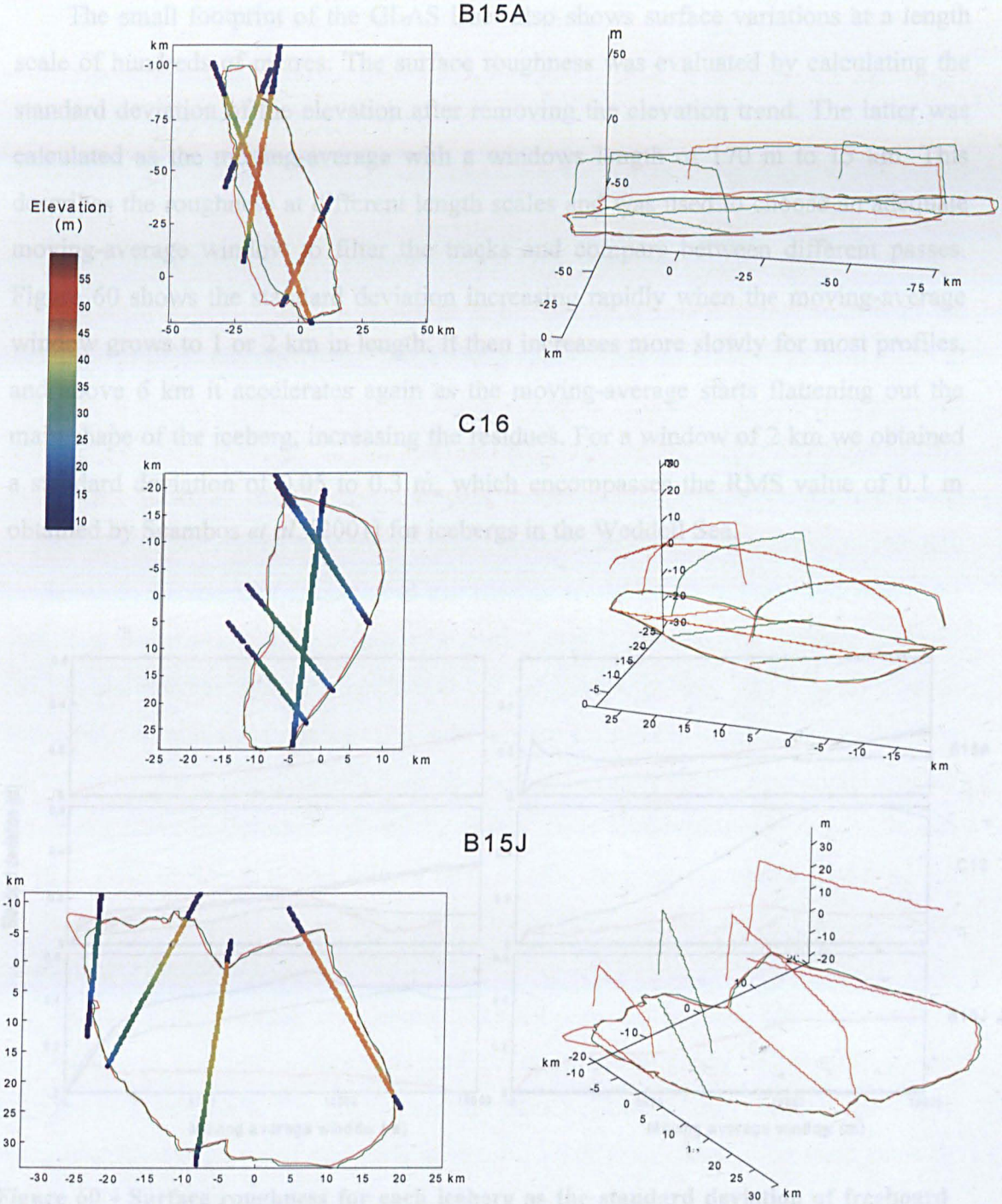

Figure 59 – Vertical GLAS profiles for the three studied icebergs. On the left a plan view with the contours extracted from MODIS satellite images and on the right a three dimensional projection with 4x vertical exaggeration. The red and green contours and profiles represent Laser 2a (2003) and 3a (2004), respectively.

The small footprint of the GLAS laser also shows surface variations at a length scale of hundreds of metres. The surface roughness was evaluated by calculating the standard deviation of the elevation after removing the elevation trend. The latter was calculated as the moving-average with a windows length of 170 m to 15 km. This describes the roughness at different length scales and was used to choose an adequate moving-average window to filter the tracks and compare between different passes. Figure 60 shows the standard deviation increasing rapidly when the moving-average window grows to 1 or 2 km in length. It then increases more slowly for most profiles, and above 6 km it accelerates again as the moving-average starts flattening out the main shape of the iceberg, increasing the residues. For a window of 2 km we obtained a standard deviation of 0.05 to 0.3 m, which encompasses the RMS value of 0.1 m obtained by Scambos *et al.* [2001] for icebergs in the Weddell Sea.

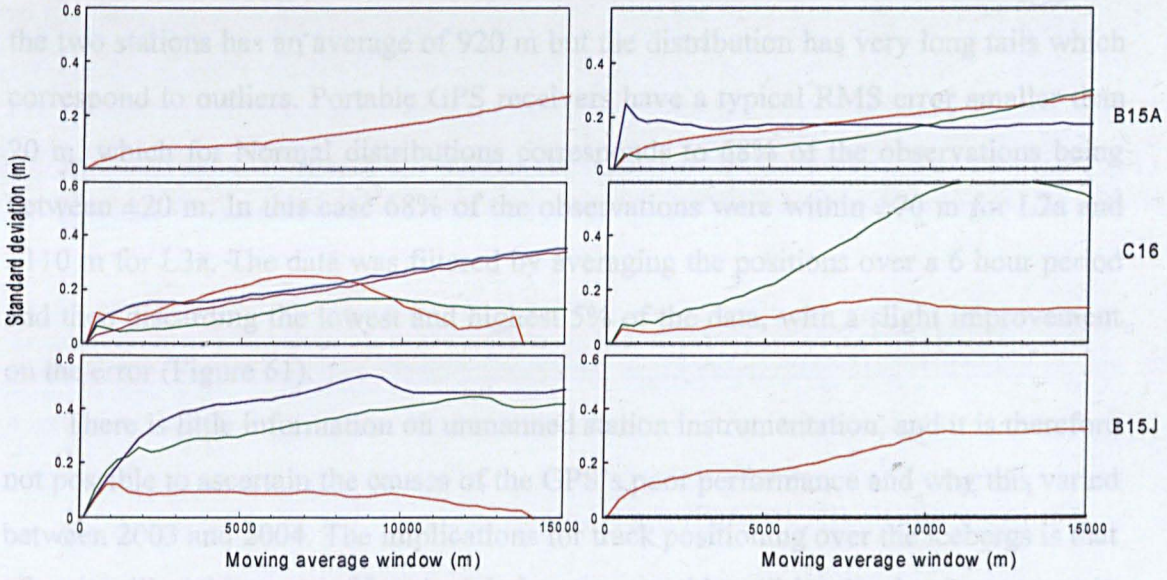

Figure 60 - Surface roughness for each iceberg as the standard deviation of freeboard after subtracting a moving-average of variable length. Different colours represent different GLAS tracks for the same icebergs.

6.4.1 Observed change in freeboard

The comparison between tracks acquired at different times relies on knowing a sufficiently accurate location over the iceberg when compared to the iceberg's surface roughness. The method used to locate the GLAS shots over an iceberg depends on the accuracy of: i) the knowledge of the GLAS shot location; ii) the iceberg contours extracted from MODIS images and iii) the GPS positions. GLAS release 21 has a horizontal accuracy of ±60 m [*Luthcke et al.*, 2005], which is comparable with the laser footprint of around 70 m. The iceberg contour has an error of at least ±125 m resulting from the MODIS image resolution of 250 m. In order to assess GPS accuracy we compared the positions of two stations placed on iceberg B15J. Although iceberg B15J was moving, the distance between both stations should be constant, and assuming that both GPSs generate bivariate independent Gaussian noise with standard deviation σ, the standard deviation of the distance would be $\sqrt{2}\,\sigma$. Figure 61 shows the statistical distribution of the distance for both Laser 2a and 3a. The distance between the two stations has an average of 920 m but the distribution has very long tails which correspond to outliers. Portable GPS receivers have a typical RMS error smaller than 20 m, which for Normal distributions corresponds to 68% of the observations being between ±20 m. In this case 68% of the observations were within ±70 m for L2a and ±110 m for L3a. The data was filtered by averaging the positions over a 6 hour period and then discarding the lowest and highest 5% of the data, with a slight improvement on the error (Figure 61).

There is little information on unmanned station instrumentation, and it is therefore not possible to ascertain the causes of the GPS's poor performance and why this varied between 2003 and 2004. The implications for track positioning over the icebergs is that often it will yield errors of hundreds of metres, so this will be the dominant error in horizontal positioning. Considering the relatively high elevation RMS values over the iceberg and the relatively large slope, mainly on C16, this will limit the results.

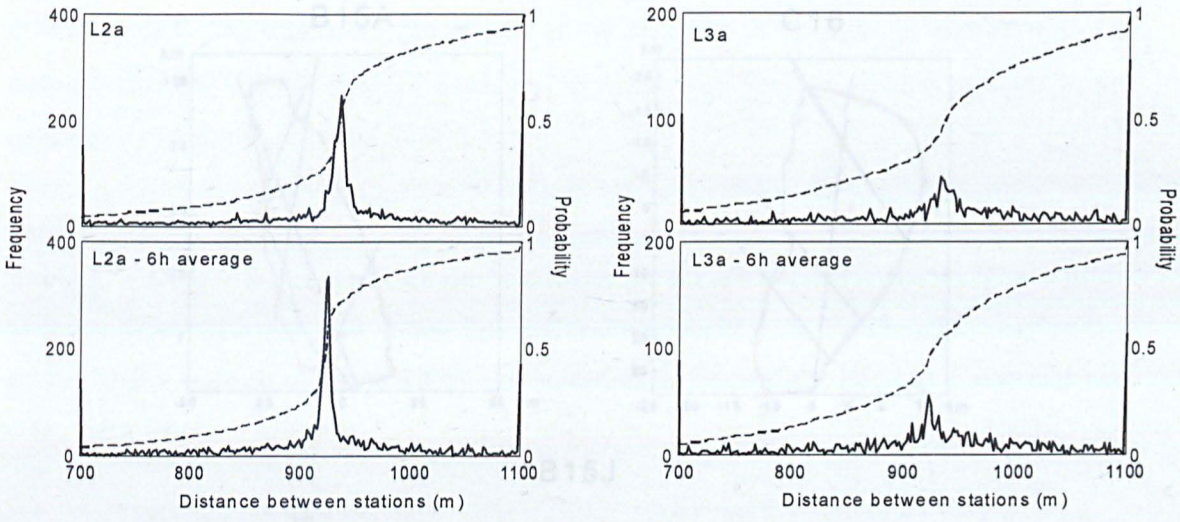

Figure 61 - Empirical distribution and cumulative distribution function (dashed line) of the distance between the two GPS stations on the iceberg B15J. The two lower graphs were calculated after filtering the position data. This consisted in averaging it for a period of 6 hours around the observation time and excluding the highest and lowest 5% of the data.

The 14 tracks produced 12 crossover points, 6 of which were between tracks one year apart (Figure 62). The results of the crossover analysis is presented in Table 17. The differences in elevation for crossovers from the same laser period varies between -0.63 and 0.52 m, while one would expect little or no variation in height. This indicates a freeboard measurement error of at least ±0.6 m; by taking into account an average ice density of 850 km m^{-3} this results in a iceberg thickness error of ±4.0 m. Differences for crossovers between L2a and L3a vary between -0.18 and 0.66 m therefore not being able to detect iceberg thinning. Averaging the GLAS track to remove the surface roughness does not improve the results. Crossovers from the same period show a large variation due to error in the referencing to local sea level and errors in horizontal referencing on iceberg. Another possible source of error is the variation in the elevation of iceberg, either through accumulation or wind drift.

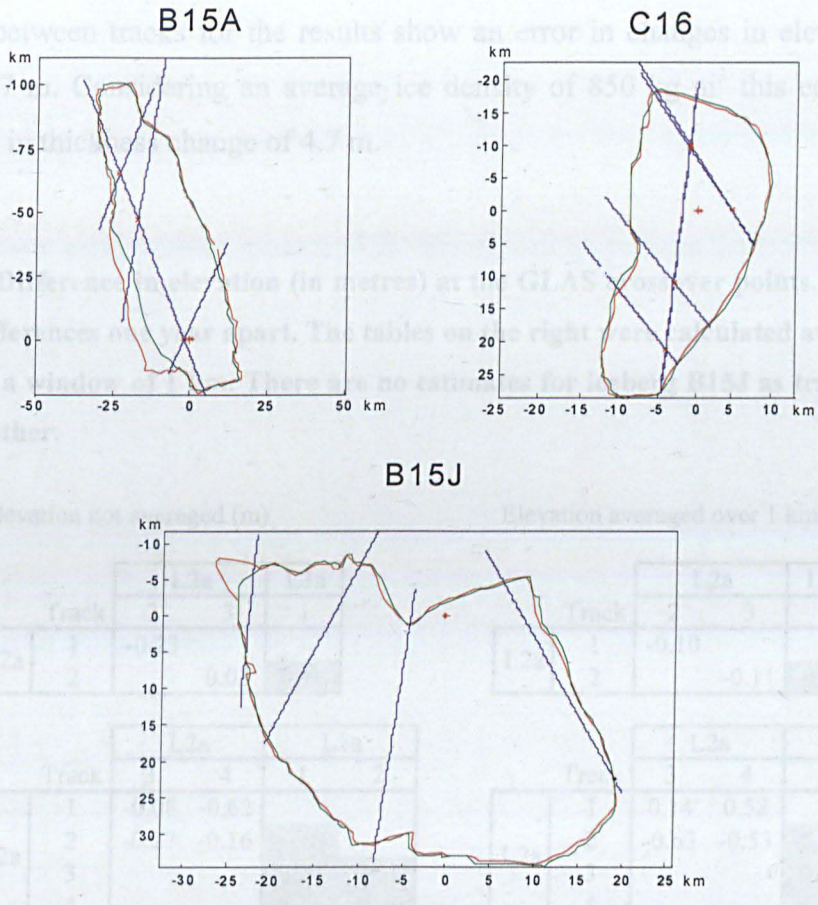

Figure 62 - Location of track crossover points (red cross) and GPS stations (red star) over the icebergs. There were no track interceptions on iceberg B5J.

Referencing the track to the local sea level is prone to errors due to the presence of sea ice, which will cause the elevation to be overestimated, and increased elevation variability over the sea. Scambos and colleagues evaluated their elevation measurements over icebergs to have an error of ±0.2 to ± 0.5 m. These authors dispensed with GPS data and used a large repository of MODIS images to position the icebergs. Moreover, their study was done in the Weddell Sea, at higher latitudes where less sea ice is present. This would have alleviated the errors in local referencing. If one assumes that the horizontal referencing won't induce more errors, then the error in a change of elevation between two profiles is the sum for each measurement's error, or from 0.4 to 1.0 m.

In the present study there are six crossovers between tracks from laser period L2a. The crossovers between tracks for the same GLAS period In the present study, the

crossover between tracks for the results show an error in changes in elevation to be around ±0.7 m. Considering an average ice density of 850 kg m^3 this equates to an uncertainty in thickness change of 4.7 m.

Table 17 – Difference in elevation (in metres) at the GLAS crossover points. The cells in grey are differences one year apart. The tables on the right were calculated averaging the tracks with a window of 1 km. There are no estimates for iceberg B15J as tracks did not cross each other.

Elevation not averaged (m)

B15A

		L2a		L3a
	Track	2	3	1
L2a	1	-0.23		
	2		0.03	**0.16**

C16

		L2a		L3a	
	Track	3	4	1	2
L2a	1	-0.08	-0.62		
	2	-0.27	-0.16	-0.03	
	3			0.26	0.01
	4			0.16	-0.10

Mean = **0.06**

Elevation averaged over 1 km (m)

		L2a		L3a
	Track	2	3	1
L2a	1	-0.10		
	2		-0.11	**0.41**

		L2a		L3a	
	Track	3	4	1	2
L2a	1	0.14	0.52		
	2	-0.63	-0.53	-0.04	
	3			0.66	-0.18
	4			0.51	-0.13

Mean = **0.16**

Kwok *et al.*'s [2004] study of sea ice in the Artic also referenced elevation to the local sea level measured at the sea ice leads. In their study the dry winter (March 2003) atmosphere over the Arctic provided ideal conditions for the cloud challenged GLAS instrument. The excellent conditions are demonstrated by values of RMS elevation of around 2 cm over very flat surfaces. The cloud cover in coastal Antarctica, such as around the Ross Sea, are in itself a limiting factor for the accuracy required.

The change in iceberg freeboard is due to several factors, the most important at this latitude being surface accumulation, M_s, basal melting, M_b, and ice flow divergence within the iceberg, $M\nabla \cdot \upsilon$:

$$\frac{\partial h}{\partial t} = \left(1 - \frac{\rho_i}{\rho_w}\right)\left(M_s + M_b + M\nabla \cdot \upsilon\right) \tag{6.3}$$

where ρ_i and ρ_w are the densities of ice and water respectively. Net accumulation on iceberg B15 during this period was negligible according to field observations at the unmanned stations (Y. Kim, personal communication). Strain thinning, causing an ice-

shelf like spreading, was modelled by Jansen and colleagues [2005]. Simulations for a typical 250 m thick iceberg, in very cold waters and with an internal temperature of -15°C resulted in vertical reduction of 1 m a^{-1}. Basal melting at high latitudes is quite small and thus comparable to strain thinning, but becomes much more important as the iceberg moves into warmer waters. The accumulation was neglected and a strain thinning of 1 m a^{-1} assumed. The error in the present measurement set a maximum basal melting of 3.7 m a^{-1}.

Table 18 – Observations of iceberg thinning and simulations of basal melting. The simulations were based on observed iceberg tracks with daily frequency. These were also resampled every 9 and 30 days to test the sensitivity of the estimates.

Source	Iceberg	Period	Location	Thickness change (m a^{-1})	Simulated basal change (m a^{-1})		
					1 day	9 days	30 days
[Frezzotti *et al.*, 1998]	Several (see text)	1973-1989	67°S	-12	-5.2	-5.2	-5.2
[Scambos *et al.*, 2005]	A38A	2/2003-10/2003	63°S-57°S	-19.3 ±9.7	-71.0	-52.2	-37.8
	A38B	3/2003-3/2004	63°S-54°S	-32.3 ±5.2	-72.3	-53.8	-39.6
	A43A	3/2003-9/2003		-10.1 ±5.0	-6.8	-5.05	-4.12
	A43A	3/2003-3/2004		-7.4 ±2.7	-8.38	-6.48	-5.6
This study	B15A	10/2003-10/2004	77°S	+0.6 ± 4.7	-0.9	-0.8	-0.7
	B15J			no crossovers	-4.1	-2.9	-2.5
	C16			+0.4 ± 4.7	-0.9	-0.9	-0.9

6.5 Basal melting simulations

Three sources of iceberg thinning observations, including the present study, were compiled and compared these with simulations of basal melting (Table 18). As seen in the last section, this is the most important thinning process for the Southern Ocean. The method consists in using the Holland and Jenkins [1999] three equation model for ice shelf basal melting and forcing it with climatological forcing fields for ocean salinity, temperature and water velocity. We used observed iceberg tracks from the freely available Brigham Young University's (BYU) iceberg database [*Long et al.*,

2002], which have higher temporal frequency than the National Ice Centre observations. The method is the same used in Chapter 5 also published as [*Silva et al.*, 2006], except that here we used the BYU tracks resampled daily, every 9 days and every 30 days, to test the sensitivity to the track's temporal frequency. Frezzotti *et al.*'s [1998] estimate is an average for multiple points measured at the Ninnis Glacier Tongue and two icebergs that resided along George V Coast in the period 1973-1989. To simulate the basal melting for this situation an iceberg of 250 m in thickness was assumed, fixed at 148°E, 67°S, for a period of four years. The measurements and simulation results are in Table 18.

Both observations and modelling agree in the general pattern of a strong increase in melting as icebergs move north into warmer waters. In the Southern Ross Sea the simulation results of around 1 m a^{-1} fit within the imperfect observations, even if we add 1 m a^{-1} for strain thinning. There is also agreement with the measurements for iceberg A43 melting at a faster rate in the southern Weddell Sea. For the faster melting icebergs in the Weddell Sea the simulations overestimate the melting. This is probably caused by two factors. The presence of such a large object in the sea is likely to affect the local ocean circulation, which the simple approach followed here disregards. For instance the surface drag might reduce the relative water velocity leading to smaller basal melting rates than predicted. Even more importantly, the estimates are largely influenced by the temporal frequency of the iceberg positions. Iceberg tracks with daily positions describe the influence of short term and mesoscale processes forcing the icebergs, such as storms, ocean eddies and even tides. Because the ocean fields are climatological and of relatively low resolution, the velocity of the water at the bottom of the iceberg will be overestimated, resulting in a large basal melting. Even a 9 day sampling, similar to the temporal frequency of the National Ice Center used in Chapter 5 overestimates the melting. The 30 day undersampling gives the best results.

Iceberg A38A had a smaller average melting rate than A38B, although the uncertainty intervals overlap. These icebergs were of similar thickness, and followed similar trajectories both in space and time (Figure 63). Iceberg A38B moved sooner into warmer waters, melting faster. But this is balanced by the fact that this iceberg was profiled the second time 5 months later than A38A during which it passes South Georgia to the south and drifts into slower and cooler waters.

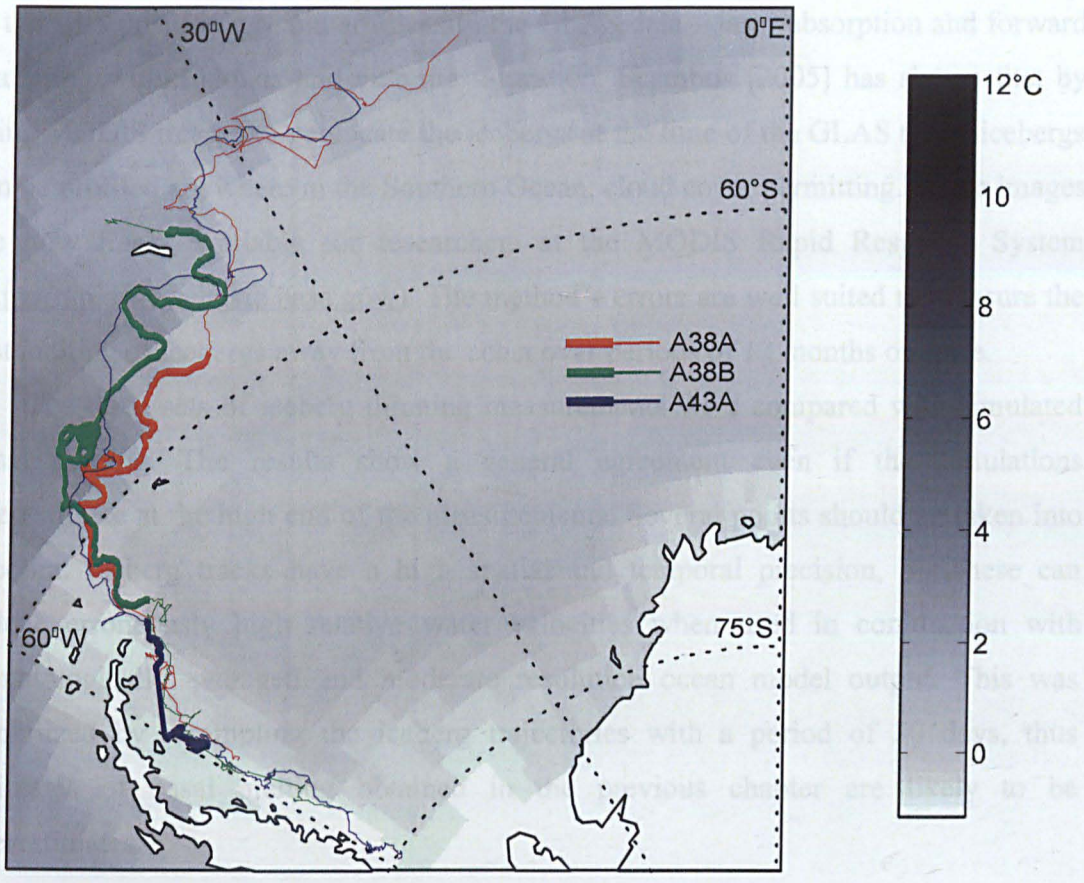

Figure 63 - Trajectories of icebergs A38A, A38B and A43A in the Weddell Sea from the Brigham Young University iceberg database [*Long et al.*, 2002]. The thin line represents the full recorded trajectory and the thick line marks the period in between the GLAS measuments. Iceberg A38B got stranded close to South Georgia where eventually it disintegrated.

6.6 Conclusions

The recent appearance of GLAS data and the demonstration of its use for the measurement of sea ice freeboard in the Arctic [*Kwok et al.*, 2004] triggered this attempt at measuring iceberg thinning. Icebergs B15A, B15J and C16 were selected due to the existence of GPS data to reference the altimetry tracks. The measured reduction in freeboard of +0.6±4.7 m and +0.4±4.7 m for icebergs B15A and C16 respectively, were overwhelmed by the uncertainty in the measurements. The sources of error were from both the positioning of the tracks over the iceberg (from incertainty

in the GPS positioning) and artefacts in the GLAS data – laser absorption and forward scattering within clouds and extreme saturation. Scambos [2005] has shown that by using MODIS images to geolocate the icebergs at the time of the GLAS track, icebergs can be profiled anywhere in the Southern Ocean, cloud cover permitting. These images are now freely available for researchers at the MODIS Rapid Response System (http://rapidfire.sci.gsfc.nasa.gov/). The method's errors are well suited to measure the fast melting of icebergs away from the coast over periods of 12 months or more.

The three sets of iceberg thinning measurements were compared with simulated basal melting. The results show a general agreement even if the simulations overestimate at the high end of the measurements. Several points should be taken into account. Iceberg tracks have a high spatial and temporal precision, but these can induce erroneously high relative water velocities when used in conjunction with climatologically averaged and moderate resolution ocean model output. This was minimized by resampling the iceberg trajectories with a period of 30 days, thus estimates of basal melting obtained in the previous chapter are likely to be overestimates.

Chapter 7 Discussion and conclusions

7.1 Discussion

The results presented in this thesis have received specific discussion in each chapter. However there are more general questions that cover several chapters and will have here an overarching discussion.

The present study has demonstrated that the input of iceberg meltwater to the ocean can be estimated using a combination of iceberg observations and modelling of iceberg basal melting. SAR images were used to map the distribution of icebergs around coastal Antarctica and in the southern half of the Weddell Sea, and to perform four measurements of the flux of icebergs along the coast (see Chapter 4). This first map of iceberg distribution around the Antarctic coast was used to study the distribution of iceberg density, proportion of grounded icebergs in coastal areas and, for the first time, to study the iceberg size distribution of a population of icebergs from 125 m long to giant icebergs. By taking into account the ice volume transported by each iceberg size class, instead of only the frequency distribution, the importance of large icebergs become evident. In the area covered by both SAR mosaics – a 200 km coastal strip and the Southern half of the Weddell Sea – the icebergs above 10 km^2 account for 70% of the total mass and giant icebergs (above 100 km^2) for over 50% of the floating ice mass. However, if the whole Southern Ocean had been considered the importance of large icebergs might have been smaller. Larger icebergs tend to stay closer to the coast than smaller ones, because they have a larger volume in relation to their surface, which means that the Coriolis force has a larger role compared with the current and wind drag that operates on the surfaces of the iceberg. For icebergs moving westwards along the coast, the Coriolis force points inland, keeping the iceberg in the Coastal current.

It is not yet possible to describe the average iceberg meltwater injection in the Southern Ocean as the SAR image coverage used here only covers the southernmost 200 km along most of the coast. Also, the instantaneous meltwater injection form several periods should be averaged to deal with the large temporal variability in

iceberg density that, at least partially, results from a heterogeneous spatial distribution. Therefore, in Chapter 4 we recommended a more complete mapping of iceberg distribution in the Southern Ocean south of the polar front, for several different periods.

The approach used in Chapter 5 to characterise the average iceberg meltwater distribution was to combine observed tracks and sizes of giant icebergs with modelling of melting processes and simulate the spreading of meltwater along its trajectories. The resulting meltwater from giant icebergs was combined with a climatological estimate of meltwater injection from the modelling of an iceberg model for icebergs up to 2 km in length [*Gladstone*, 2001; *Gladstone et al.*, 2001]. In this way this meltwater distribution takes into account both small and giant icebergs and can be used to test the sensitivity of ocean circulation models to a spatially and temporally variable forcing of iceberg freshwater.

This approach present several shortcomings. The NIC giant berg database has discontinuities in the tracks and size measurements which results in distortions in the trajectories and amount of water resulting from horizontal size reduction. Also, the volume of water resulting from an observed reduction in horizontal size is spread over the trajectory of the giant iceberg, while in reality some of this volume will form smaller icebergs which will have different drift patterns, and possibly longer longevities. A third problem is that when giant icebergs are too small to be tracked the corresponding water volume is accounted for as having the same distribution pattern as the modelled icebergs, which calved from the coast. This overestimates the amount of meltwater that is released to the ocean close to the coast.

The calving of icebergs is the largest output terms in the equation of the Antarctic mass balance [*IPCC*, 2001] and also carries the largest uncertainty, 33 %, which translates into an ambiguity in the net balance. Gladstone [2001] observed in both SAR images and iceberg trajectory simulations that the majority of calved icebergs were carried along the narrow, counter-clockwise, Antarctic Coastal Current. He then proposed the analysis of long time-series of SAR images to estimate and monitor the calving flux of the Antarctic Ice sheet, and through it improve the knowledge of the Antarctic mass balance. This was originally one of the motivations for this thesis but was superseded due to advances in the application of satellite remote sensing in

glaciology. Studies of the components of mass balance[3] now rely on SAR interferometry [*Rignot et al.*, 2004], speckle tracking [*Rignot*, 2002] and feature tracking [*Frezzotti et al.*, 2000] over glaciers and ice streams to measure the ice velocity. These, combined with the knowledge the ice sheet thickness allow estimates of ice volume losses. It can be applied to measure fluxes over calving front or, more frequently, over the grounding line.

In Chapter 4 the error in measuring iceberg basal area was estimated as 15%, but the measurement of the velocity of a continuous volume of ice is intrinsically more accurate than mapping thousands of irregular shaped icebergs of different thicknesses and ages spread across a very large area. Both methods depend on accurate estimates of ice thickness and density. This can be measured for very large icebergs, as was done on Chapter 5, but can only be estimated using an empirical relationship for the majority of floating iceberg mass. In ice flux studies it is feasible to measure this for the majority of large glaciers and ice streams [*Jacka et al.*, 2004]. The flux method also makes it easier to observe temporal variations in the calving flux and to attribute changes to a specific drainage basin. This is particularly important as different trends have been observed on the East and West Antarctic ice sheets [*Rignot and Thomas*, 2002] and also at the drainage basin scale [*Davis et al.*, 2005; *Payne et al.*, 2004]. Another advantage of the flux method is that it can also be used to measure basal melting of glacier tongues and ice shelves which is the second largest mass loss term in Antarctica [*Jacobs et al.*, 1996]. When the melting and thus the configuration of the ice are in steady state, the volume of basal melting can determined by subtracting the volume flux at the grounding line by volume flux at the calving front [e.g. *Jenkins et al.*, 1997].

Our motivation for the four iceberg flux measurements was, ultimately, to allow for an assessment of meltwater on the ocean and not for mass balance calculations. It was used to confirm the large percentage of grounded icebergs and to measure iceberg trajectories and speeds in the Eastern Weddell during summer and winter. The high sampling requirements for this technique, due to variability in iceberg density and the

[3] Component or flux studies of ice sheet mass balance measure the different input and output fluxes, often at the basin level, as opposed to the integrated approach where the variations of the ice sheet volume are measured from changes in surface elevation, correcting for the movement of the underlying bed and firn compaction [Jacka *et al.* 2004].

need for frequent tracking, limits its usefulness. That led us to propose the use of newly available satellite imaging products to extend the tracking of giant icebergs to multi-kilometre scale icebergs and thus to account for up to 70% of the volume of the total iceberg population, greatly improving its usefulness in describing iceberg dynamics and erosion. The mapping of the static distribution of icebergs, as done for the two mosaics, complements this approach by providing information on smaller icebergs.

In order to better understand the impact of icebergs on the ocean, the knowledge of where and how much meltwater is entering the ocean should be accompanied by a good understanding of how the meltwater mixes with the ocean water. In this section we will start by presenting a summary of theoretical work done in the area, including laboratory studies. This is followed by a review of oceanographic observations around icebergs and, finally, an assessment of existing gaps in the literature that we see as limiting to the study of interaction of icebergs with the ocean.

Iceberg melting affects the climate system through heat and buoyancy fluxes at the ice-water boundary and a flux of mass, and therefore momentum, into the ocean. Estimates of the volume and distribution of iceberg meltwater must be complemented by a good understanding of the flow pattern around the ice as these will determine the properties of the mixture of meltwater and ambient water and the heat and salt fluxes to the ocean and atmospheric boundary layer. For instance Jenkins [1999] studied the melting of icebergs in the Southern Ocean and predicted that icebergs melting off the continental shelf could have two different and opposing effects on the vertical heat and flux of nearby water, depending on the depth at which the meltwater was released. Off the continental shelf the Antarctic Surface Water (AASW) is under laid by the relatively warm and salty Circumpolar Deep Water. Meltwater mixing with the surface water results in the predictable cooling and freshening of the ocean surface, but an iceberg deep enough to reach below the pycnocline can melt and mix turbulently with CDW which would then be fresh enough to upwell and carrying warmth vertically. The knowledge of the final properties of the meltwater mixture and how this is spread in the ocean are fundamental to quantitatively study its impacts on the ocean.

7.2 - Conclusions

The main contributions of this PhD project are the following:

1- Computer-based algorithm for the detection and tracking of icebergs

A new computer-based algorithm for the detection and tracking of icebergs on SAR images was proposed in Chapter 3 [*Silva and Bigg*, 2005]. This method allows the processing of large volumes of images efficiently and in a systematic way, reducing the variability of the human operator. It was tested on ERS PRI/Envisat IMP 25 m resolution images (Chapter 3) and Envisat Wide Swath 150 m resolution images (Chapter 4). The accuracy when applied to 25 m images was assessed against manual classification, and performed at least as well than a previously published iceberg detection method [*Williams et al.*, 1999], but producing less false alarms. This is the first iceberg detection algorithm that allows the detection to take place at close to the SAR image's maximum resolution (not to be confused with the pixel distance) which allows the shape to be extracted and tracked across a time series of images.

Wide Swath (WS) images have a coverage 16 times larger than that of PRI images, and as such are particularly suitable for monitoring studies. This is the first algorithm proposed to work on WS images. The accuracy on WS images was tested against manual classifications on high resolution images to define a size detectability curve. It was also validated against manual classifications on SAR images, verified by ship-based observations that we obtained during a short field campaign in the Weddell Sea. The algorithm is also the first of its kind to be tested for this imagery type which shows great advantages for iceberg monitoring.

2-Coastal distribution of icebergs around Antarctica

The RAMP mosaic of SAR images was used to map iceberg distribution on a coastal strip of around 200 km around Antarctica (Chapter 4). A second mosaic extending the coverage on the Weddell Sea was also produced. The coastal area,

despite constituting only 15 % of the Southern Ocean, accumulates an iceberg volume 3 times the annual calving flux of the continent. Analysis of bathymetry data, which was supported by iceberg tracking, predicts that up to 40 % of icebergs in this area are grounded, leading to longer longevities. Two iceberg size classes prevail in terms of total ice volume carried: multi-decakilometric and kilometric icebergs. The average nearest-neighbour distance between free floating icebergs is 3278 m, or around half the distance expected for randomly distributed icebergs. This shows a highly clustered distribution which raises the sampling requirements of monitoring studies. The iceberg maps derived are not yet sufficient to establish a climatology for the Southern Ocean, so recommendations are made for a two way complementary iceberg monitoring strategy: mapping of iceberg distribution for the whole Southern Ocean south of the Polar Front, for several different periods, and extension of the existing databases of iceberg tracks to include multi-kilometric icebergs. This last point could be achieved by using daily coverage, 1 km resolution, Envisat Global Monitoring Mode images, that have been archived since 2004.

3-Map of iceberg meltwater distribution in the Southern Ocean

The first map of the iceberg meltwater distribution in the Southern Ocean including giant icebergs was presented in Chapter 5 [*Silva et al.*, 2006]. This can now be used to test the sensitivity of ocean circulation models to a more realistic iceberg meltwater forcing. Observed tracks and sizes of giant icebergs from the period 1986-2003 were combined with the output of an ocean circulation model and atmospheric reanalysis data to model the melting and spreading of iceberg meltwater. The meltwater contribution of smaller icebergs is described by a simulation of iceberg drift and decay [*Gladstone*, 2001; *Gladstone et al.*, 2001]. The iceberg meltwater was shown to be comparable in magnitude with other components of the freshwater flux for the Weddell Sea and for the Southern Ocean south of the Polar Front, thus meriting inclusion in climate studies and simulations. Also, we observed a large spatial and temporal variation in the meltwater injection caused by giant icebergs which indicates that the impact of melting can be even more important locally.

4-Assessment of measuring iceberg thinning using laser altimetry

We measured the profiles and changes to the freeboard of 3 giant icebergs in the southern Ross Sea using GLAS satellite-borne laser altimetry (Chapter 6). The existence of GPS stations on the icebergs allowed referencing of GLAS tracks on the icebergs, and through this an analysis of track crossover points yielded the variation in iceberg thickness. The uncertainty carried by the GPS data and artefacts in GLAS altimetry were large when compared with the small reductions in freeboard caused by basal melting and severely reduced the precision of the measurements. For the present release of GLAS data the method is limited to measuring large differences in freeboard by comparing tracks more than one year apart of icebergs melting faster in warmer waters as done by Scambos *et al.* [2005]. Using the present measurements and other published observations we compared with simulations of basal melting. Simulations tended to overestimate melting for warmer waters and better results were obtained by resampling the iceberg trajectories with a period of 30 days. These results can be used to refine the meltwater estimation procedure used in Chapter 5.

A next step towards describing a climatology of iceberg distribution and movement in the Southern Ocean can be pursued by following the recommendations for iceberg monitoring made in section 4.6. This would be fully observational, while the present meltwater estimate relies partially on simulation tracks of small icebergs.

Advances in defining an iceberg climatology should be accompanied by progress in the effect of icebergs on the ocean. Detailed field observations, preferably around giant icebergs and in areas with non-negligible basal melting, should be undertaken to measure changes to the surrounding waters. Of particular importance to parameterise ocean circulation models is the presence and spatial extent of layers of meltwater mixture. The vertical distribution of these changes will define any iceberg induced heat flux at the surface.

References

Abshire, J.B., X. Sun, H. Riris, J.M. Sirota, J.F. McGarry, S. Palm, D. Yi, and P. Liiva, Geoscience Laser Altimeter System (GLAS) on the ICESat Mission: On-orbit measurement performance, *Geophysical Research Letters, 32* (21), 2005.

Ainley, D.G., and S.S. Jacobs, Sea-Bird Affinities for Ocean and Ice Boundaries in the Antarctic, *Deep-Sea Research Part a-Oceanographic Research Papers, 28* (10), 1173-1185, 1981.

Arrigo, K.R., G.L. van Dijken, D.G. Ainley, M.A. Fahnestock, and T. Markus, Ecological impact of a large Antarctic iceberg, *Geophysical Research Letters, 29* (7), art. no.-1104, 2002.

Bakayev, V.G., Soviet Antarctic Expedition Atlas of Antarctica, Administration of Geodesy and Cartography, Moscow, 1966.

Bamber, J.L., and R.A. Bindschadler, An improved elevation dataset for climate and ice-sheet modelling: validation with satellite imagery, *Ann. Glaciol., 25*, 439-444, 1997.

Bangham, J.A., R. Harvey, P.D. Ling, and R.V. Aldridge, Morphological scale-space preserving transforms in many dimensions, *Journal of Electronic Imaging, 5* (3), 283-299, 1996.

Beckmann, A., and H. Goosse, A parameterization of ice shelf-ocean interaction for climate models, *Ocean Modelling, 5* (2), 157-170, 2003.

Beucher, S., and C. Lantuejoul, Use of watersheds in contour detection, in *International Workshop on image processing, real-time edge and motion detection/estimation*, Rennes, France, 1978.

Bigg, G.R., M.R. Wadley, D.P. Stevens, and J.A. Johnson, Modelling the dynamics and thermodynamics of icebergs, *Cold Regions Science and Technology, 26* (2), 113-135, 1997.

Davis, C.H., Y. Li, J.R. McConnell, M.M. Frey, and E. Hanna, Snowfall-Driven Growth in East Antarctica Ice Sheet Mitigates Recent Sea-Level Rise, *Science*, 2005.

Davis, L.S., A Survey of Edge Detection Techniques, *Computer Graphics and Image Processing, 12*, 248-270, 1975.

de Cuevas, B.A., D.J. Webb, A.C. Coward, C. Richmond, S,, and E. Rourke, The UK Ocean Circulation and Advanced Modelling Project (OCCAM), in *High Performance Computing, Proceedings of HPCI Conference 1998*, edited by R.J. Allan, M.F. Guest, A.D. Simpson, D.S. Henty, and D.A. Nicole, pp. 325-335, Plenum Press, Manchester, 1999.

Drinkwater, M.R., Satellite Microwave Radar Observations of the Antarctic Sea Ice, in *Analysis of SAR Data of the Polar Oceans*, edited by C. Tsatsoulis, and R. Kwok, pp. 250, Springer-Verlag, Berlin and Heidelberg, 1997.

Fjørtoft, R., Segmentation d'images radar par detections de contours, PhD thesis, Institut National Polytechnique de Toulouse, 1999a.

Fjørtoft, R., Segmentation of {SAR} Images by Edge Detection: Strategy, Optimization and Implementation, in *Proc. Norwegian Signal Processing Symposium (NORSIG'99)*, pp. 70--75, Asker, Norway, 1999b.

Fjørtoft, R., P. Marthon, and A. Lopès, Multiresolution Edge Detection in SAR Images, in *Proc. Norwegian Signal Processing Symposium (NORSIG'97)*, pp. 6-10, Tromsø, Norway, 1997.

Foldvik, A., and T. Kvinge, Conditional stability of sea water at the freezing point, *Deep-Sea Research, 21*, 169-174, 1974.

Frezzotti, M., A. Cimbelli, and J.G. Ferrigno, Ice-front change and iceberg behaviour along Oates and George V Coasts, Antarctica, 1912-96, *Ann. Glaciol., 27*, 643-650, 1998.

Frezzotti, M., I.E. Tabacco, and A. Zirizzotti, Ice discharge of eastern Dome C drainage area, Antarctica, determined from airborne radar survey and satellite image analysis, *Journal of Glaciology, 46* (153), 253-264, 2000.

Fricker, H.A., A. Borsa, B. Minster, C. Carabajal, K. Quinn, and B. Bills, Assessment of ICESat performance at the Salar de Uyuni, Bolivia, *Geophysical Research Letters, 32* (21), 2005.

Fricker, H.A., N.W. Young, I. Allison, and R. Coleman, Iceberg calving from the Amery Ice Shelf, East Antarctica, in *Annals of Glaciology, Vol 34, 2002*, pp. 241-246, Int. Glaciological Soc., Cambridge, 2002.

Gill, A.E., Circulation and bottom water production in the Weddell Sea, *Deep-Sea Research, 20*, 111-140, 1973.

Gill, R.S., Operational Detection of Sea Ice Edges and Icebergs Using SAR, *Canadian Journal of Remote Sensing, 27* (5), 411-432, 2001.

Gladstone, R., A Modelling and Remote Sensing Study of Antarctic Icebergs, PhD thesis, University of East Anglia, Norwich, 2001.

Gladstone, R., and G.R. Bigg, Satellite tracking of icebergs in the Weddell Sea, *Antarctic Science, 14* (3), 278-287, 2002.

Gladstone, R.M., G.R. Bigg, and K.W. Nicholls, Iceberg trajectory modeling and meltwater injection in the Southern Ocean, *Journal of Geophysical Research-Oceans, 106* (C9), 19903-19915, 2001.

Grimaud, M., A New Measure of Contrast - the Dynamics, in *Image Algebra and Morphological Image Processing Iii*, pp. 292-305, SPIE - INT SOC OPTICAL ENGINEERING, Bellingham, 1992.

Grosfeld, K., M. Schroder, E. Fahrbach, R. Gerdes, and A. Mackensen, How iceberg calving and grounding change the circulation and hydrography in the Filchner Ice Shelf-Ocean System, *Journal of Geophysical Research-Oceans, 106* (C5), 9039-9055, 2001.

Hamley, T.C., and W.F. Budd, Antarctic Iceberg Distribution and Dissolution, *Journal of Glaciology, 32* (111), 242-251, 1986.

Harms, S., E. Fahrbach, and V.H. Strass, Sea ice transports in the Weddell Sea, *Journal of Geophysical Research-Oceans, 106* (C5), 9057-9073, 2001.

Haykin, S., E. Lewis, R. Raney, and J. Rossiter, *Remote Sensing of Sea Ice and Icebergs*, 686 pp., Wiley, John & Sons, 1994.

Hellmer, H., and A. Beckmann, The influence of ice shelves on the Weddell Sea. Filchner-Ronne Iche Shelf Programme Rep. 12, Alfred-Wegner-Inst. for Pol. and Mar. Res., Bremerhaven, Germany, 1998.

Hellmer, H.H., Impact of Antarctic ice shelf basal melting on sea ice and deep ocean properties, *Geophysical Research Letters, 31* (10), art. no.-L10307, 2004.

Holland, D.M., and A. Jenkins, Modeling thermodynamic ice-ocean interactions at the base of an ice shelf, *Journal of Physical Oceanography, 29* (8), 1787-1800, 1999.

IPCC, *Climate Change 2000. The science of climate change. Contribution of working group I to the third assessment report of the Intergovernmental Panel on Climate Change.*, Cambridge University Press, Cambridge, 2001.

Jacka, T.H., W. Abdalati, I. Allison, F. Carsey, G. Casassa, M. Fily, M. Frezzotti, H.A. Fricker, C. Genthon, I. Goodwin, Z. Guo, G.S. Hamilton, R.C.A. Hindmarsh, C.L. Hulbe, K.C. Jezek, T.A. Scambos, C. Shuman, P. Skvarca, S. Takahashi, R.S.W. van de Wal, D.G. Vaughan, W.L. Wang, R.C. Warner, D.J. Wingham, N.W. Young, and H.J. Zwally, Recommendations for the collection and synthesis of Antarctic Ice Sheet mass balance data, *Global and Planetary Change*, *42* (1-4), 1-15, 2004.

Jacobs, S.S., A.L. Gordon, and A.F. Amos, Effect of glacial ice melting on the Antarctic Surface Water, *Nature*, *277*, 469-471, 1979.

Jacobs, S.S., H.H. Hellmer, C.S.M. Doake, A. Jenkins, and R.M. Frolich, Melting of ice shelves and the mass balance of Antarctica, *Journal of Glaciology*, *38*, 375, 1992.

Jacobs, S.S., H.H. Hellmer, and A. Jenkins, Antarctic ice sheet melting in the Southeast Pacific, *Geophysical Research Letters*, *23* (9), 957-960, 1996.

Jain, A., *Fundamentals of Digital Image Processing*, 592 pp., Prentice Hall, London, 1988.

Jansen, D., H. Sandhager, and W. Rack, Model experiments on large tabular iceberg evolution: ablation and strain thinning, *Journal of Glaciology*, *51* (174), 2005.

Jenkins, A., The impact of melting ice on ocean waters, *Journal of Physical Oceanography*, *29* (9), 2370-2381, 1999.

Jenkins, A., D.G. Vaughan, S.S. Jacobs, H.H. Hellmer, and J.R. Keys, Glaciological and oceanographic evidence of high melt rates beneath Pine island glacier, west Antarctica, *Journal of Glaciology*, *43* (143), 114-121, 1997.

Keys, H.J.R., S.S. Jacobs, and D. Barnett, The Calving and Drift of Iceberg B-9 in the Ross Sea, Antarctica, *Antarctic Science*, *2* (3), 243-257, 1990.

Keys, J.R., and A.D.F. Fowler, Sources and movement of icebergs in the south-west Ross Sea, Antarctica., *Annals of Glaciology*, *12*, 85-88, 1989.

King, J.C., and J. Turner, *Antarctic Meteorology and Climatology*, 408 pp., Cambridge University Press, Cambridge, 1997.

Kwok, R., H.J. Zwally, and D.H. Yi, ICESat observations of Arctic sea ice: A first look, *Geophysical Research Letters*, *31* (16), 2004.

Levitus, S., R. Burgett, and T.P. Boyer, *World Ocean Atlas 1994, Volume 3, Salinity.*, 1994.

Lichey, C., and H.H. Hellmer, Modeling giant-iceberg drift under the influence of sea ice in the Weddell Sea, Antarctica, *Journal of Glaciology*, *47* (158), 452-460, 2001.

Long, D.G., J. Ballantyne, and C. Bertoia, Is the number of Antarctic icebergs really increasing?, *EOS*, *83* (42), 472-474, 2002.

Luthcke, S.B., D.D. Rowlands, T.A. Williams, and M. Sirota, Reduction of ICESat systematic geolocation errors and the impact on ice sheet elevation change detection, *Geophysical Research Letters*, *32* (21), 2005.

Lythe, M.B., D.G. Vaughan, and B. Consortium, BEDMAP - bed topography of the Antarctic. 1:10,000,000 scale map, British Antarctic Survey, Cambridge, 2000.

Markus, T., The effect of the grounded tabular icebergs in front of Berkner Island on the Weddell Sea ice drift as seen from satellite passive microwave sensors, in *IGARSS '96 - 1996 International Geoscience and Remote Sensing Symposium:*

Remote Sensing for a Sustainable Future, Vols I - Iv, pp. 1791-1793, I E E E, New York, 1996.

Martin, C.F., R.H. Thomas, W.B. Krabill, and S.S. Manizade, ICESat range and mounting bias estimation over precisely-surveyed terrain, *Geophysical Research Letters, 32*, 2005.

McIntyre, N.F., and W. Cudlip, Observation of a giant Antarctic tabular iceberg by satellite radar altimetry, *Polar Record, 23*, 458-462, 1987.

Meyer, F., and S. Beucher, Morphological Segmentation, *Journal of Visual Communications and Image Representation, 1* (1), 21-46, 1990.

Morgan, V.I., and W.F. Budd, The distribution, movement and melt rates of antarctic icebergs, in *Iceberg Utilization. Proceedings of the first International Conference*, edited by A.A. Husseiny, pp. 220-227, Pergamon Press, London, 1978.

Najman, L., and M. Schmitt, Geodesic saliency of watershed contours and hierarchical segmentation, *IEEE Transactions on Pattern Analysis and Machine Intelligence, 18* (12), 1163-1173, 1996.

Neshyba, S., Upwelling by Icebergs, *Nature, 267* (5611), 507-508, 1977.

Nicholls, K.W., and K. Makinson, Ocean circulation beneath the western Ronne Ice Shelf, as derived from in situ measurements of water currents and properties, in *Ocean, Ice and Atmosphere: Interactions and the Antarctic Continental Margin*, edited by S.S. Jacobs, and R.F. Weiss, pp. 301-318, AGU, Washington, D.C., 1998.

Oliver, C., and S. Quegan, *Understanding Synthetic Aperture Radar Images*, 479 pp., Artech House, Boston, 1998.

Orheim, O., Iceberg discharge and the mass balace of Antarctica, in *Glaciers, Ice Sheets and Sea Level: Effect of a CO_2-induced Climatic Change. Report of a Workshop held in Seattle, Washington, September 13-15, 1984.*, pp. 210-215, National Academy Press, Washington, DC, 1985a.

Orheim, O., Iceberg discharge and the mass balance of Antarctica, *Iceberg Research, 8*, 3-7, 1985b.

Orheim, O., Antarctic icebergs-production, distribution and disintregation (abstract), *Annals of Glaciology* (11), 205, 1988.

Orheim, O., Extracting climatic information from the observation of icebergs in the southern ocean (abstract), *Ann. Glaciol., 14*, 352, 1990.

Orsi, A.H., T. Whitworth, and W.D. Nowlin, On the Meridional Extent and Fronts of the Antarctic Circumpolar Current, *Deep-Sea Research Part I-Oceanographic Research Papers, 42* (5), 641-673, 1995.

Payne, A.J., A. Vieli, A.P. Shepherd, D.J. Wingham, and E. Rignot, Recent dramatic thinning of largest West Antarctic ice stream triggered by oceans, *Geophysical Research Letters, 31* (23), art. no.-L23401, 2004.

Phillips, H.A., and S.W. Laxon, Tracking of Antarctic Tabular Icebergs Using Passive Microwave Radiometry, *International Journal of Remote Sensing, 16* (2), 399-405, 1995.

Power, D., J. Youden, K. Lane, C. Randell, and D. Flett, Iceberg detection capabilities of RADARSAT synthetic aperture radar, *Canadian Journal of Remote Sensing, 27* (5), 476-486, 2001.

Rapley, C.G., W. Cudlip, K.C. Partington, N.F. McIntyre, and J.K. Ridley, Satellite Radar Altimetry of Ice Sheets and Ice Shelves, in *Antarctic Special Topic Award Scheme Symposium*, edited by R.B. Heywood, pp. 43-50, British Antarctic Survey, 1989.

Richardson, G., M.R. Wadley, K.J. Heywood, D.P. Stevens, and H.T. Banks, Short-term climate response to a freshwater pulse in the Southern Ocean, *Geophysical Research Letters, 32* (3), art. no.-L03702, 2005.

Ridley, J.K., and K.C. Partington, A Model of Satellite Radar Altimeter Return from Ice Sheets, *International Journal of Remote Sensing, 9* (4), 601-624, 1988.

Rignot, E., Mass balance of East Antarctic glaciers and ice shelves from satellite data, *Annals of Glaciology, 34*, 217-227, 2002.

Rignot, E., D. Braaten, S.P. Gogineni, W.B. Krabill, and J.R. McConnell, Rapid ice discharge from southeast Greenland glaciers, *Geophysical Research Letters, 31* (10), art. no.-L10401, 2004.

Rignot, E., and R.H. Thomas, Mass balance of polar ice sheets, *Science, 297* (5586), 1502-1506, 2002.

Ripley, B.D., *Spatial Statistics*, 252 pp., Wiley and Sons, New York, 1981.

Rist, M.A., P.R. Sammonds, H. Oerter, and C.S.M. Doake, Fracture of Antarctic shelf ice, *Journal of Geophysical Research-Solid Earth, 107* (B1), 2002.

Rott, H., H. Miller, K. Sturm, and W. Rack, Application of ERS-1 SAR and scatterometer data for studies of the Antarctic ice sheet, in *Second ERS-1 symposium*, pp. 133-139, ESA, Cannes, France, 1993.

Russell-Head, D.S., The melting of free drifting icebergs, *Ann. Glaciol., 1*, 119-122, 1980.

Saunders, P.M., A.C. Coward, and B.A. de Cuevas, Circulation of the Pacific Ocean seen in a global ocean model: Ocean Circulation and Climate Advanced Modelling project (OCCAM), *Journal of Geophysical Research, 104* (C8), 18281-18299, 1999.

Scambos, T., B. Raup, and J. Bohlander, Images of Antarctic ice shelves, National Snow and Ice Data Center, 2001.

Scambos, T., O. Sergienko, A. Sargent, D. MacAyeal, and J. Fastook, ICESat profiles of tabular iceberg margins and iceberg breakup at low latitudes, *Geophysical Research Letters, 32*, 2005.

Schmitt, M., Response to the comment on "Geodesic saliency of watershed contours and hierarchical segmentation", *IEEE Transactions on Pattern Analysis and Machine Intelligence, 20* (7), 764-766, 1998.

Schodlok, M.P., H.H. Hellmer, G. Rohardt, and E. Fahrbach, Weddell Sea Iceberg Drift: Five Years of Observations, *Journal of Geophysical Research, 111*, 2006.

Schweitzer, P.N., Monthly average polar sea-ice concentration, Rep. DDS-27, http://geochange.er.usgs.gov/pub/info/holdings.html, U.S. Geol. Surv., Reston, Virginia, 1993.

Sephton, A.J., L.M.J. Brown, J.T. Macklin, K.C. Partington, N.J. Veck, and W.G. Rees, Segmentation of Synthetic-Aperture Radar Imagery of Sea-Ice, *International Journal of Remote Sensing, 15* (4), 803-825, 1994.

Shepherd, A., D. Wingham, T. Payne, and P. Skvarca, Larsen ice shelf has progressively thinned, *Science, 302* (5646), 856-859, 2003.

Silva, T.A.M., and G.R. Bigg, Computer-based identification and tracking of Antarctic icebergs in SAR images, *Remote Sensing of Environment, 94* (3), 287-297, 2005.

Silva, T.A.M., G.R. Bigg, and K.W. Nicholls, Contribution of giant icebergs to the Southern Ocean freshwater flux, *Journal of Geophysical Research-Oceans, 111* ((C3)), 2006.

Smith, W.H.F., and D.T. Sandwell, Global sea floor topography from satellite altimetry and ship depth soundings, *Science, 277* (5334), 1956-1962, 1997.

Soille, P., *Morphological Image Analysis. Principles and applications.*, 391 pp., Springer, 2002.

Spinhirne, J.D., S.P. Palm, and W.D. Hart, Antarctica cloud cover for October 2003 from GLAS satellite lidar profiling, *Geophysical Research Letters, 32* (22), 2005.

Swithinbank, C., P. McClain, and P. Little, Drift tracks of Antarctic Icebergs, *Polar Record, 18* (116), 495-501, 1977.

Tchernia, P., and P.F. Jeannin, Circulation in Antarctic Waters as revealed by iceberg tracks 1972-1983, *Polar Rec., 22* (138), 263-269, 1984.

Thomas, R.H., Satellite remote sensing over ice, in *Frontiers of Remote Sensing of the Oceans and Troposphere fom Air and Space Platforms, URSI Symposium*, pp. 501-512, NASA conference publication 2303, Tel Aviv, Israel, 1984.

Touzi, R., A. Lopes, and P. Bousquet, A Statistical and Geometrical Edge Detector for Sar Images, *Ieee Transactions on Geoscience and Remote Sensing, 26* (6), 764-773, 1988.

Turner, J., W.M. Connolley, S. Leonard, G.J. Marshall, and D.G. Vaughan, Spatial and temporal variability of net snow accumulation over the Antarctic from ECMWF re-analysis project data, *International Journal of Climatology, 19* (7), 697-724, 1999.

Viehoff, T., and A. Li, Iceberg Observations and Estimation of Submarine Ridges in the Western Weddell-Sea, *International Journal of Remote Sensing, 16* (17), 3391-3408, 1995.

Vincent, L., and P. Soille, Watersheds in Digital Spaces - an Efficient Algorithm Based on Immersion Simulations, *Ieee Transactions on Pattern Analysis and Machine Intelligence, 13* (6), 583-598, 1991.

Wadhams, P., *Ice in the Ocean*, 351 pp., Gordon and Breach Science Publishers, 2000.

Weeks, W.F., and M. Mellor, Some elements of iceberg technology, in *Iceberg Utilization. Proceedings of the first International Conference*, edited by A.A. Husseiny, pp. 45-98, Pergamon press, London, 1978.

Williams, R., and M. Macdonald, An image segmentation technique to infer the outlines of icebergs, depicted in satellite images, from their shadows and bright sunlit surfaces, in *Intelligent Information Systems, 1995. ANZIIS-95. Proceedings of the Third Australian and New Zealand Conference on , 27 Nov 1995*, 1995.

Williams, R.N., W.G. Rees, and N.W. Young, A technique for the identification and analysis of icebergs in synthetic aperture radar images of Antarctica, *International Journal of Remote Sensing, 20* (15-16), 3183-3199, 1999.

Willis, C.J., J.T. Macklin, K.C. Partington, K.A. Teleki, W.G. Rees, and R.G. Williams, Iceberg detection using ERS-1 synthetic aperture radar, *International Journal of Remote Sensing, 17* (9), 1777-1795, 1996.

Young, N.W., Antarctic iceberg drift and ocean currents derived from scatterometer image series, in *Workshop on Emerging Scatterometer Applications - from Research to Operations*, pp. 125-132, EUROPEAN SPACE AGENCY, Paris, 1998.

Young, N.W., Another massive iceberg is born, *Australian Antarctic Magazine* (Spring 2002), 40, 2002.

Young, N.W., D. Turner, G. Hyland, and R.N. Williams, Near-coastal iceberg distributions in East Antarctica, 50-145 degrees E, *Ann. Glaciol.*, *27*, 68-74, 1998.

Zwally, H.J., B. Schutz, W. Abdalati, J. Abshire, C. Bentley, A. Brenner, J. Bufton, J. Dezio, D. Hancock, D. Harding, T. Herring, B. Minster, K. Quinn, S. Palm, J. Spinhirne, and R. Thomas, ICESat's laser measurements of polar ice, atmosphere, ocean, and land, *Journal of Geodynamics*, *34* (3-4), 405-445, 2002.

Appendix List of SAR images used

Table 19 – Details of SAR images used in the performance assessment.

Satellite	Imge type	Orbit	Frame	Acquisition date	Acquisition time	Image
ERS-1	PRI	05114	5715	08-JUL-1992	01:24:08	A
ERS-1	PRI	05157	5715	11-JUL-1992	01:29:54	B
ERS-1	PRI	05386	5715	27-JUL-1992	01:27:05	C

Table 20 - Images used in the Ruppert Coast study, comparing PRI with WS images.

Satellite	Image type	Orbit	Frame	Acquisition date	Acquisition time
ERS-2	PRI	47317	5193	8-MAY-2004	16:40:54
ERS-2	PRI	47317	5211	8-MAY-2004	16:41: 09
ERS-2	PRI	47317	5229	8-MAY-2004	16:41:24
ENVISAT	WS	11428	0396	07-MAY-2004	11:46:17

Table 21 - Images used in the field study on the Eastern Weddell Sea and flux measurement study WS_summer_04/5.

Satellite	Image type	Orbit	Frame	Acquisition date	Acquisition time
Envisat	WS	14718	372	23/12/2004	07:50
Envisat	WS	14718	379	23/12/2004	07:51
Envisat	WS	14718	654	23/12/2004	07:52
Envisat	WS	14761	1417	26/12/2004	07:56
Envisat	WS	14761	1418	26/12/2004	07:57
Envisat	WS	14761	362	26/12/2004	07:58
Envisat	WS	14904	355	05/01/2005	07:41
Envisat	WS	14904	356	05/01/2005	07:42
Envisat	WS	14904	357	05/01/2005	07:43

Table 22- Images used in Weddell Sea mosaic.

Satellite	Image type	Orbit	Frame	Acquisition date	Acquisition time
Envisat	WS	13017	0388	26/08/2004	11:50
Envisat	WS	13017	0395	26/08/2004	11:49
Envisat	WS	13217	0257	09/09/2004	11:10
Envisat	WS	13217	0390	09/09/2004	11:11
Envisat	WS	13217	0584	09/09/2004	11:12
Envisat	WS	13244	0261	11/09/2004	08:29
Envisat	WS	13244	0389	11/09/2004	08:28
Envisat	WS	13244	0393	11/09/2004	08:30
Envisat	WS	13244	0402	11/09/2004	08:30
Envisat	WS	13288	0391	14/09/2004	10:16
Envisat	WS	13499	0392	29/09/2004	04:08
Envisat	WS	13499	1081	29/09/2004	04:08
Envisat	WS	13659	0260	10/10/2004	08:17
Envisat	WS	13659	0268	10/10/2004	08:17
Envisat	WS	13659	0394	10/10/2004	08:18
Envisat	WS	13659	1507	10/10/2004	08:19

Table 23 - Images used for flux measurement study PRI_winter92

Satellite	Image type	Orbit	Frame	Acquisition date	Acquisition time
ERS2	PRI	5114	05715	08/07/1992	01:24:08
ERS2	PRI	5114	05733	08/07/1992	01:24:24
ERS2	PRI	5114	05751	08/07/1992	01:24:39
ERS2	PRI	5114	05769	08/07/1992	01:24:54
ERS2	PRI	5157	05715	11/07/1992	01:29:54
ERS2	PRI	5157	05733	11/07/1992	01:30:25
ERS2	PRI	5157	05751	11/07/1992	01:30:24
ERS2	PRI	5157	05769	11/07/1992	01:30:39
ERS2	PRI	5386	05715	27/07/1992	01:27:05
ERS2	PRI	5386	05733	27/07/1992	01:27:20
ERS2	PRI	5386	05751	27/07/1992	01:27:36
ERS2	PRI	5386	05769	27/07/1992	01:27:51

Table 24 - Images used for flux measurement study WS_summer_03/4

Satellite	Image type	Orbit	Frame	Acquisition date	Acquisition time
Envisat	WS	9519	3916	26/12/2003	03:04
Envisat	WS	9605	4398	1/1/2004	03:14

Table 25 - Images used for flux measurement study WS_winter_04

Satellite	Image type	Orbit	Frame	Acquisition date	Acquisition time
Envisat	WS	13244	0261	11/09/2004	08:29
Envisat	WS	13244	0389	11/09/2004	08:28
Envisat	WS	13244	0393	11/09/2004	08:30
Envisat	WS	13244	0402	11/09/2004	08:30
Envisat	WS	13659	0260	10/10/2004	08:17
Envisat	WS	13659	0268	10/10/2004	08:17
Envisat	WS	13659	0394	10/10/2004	08:18
Envisat	WS	13659	1507	10/10/2004	08:19